
Development of Beam Diagnostic Systems for Electric Dipole Moment Measurements at Particle Accelerators

Der Fakultät für Mathematik, Informatik und Naturwissenschaften der
RWTH Aachen University vorgelegte Dissertation zur Erlangung des
akademischen Grades eines Doktors der Naturwissenschaften

vorgelegt von

Master of Science

Fabian Hinder

aus Düren (Nordrhein-Westfalen).

Abstract

One puzzle of modern physics is the observed matter over antimatter dominance in the universe. A common explanation for this dominance is based on \mathcal{CP} violating sources. In general \mathcal{CP} violation is included in the Standard Model (SM) of particle physics, but the amount of \mathcal{CP} violation is not sufficient to explain the measured matter-antimatter-asymmetry. Therefore, additional sources beyond the SM are searched for. One way of finding these sources is the search for permanent Electric Dipole Moments (EDMs) of fundamental particles, since they violate \mathcal{CP} symmetry. The search for EDMs started decades ago in the sector of neutral particles. Up to now all measurements of EDMs are compatible with zero. Complementary to the neutral particles, the EDMs of charged particles, like the proton or deuteron, are of interest to disentangle possible sources of \mathcal{CP} violation. For the charged particles, new experimental methods are needed. These methods are based on the usage of dedicated particle storage rings. In order to develop a dedicated storage ring, the JEDI (Jülich Electric Dipole moment Investigations) collaboration started experiments at the existing magnetic storage ring COSY (Cooler Synchrotron), at Forschungszentrum Jülich in Germany. Within the years 2017 to 2019, a first direct EDM measurement of the deuteron by using a radio frequency Wien filter is planned. In this experimental setup, a non zero EDM would lead to a polarization buildup out of the storage ring plane into the vertical direction. This buildup can also be created by interactions of the magnetic dipole moment with magnetic fields, if the trajectory of the particle beam is not centered in the magnetic elements of the accelerator. In order to counteract this systematic error sources, an orbit correction scheme, including Beam Position Monitors (BPMs) and corrector magnets is needed.

The existing BPM system at COSY, including the readout electronics, allows a position measurement with a statistical resolution of $1\ \mu\text{m}$ for a centered beam. In addition to the statistical resolution, the accuracy is one important characteristic for a beam position measurement. This accuracy is in the order of $0.1\ \text{mm}$ for the existing electronics and one major source of systematic uncertainties for EDM experiments. As a conclusion of this result, an upgrade program of the BPM readout has started with the goal to reach an accuracy and resolution of $4\ \mu\text{m}$.

In order to correct the measured beam position to zero, a correction algorithm is developed and benchmarked. This correction algorithm includes the soft-

ware development of an automated measurement of the Orbit Response Matrix (ORM) and a detailed analysis of the inversion of this matrix. The inverted matrix is used to calculate deflection angles for the corrector magnets in order to correct the beam position in all elements. Applying the correction algorithm results in an orbit RMS (Root Mean Square) of ≈ 2 mm, which is not sufficient for EDM measurements and much worse than the theoretical limit derived from the BPM resolution and accuracy. Simulations have been performed to explain this discrepancy. The simulations indicate, that the magnets positions are known to a precision of 0.5 mm. In a survey of all magnets this prediction was confirmed. Based on these results an alignment campaign started and is ongoing. Besides the realignment of the magnets, additional corrector magnets and additional BPMs can be placed within the simulations to improve the orbit quality. Upgrading COSY with additional elements and realigning the magnets should lead to an orbit RMS of $10\ \mu\text{m}$, which is in the same range as the resolution and accuracy of the upgraded BPM electronics.

Besides the correction algorithm, which is a starting point of a live orbit feedback, the connection of spin tune changes and ORM measurements was analyzed. As a result of this analysis, a new method to measure the dispersion function at corrector magnets is developed and presented in this thesis.

Contents

Nomenclature	VII
1. Introduction	1
2. Motivation	3
2.1. Matter - Antimatter - Asymmetry	3
2.2. Discrete Symmetries and their Transformations	4
2.2.1. Parity Transformation	5
2.2.2. Charge Conjugation	5
2.2.3. Time Reversal	5
2.2.4. Combined Charge and Parity Transformation	6
2.3. Electric Dipole Moments	6
2.3.1. Definition of EDMs	7
2.3.2. Sources for CP Violation and their Connection to EDMs	8
2.3.3. Existing EDM Measurements	9
2.4. EDM Search in Storage Rings	11
3. Beam Dynamics in Storage Rings	15
3.1. Lorentz-Force	15
3.2. Coordinate System	15
3.3. Transverse Motion	16
3.3.1. Bending Magnets	17
3.3.2. Focusing Magnets	18
3.3.3. Equations of Motion	19
3.3.4. Hill's Equation	20
3.3.5. Dispersion	21
3.3.6. Field Errors	22
3.4. Longitudinal Motion and Path Lengthening	25
4. Spin Dynamics in Storage Rings	27
4.1. Polarization	27
4.1.1. Spin- $\frac{1}{2}$ Particles	27
4.1.2. Spin-1 Particles	29
4.2. Spin Motion in Storage Rings	30
4.2.1. Coordinate Systems	30
4.2.2. Spin Motion in Rest Frame	30

4.2.3. Relativistic Particles	31
5. Accelerator Complex around COSY	33
5.1. COSY - Cooler Synchrotron	33
5.2. EDDA Polarimeter	35
6. Beam Position Monitor System at COSY	39
6.1. Commonly used BPMs	39
6.2. Uncertainties of Beam Position Measurements	41
6.2.1. Resolution Limited by Thermal Noise	42
6.2.2. Readout Electronics	43
6.3. Planned Upgrade of the Readout Electronics	48
7. Orbit Response Matrix	51
7.1. Measurement Software	51
7.1.1. Corrector Magnet Settings	52
7.1.2. Beam Position Monitor Readout	54
7.1.3. Timing	55
7.2. Orbit Response Matrix Calculation	57
7.2.1. Noise Measurement	57
7.2.2. Matrix Entry Calculation	61
7.3. Orbit Correction	66
7.3.1. Correlated Data	67
7.3.2. Singular Value Decomposition	68
7.3.3. Example of an Orbit Correction using TSVD	72
7.3.4. Further Developments toward Orbit Feedback System	76
7.4. Simulations	77
7.4.1. Misalignment of Quadrupoles	78
7.4.2. BPM Resolution	82
7.4.3. Alignment of Dipoles and Quadrupoles	84
7.4.4. Additional Elements	87
8. Systematic Effects on Spin Motion	93
8.1. Dispersion Measurements at the Corrector Magnets	93
8.1.1. Theoretical Model	93
8.1.2. Spin Tune Monitoring	94
8.1.3. Measurement Results	97
8.1.4. Outlook: Orbit Correction and EDM Measurement	100
9. Conclusion and Outlook	103
Bibliography	i
List of Figures	xi

List of Tables	xiii
A. Appendix	xv
A.1. Derivation of the RMS Expectation Value	xv

Nomenclature

ADC	Analog to Digital Converter
AMS	Alpha Magnetic Spectrometer
ANKE	Apparatus for Studies of Nucleon and Kaon Ejectiles
BBN	Big-Bang Nucleosynthesis
BPM	Beam Position Monitor
\mathcal{C}	Charge conjugation
CKM	Cabibbo-Kobayashi-Maskawa matrix
CMB	Cosmic Microwave Background
COSY	COoler SYnchrotron
COSYLab	COntrol SYstem Laboratory
\mathcal{CP}	Charge conjugation and Parity transformation
\mathcal{CPT}	Combined Charge conjugation, Parity transformation and Time reversal
EDDA	Excitation function Data acquisition Designed for the Analysis of phase shifts
EDM	Electric Dipole Moment
EPICS	Experimental Physics and Industrial Control System
JULIC	Jülich Light Ion Cyclotron
LHC	Large Hadron Collider
LOCO	Linear Optics from Closed Orbit
LSB	Least Significant Bit
MADX	Methodical Accelerator Design version X
MC	Monte Carlo
MDM	Magnetic Dipole Moment
ORM	Orbit Response Matrix
\mathcal{P}	Parity transformation
PAX	Polarized Antiproton eXperiments
QCD	Quantum Chromo Dynamics
RF	Radio Frequency
RMS	Root Mean Square ($RMS^2 = \frac{1}{N} \sum_{i=1}^N x_i^2$)

Nomenclature

ROOT	Data analysis software framework
SM	Standard Model of particle physics
SQUID	Superconducting QUantum Interference Device
STD	STANDARD Deviation ($STD^2 = \frac{1}{N-1} \sum_{i=1}^N (x_i - \bar{x})^2$)
SVD	Singular Value Decomposition
\mathcal{T}	Time reversal
T-BMT	Thomas Bargmann Michel Telegdi
TSVD	Truncated Singular Value Decomposition
WASA	Wide Angle Shower Apparatus
WMAP	Wilkinson Microwave Anisotropy Probe

1. Introduction

Physics describes the phenomena of nature with mathematical models in all details, starting from the evolution of the universe with its galaxies and stars down to the smallest structures, the elementary particles. The Standard Model (SM) of particle physics is successful in describing elementary particles and their interaction. Measurements at high energies, which allow a deep insight in particles, as well as cosmological measurements can be described very precisely by the SM. But the SM is unsuccessful in explaining the measured lack of antimatter in the known part of the universe. Explanations for the disappearance of antimatter during the early universe are based on the assumption, that fundamental symmetries are violated. Since the violation of symmetries is so important, modern experiments try to measure violation of these symmetries. One candidate for the violation of time or equivalent the combined charge and parity violation is the Electric Dipole Moment (EDM) of fundamental particles. This EDM is in the SM much below the experimental sensitivity, but extensions of the SM, which are able to describe the measured disappearance of antimatter, predict larger EDMs which can be measured with technologies available today. Therefore a measurement of such an EDM is a candidate to confirm these models. Since 60 years, measurements of EDMs on neutral particles have been performed. The statistical and systematical sensitivity improved during this time. Up to now all measurements are compatible with zero within their systematical sensitivity and no EDM was found. All these measurements are based on the principle, of trapping the particle and applying electrical fields to manipulate the polarization, which is influenced by the coupling of the electrical fields and the EDM. For charged particles, such an experiment is not possible, since electric fields will accelerate the particle outside of the particle trap. In order to enable EDM measurements on charged, elementary particles an experimental method is investigated within the JEDI¹ collaboration. This method uses a particle storage ring as a particle trap. The charged, polarized particles circulate in the storage ring and radial electric fields or vertical magnetic fields can be applied. A change of the polarization direction is a direct signal for an EDM, which couples to the electric fields. The JEDI collaboration aims for a dedicated EDM storage ring for protons and deuterons, which improves the systematical and statistical sensitivity.

¹JEDI - Jülich Electric Dipole moment Investigations

1. Introduction

As a starting point for the studies of the JEDI collaboration, the existing storage ring Cooler Synchrotron (COSY) at Forschungszentrum Jülich in Germany is used. COSY provides polarized protons or deuterons. The accelerator is equipped with spin manipulating devices and a polarimeter to monitor the polarization evolution. Within the next years, a first direct measurement of the deuteron EDM is planned. The systematical sensitivity is reduced, compared to a dedicated storage ring, but the principle mechanisms of EDM measurements on charged particles can be studied. The knowledge, gained with these measurements will help to construct a dedicated storage ring. One important quantity, which increases the systematic sensitivity, is the quality of the closed orbit. In other words, the particle beam has to be centered in all accelerator elements to reduce systematic effects.

The aim of this thesis is the improvement of the orbit quality at COSY. This is done by improving the orbit measurement, the orbit correction scheme as well as the investigation of the main sources of orbit disturbances. The thesis itself is structured as follows.

Chapter 2 summarizes the matter over antimatter problem of the SM. The definition of the EDM of fundamental particles is given here and its connection to fundamental symmetries is described. The EDM measurement principle in accelerators is explained as well. The mathematical tools to describe the particle trajectory in an accelerator is depicted in chapter 3. This chapter is focused on the equations and terms needed to perform orbit correction and its connection to spin manipulation. Chapter 4 illustrates the spin dynamics in storage rings, since for the EDM measurement the knowledge of the spin is of interest. Chapter 5 introduced COSY and its elements, the particle sources, the cooling elements and the spin manipulating devices. The EDDA detector, used for polarization measurements, is described in this chapter as well. In chapter 6 the Beam Position Monitors (BPMs) of COSY are investigated and their performance is analyzed. The beam positions, measured with the BPMs, are later used as starting point for the orbit correction scheme. Chapter 7 is the main part of this thesis. It explains a model independent way of the orbit correction with the existing hardware devices, the BPMs and the corrector magnets. In addition, the investigation of upgrades to improve the orbit is presented. Chapter 8 presents a measurement, which combines the tools, developed in the orbit correction chapter in combination with spin monitoring. This combination allows to measure parameters of COSY, which can be used to improve the theoretical understanding of the accelerator model. Chapter 9 summarizes the results and gives an outlook.

2. Motivation

Within this chapter, the physical case, "Why we are interested in searching for electric dipole moments" is described. In addition a short overview about the existing measurements of electric dipole moments is presented as well as the measurement concept for charged particles.

2.1. Matter - Antimatter - Asymmetry

Cosmology and the Standard Model of particle physics (SM) fail to explain why there is a big amount of matter and no antimatter in the universe. This matter-antimatter-asymmetry is expressed in the baryon-antibaryon-asymmetry η_{BA} , which is defined as the difference of the baryon density n_B and the antibaryon density $n_{\bar{B}}$ relative to the photon density n_γ after the primordial nucleosynthesis:

$$\eta_{\text{BA}} = \frac{n_B - n_{\bar{B}}}{n_\gamma}. \quad (2.1)$$

On the one hand, this asymmetry is a parameter in cosmological models and on the other hand, it can be measured by astrophysical observations. Two independent measurements of the baryon-antibaryon-asymmetry were performed up to now. One is the measurement of the occurrence of lightweight nuclei, which were synthesized during the first three minutes after the Big Bang, during the Big-Bang Nucleosynthesis (BBN)[1, 2]. A second method is the analysis of the cosmic microwave background (CMB), measured by the satellite experiments WMAP¹ and Planck. The results of both measurements are compatible with each other and read [3, 4]:

$$5.8 \cdot 10^{-10} \leq \eta_{\text{BA}} \leq 6.6 \cdot 10^{-10} \quad (\text{BBN, 95 \% C.L.}), \quad (2.2)$$

$$\eta_{\text{BA}} = (6.09 \pm 0.06) \cdot 10^{-10} \quad (\text{CMB}). \quad (2.3)$$

The baryon-antibaryon-asymmetry expectation from the SM and standard cosmological models is in the order of [5]:

$$\eta_{\text{SM}} = 10^{-18}, \quad (2.4)$$

¹WMAP - Wilkinson Microwave Anisotropy Probe

2. Motivation

which is eight orders of magnitude below the measured one. Two explanations for this discrepancy are possible:

1. Matter and antimatter are separated in the universe and we are living in a matter dominated region.
2. Asymmetric processes lead to an annihilation of antimatter during the evolution of the universe.

The first hypothesis is investigated by the experiment AMS-02² on the international space station, which searches for single heavy anti-nuclei. A finding of such an anti-nuclei would be an indication of anti-stars in the universe [6].

For the appearance of the second case, the Baryogenesis, three conditions were formulated by Sakharov [7] in 1967:

- **Baryon number violation:** A process, which violates the baryon number conservation, must exist, otherwise the asymmetry of baryons and antibaryons would be zero.
- **Violation of \mathcal{C} and \mathcal{CP} symmetries:** Processes must violate the charge conjugation symmetry (\mathcal{C}) and the combined charge and parity transformation symmetry (\mathcal{CP}). For processes, which generate baryons and are \mathcal{P} symmetric, the conjugated process would generate antibaryons in the same amount as the process itself generates baryons. This would obviously result in $\eta_{BA} = 0$.
- **Out of thermal equilibrium:** The processes have to take place out of thermal equilibrium, otherwise the inverse process can occur and no excess of baryons over antibaryons would be possible.

The Standard Model of particle physics partially fulfills the \mathcal{CP} violation, but the amount of \mathcal{CP} violating processes is too small to explain the measured baryon-antibaryon-asymmetry. Additional \mathcal{CP} violating processes, beyond the Standard Model, are necessary. Such processes can manifest in Electric Dipole Moments (EDMs) of elementary particles, as shown later in this chapter.

2.2. Discrete Symmetries and their Transformations

Symmetries and their transformations are of interest in physics, since they are a basis for conservation laws. In particle physics the parity transformation, the

²Alpha Magnetic Spectrometer

charge conjugation, the time reversal and a combination of them are important, therefore they are defined in the following.

2.2.1. Parity Transformation

The parity transformation \mathcal{P} changes the sign of the coordinates of a physical process ($\vec{x} \rightarrow -\vec{x}$), whereas the time coordinate stays the same ($t \rightarrow t$). Processes which are symmetric under \mathcal{P} behave exactly as their mirror image process. The electromagnetic and the strong interactions of particles are parity symmetric, whereas the weak interaction is parity violating: After the observation of the K^+ decay in a final state of two and three pions, which are eigenstates of the parity operator with eigenvalues ± 1 , Lee and Yang postulated parity violation in the weak section of the SM in 1956 [8]. One year later, Wu et. al. performed an experiment, where the beta decay of polarized ^{60}Co was analyzed [9]:



The flight direction of the emitted electrons was always aligned to the initial polarization direction. A parity transformation doesn't effect the polarization direction, but it changes the momentum of flight direction. Thereby the measured process is parity violating. In addition, the spin of the antineutrino points always in the same direction as its momentum. Assuming massless neutrinos, only left handed neutrinos and right-handed anti-neutrinos couple to the weak interaction.

2.2.2. Charge Conjugation

The charge conjugation \mathcal{C} transforms a particle into its antiparticle and changes the sign of all additive quantum numbers of the particle. Under \mathcal{C} a left-handed neutrino converts to a left-handed anti-neutrino, which does not participate in the weak interaction. Therefore the weak interaction is maximal \mathcal{C} violating.

2.2.3. Time Reversal

The time reversal operator \mathcal{T} changes the sign of the time without changing the coordinates ($t \rightarrow -t, \vec{x} \rightarrow \vec{x}$). A process, which runs reverse and is symmetric under \mathcal{T} produces the same rates as the original process.

Tests in the strong and electromagnetic section have shown no evidence for \mathcal{T} violation. In the weak sector, the measurement of the probability of the

2. Motivation

transformations $\bar{K}^0 \rightarrow K^0$ and $K^0 \rightarrow \bar{K}^0$ were compared. The measured asymmetry in the rates is a direct violation of \mathcal{T} symmetry [10]:

$$\frac{R(\bar{K}^0 \rightarrow K^0) - R(K^0 \rightarrow \bar{K}^0)}{R(\bar{K}^0 \rightarrow K^0) + R(K^0 \rightarrow \bar{K}^0)} = (6.6 \pm 1.3_{\text{sys}} \pm 1.0_{\text{stat}}) 10^{-3}. \quad (2.6)$$

The combined operation \mathcal{CPT} , in any order, is conserved for any local quantum field theory, which is Lorentz invariant [11]. Assuming this \mathcal{CPT} theorem, a \mathcal{T} violation follows from \mathcal{CP} violation to hold the \mathcal{CPT} symmetry. The \mathcal{CPT} theorem itself is tested by measuring the mass differences of particles and their antiparticles, which is predicted to be zero. Up to now no mass differences were found [12].

2.2.4. Combined Charge and Parity Transformation

A direct violation of the combined symmetry \mathcal{CP} was measured by Cronin and Fitch in the decay of K^0 particles in 1964 [13]. The rate asymmetry of the decays:

$$K_L^0 \rightarrow \pi\pi \text{ and } K_L^0 \rightarrow \pi\pi\pi \quad (2.7)$$

is different. In the decay, two or three pions represent: $\pi\pi = \pi^0\pi^0$ or $\pi\pi = \pi^+\pi^-$ and $\pi\pi\pi = \pi^+\pi^-\pi^0$ or $\pi\pi\pi = \pi^0\pi^0\pi^0$. This asymmetry is \mathcal{CP} violating, since the second process is the \mathcal{CP} transformed process of the first one. The measured asymmetry can be explained by the unitary 3×3 Cabibbo-Kobayashi-Maskawa (CKM) matrix, which describes the mixing of the six quarks [14]. The complex phase of the CKM matrix δ is proportional to the \mathcal{CP} violation. Unfortunately, the \mathcal{CP} violation in the CKM matrix is not sufficient to explain the matter-antimatter-asymmetry. Therefore, additional sources of \mathcal{CP} violation are focus of present research. Such sources can manifest in permanent EDMs as shown in the following section.

2.3. Electric Dipole Moments

This section deals with EDMs. First of all a general definition of EDMs is given, followed by its behavior under transformations. The section closes with sources of EDMs for elementary particles.

2.3.1. Definition of EDMs

The EDM of a particle is classically defined as a displacement of charges:

$$\vec{d} = \int_V \rho(\vec{r}) \cdot \vec{r} d\vec{r}, \quad (2.8)$$

where ρ is the charge density. In particle physics, an EDM is a fundamental property of a particle. It is aligned parallel or antiparallel to the spin \vec{S} of the particle, since the quantization axis of the spin is the only distinguished direction [15]. The EDM \vec{d} and the magnetic dipole moment (MDM) $\vec{\mu}$ are given by:

$$\vec{d} = \eta_{\text{EDM}} \frac{q}{2mc} \vec{S} \quad (2.9)$$

$$\vec{\mu} = g \frac{q}{2m} \vec{S}, \quad (2.10)$$

where q and m denote the charge and the mass of the particle, resp. . The speed of light is c . The parameter g is the g -factor of the particle, η_{EDM} is a scaling factor, defined in analogy with the g -factor.

The Hamiltonian of a particle at rest with magnetic and electric dipole moment in external magnetic \vec{B} and electric \vec{E} fields reads:

$$H = -\vec{\mu} \cdot \vec{B} - \vec{d} \cdot \vec{E}. \quad (2.11)$$

The parity and time transformations of the Hamiltonian results in:

$$H = -\vec{\mu} \cdot \vec{B} - \vec{d} \cdot \vec{E} \quad \xrightarrow{\mathcal{P}} \quad H = -\vec{\mu} \cdot \vec{B} + \vec{d} \cdot \vec{E} \quad (2.12)$$

$$H = -\vec{\mu} \cdot \vec{B} - \vec{d} \cdot \vec{E} \quad \xrightarrow{\mathcal{T}} \quad H = -\vec{\mu} \cdot \vec{B} + \vec{d} \cdot \vec{E}. \quad (2.13)$$

The magnetic field and the spin of the particle are eigenstates of parity transformations with the eigenvalue $+1$. The electric field changes the sign under parity transformation, therefore it's eigenvalue is -1 . The product of \vec{d} and the electric field is therefore parity symmetry violating, whereas $\vec{\mu} \cdot \vec{B}$ stays unchanged under parity transformation.

For the time reversal, the magnetic field changes the sign and the direction of the spin flips. This results in an unchanged product of both quantities. In contrast, the electric field is an eigenstate with eigenvalue $+1$ of \mathcal{T} transformations, therefore the EDM violates time reversal symmetry. The described situation is visualized in Fig. 2.1. Assuming the \mathcal{CPT} theorem, an EDM, which violates \mathcal{T} symmetry is directly violating \mathcal{CP} .

2. Motivation

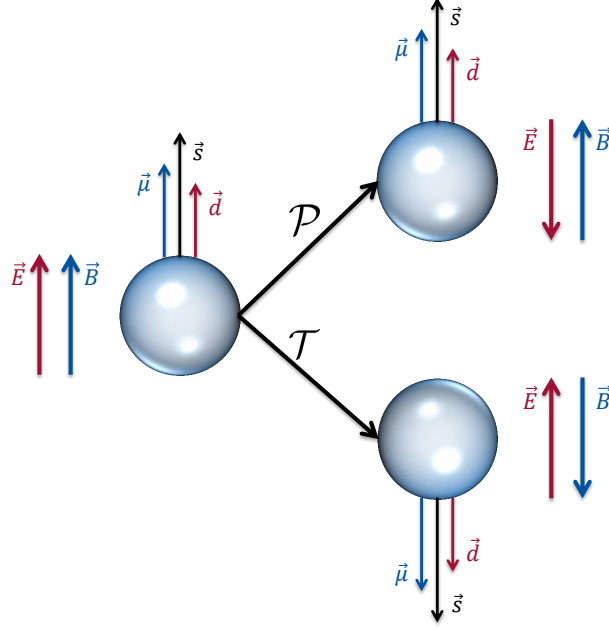


Figure 2.1.: Schematic drawing of a particle with magnetic and electric dipole moments, aligned to the spin, under parity transformation and time reversal. Under parity transformation, the particle stays the same, but an external electric field changes the sign. Under time reversal, the spin and the associated quantities EDM and MDM changes the sign. The external magnetic field changes the direction, whereas the electric field stays the same. Due to the described transformations, a non-zero EDM violates time and parity symmetry (adopted from [16, figure 2.1]).

2.3.2. Sources for CP Violation and their Connection to EDMs

Possible EDMs of particles can be induced by manifold sources. Within the SM the weak as well as the strong sector can introduce EDMs via higher order corrections, motivated in the following.

Weak Sector In the weak sector, the already mentioned imaginary phase of the CKM matrix contributes to \mathcal{CP} violation. This contribution to EDMs of neutrons or protons is on the three-loop level. The contribution to the electron EDM is even on the four-loop level. Therefore the EDM is tiny and the resulting

predictions for EDMs of neutrons and electrons are [15, 17, 18]:

$$d_n \approx 10^{-32} e \text{ cm} \quad (2.14)$$

$$d_e \approx 10^{-40} e \text{ cm}. \quad (2.15)$$

Strong Sector Another source in the SM is the θ_{QCD} term, which is an additional term added to the Lagrangian of the quantum chromodynamics (QCD):

$$\mathcal{L}_\theta = -\theta_{\text{QCD}} \frac{g_s^2}{64\pi^2} \epsilon^{\mu\nu\alpha\beta} G_{\mu\nu}^a G_{\alpha\beta}^a. \quad (2.16)$$

In this Lagrangian, $G_{\mu\nu}^a$ is the gluon field tensor, ϵ is the four dimensional Levi-Cevita tensor and g_s denotes the strong coupling constant. The parameter θ_{QCD} can lead to huge EDMs of hadrons, especially the neutron and the proton, compared to the ones generated by the weak sector [19]:

$$d_n = \theta_{\text{QCD}} \cdot (-2.9 \pm 0.9) \cdot 10^{-16} e \text{ cm} \quad (2.17)$$

$$d_p = \theta_{\text{QCD}} \cdot (1.1 \pm 1.1) \cdot 10^{-16} e \text{ cm}. \quad (2.18)$$

Nevertheless, the measurement of the neutron EDM $d_n < 3.0 \cdot 10^{-26} e \text{ cm}$ with a confidence level of 90 % [20] limits the θ_{QCD} term:

$$\theta_{\text{QCD}} < 10^{-10}, \quad (2.19)$$

whereas the natural expectation of this value is $\mathcal{O}(1)$. The existing fine tuning of the θ_{QCD} term is called the strong CP problem of the SM.

2.3.3. Existing EDM Measurements

Since the EDM of a fundamental particle is an ideal probe to search for \mathcal{CP} violating sources, many experiments were done up to now. The principle of the measurements is the following.

Polarized particles or atoms are trapped and the evolution of the polarization, depending on external electric fields, is measured. During the store of the particles, a static and homogeneous magnetic field is present. In addition a static and homogeneous electric field is superimposed. The EDM is determined, by measuring the frequency shift due to the interaction of the EDM and the electric field: $\vec{d} \cdot \vec{E}$. Since the magnetic field contributes to the frequency shift of the system as well ($\vec{\mu} \cdot \vec{B}$), the polarity of the electric field is switched systematically to disentangle the EDM from the MDM. A change of the electric field influences the Larmor precession frequency for a non-vanishing EDM. The difference of

2. Motivation

the frequencies $\Delta\omega$, measured for both polarities, is proportional to the EDM d :

$$\Delta\omega = \omega(E^+) - \omega(E^-) = \frac{4dE}{\hbar}. \quad (2.20)$$

The first EDM limit of the neutron was measured in the years 1949 to 1951 and published in 1957 by Smith, Ramsey and Purcell [21]:

$$d_n = (0.1 \pm 2.4) \cdot 10^{-20} \text{ e cm}. \quad (2.21)$$

Over the last 60 years, the systematic uncertainties were reduced and some results of upper EDM limits are:

- $d_n \leq 3 \cdot 10^{-26} \text{ e cm}$ (90 % C.L.) neutron EDM limit, measured on ultra cold neutrons [20].
- $d_e \leq 8.7 \cdot 10^{-29} \text{ e cm}$ (90 % C.L.) electron EDM limit, derived from a measurement using the polar molecule thorium monoxide [22].
- $d_p \leq 7.9 \cdot 10^{-25} \text{ e cm}$ (95 % C.L.) proton EDM limit, derived from the measurement of the ^{199}Hg atomic EDM: $d_{^{199}\text{Hg}} \leq 3.1 \cdot 10^{-29} \text{ e cm}$ (95 % C.L.) [23].
- $d_\mu \leq 1.9 \cdot 10^{-19} \text{ e cm}$ (95 % C.L.) average of the measured EDM of μ^+ and μ^- at the g-2 experiment [24].

All measurements are compatible with EDMs of zero, therefore they all provide upper limits. These upper limits set strong limits on possible extensions of the SM and are complementary to high energy searches at LHC³ [25].

The measured confidence levels for the EDMs of the charged particles, electron and proton, are derived from measurements on neutral atoms. The derivation includes assumptions about the interaction of the nuclei in the atom [26]. The only direct measurement of the EDM of charged particles was performed with a μ^+ and a μ^- beam at the g-2 experiment at Brookhaven National laboratory. For heavy nuclei, like deuterons or Helium, no measurements exist at all. A direct measurement of these EDMs is appropriated to find \mathcal{CP} violating sources.

For charged particles, the classical way of trapping the particle and switching on electric fields is not feasible since they are accelerated by external electric fields. Due to this acceleration, the particles can not be stored. A measurement can only be performed in particle storage rings where the particles circulate with beam lifetimes up to hours.

³LHC - Large Hadron Collider

2.4. EDM Search in Storage Rings

As mentioned in the previous section, the EDMs of charged particles can only be directly measured in storage rings. The principle idea is the same as the one for neutral systems: electric fields interact with the EDM and if the EDM is non-zero, the spin precession is perturbed. A possible layout of such an experiment is the following:

A longitudinally polarized particle beam is injected and trapped inside the accelerator by magnetic or electric fields in the lab frame. These fields, Lorentz transformed to the particle rest frame, moving with the velocity $\vec{\beta}c$ with respect to the lab frame, lead to magnetic and electric fields. The electric field in the rest frame interacts with the EDM. A non-zero EDM would lead to a vertical oscillation of the polarization with the frequency:

$$\vec{\omega}_{\text{EDM}} = -\frac{q}{mc} \frac{\eta_{\text{EDM}}}{2} \left(\vec{E} + c\vec{\beta} \times \vec{B} \right), \quad (2.22)$$

if the polarization stays parallel to the momentum. Unfortunately, the polarization precesses due to the MDM in the horizontal plane with the frequency:

$$\vec{\omega}_{\text{MDM}} = -\frac{q}{m} \left[\left(G + \frac{1}{\gamma} \right) \vec{B} - \left(G + \frac{1}{1+\gamma} \right) \vec{\beta} \times \frac{\vec{E}}{c} \right], \quad (2.23)$$

where it is assumed, that $\vec{B}\vec{\beta} = \vec{E}\vec{\beta} = 0$. The anomalous magnetic moment G is connected to the g -factor $G = \frac{g-2}{2}$. γ is the usual Lorentz γ . A more general motivation of the spin motion equation is given in chapter 4. The momentum vector itself precesses with the frequency $\vec{\omega}_{\text{cyc}} = -\frac{q}{m\gamma} \left(\vec{B} - \frac{\vec{\beta} \times \vec{E}}{\beta^2 c} \right)$. In order to align the spin parallel to the momentum, the spin precession frequency needs to be the same as the momentum precession. This leads to the "Frozen-Spin" condition:

$$G\vec{B} = \left(G - \frac{1}{\gamma^2 - 1} \right) \vec{\beta} \times \frac{\vec{E}}{c}. \quad (2.24)$$

This condition can be fulfilled with different combinations of magnetic and electric fields, depending on the anomalous magnetic moment.

- **For particles with $G > 0$** , the spin can be frozen by using only electric fields at one specific momentum. This momentum, often referred as "magic", is:

$$p = \sqrt{\gamma^2 - 1} \cdot mc = \frac{mc}{\sqrt{G}}. \quad (2.25)$$

For protons with $G = 1.79$, the magic momentum reads $p \approx 0.701 \text{ GeV}/c$.

2. Motivation

- **For particles with $G < 0$** , the frozen spin condition can only be fulfilled by the use of magnetic and electric fields. The combined bending element needs to provide a vertical magnetic field and a radial electric field. The field strength relation is given by:

$$\frac{B}{E} = \left(1 - \frac{1}{G(\gamma^2 - 1)}\right) \frac{\beta}{c}. \quad (2.26)$$

If the spin precession due to the magnetic moment is frozen, the EDM is the only term, contributing to a spin motion. Thus, the EDM can be determined by measuring the frequency ω_{EDM} . For a pure electric ring with fields of $E \approx 10 \text{ MV m}^{-1}$ and an EDM of $d \approx 1 \cdot 10^{-24} \text{ e cm}$ the frequency is approximately 0.1 mHz. This tiny frequency is not measurable, since the polarization lifetime is in the order of 1000 s [27] and only the beginning of the oscillation can be measured. At the beginning of the experiment, the oscillation reads:

$$P_y(t) = P_0 \cdot \sin(\omega_{\text{EDM}}t) \approx P_0 \cdot \omega_{\text{EDM}}t. \quad (2.27)$$

This linear increase of the vertical polarization is directly proportional to the EDM and the slope is the EDM signal in all presented measurement concepts. Actually, the muon EDM limit was extracted from the measurement of the vertical polarization oscillation observed within the g-2 experiment.

For a pure magnetic ring, the spin precession due to the magnetic moment is always present. The additional EDM rotation around a radial axis leads to a tilt of the rotation axis by the angle $\tan \xi = \frac{\eta_{\text{EDM}}\beta}{2G}$. In addition the precession frequency changes to $\omega_{\text{S}}^2 = \omega_{\text{MDM}}^2 + \omega_{\text{EDM}}^2$. Since the EDM effect is tiny with respect to the MDM effect, this frequency change can be neglected. In contrast, the tilt of the rotation axis is in principle measurable, since the polarization oscillates in the vertical plane with the frequency $f_{\text{S}} = \gamma G f_{\text{rev}}$. But the amplitude is small and on average the signal vanishes. In order to increase the signal, an RF Wien filter which operates at a harmonic of the spin frequency $f_{\text{S}} = \frac{\omega_{\text{S}}}{2\pi}$:

$$f_{\text{RF}} = (1 + k) f_{\text{S}} = (1 + k) \gamma G f_{\text{rev}} \quad \text{with } k \in \mathbb{Z}, \quad (2.28)$$

can be used. The electric field of the Wien filter has to point in the radial direction, whereas the perpendicular magnetic field points in the vertical direction. In case of the running Wien filter the vertical polarization oscillates with the frequency f_{S} , which is identical to the situation without an RF device. The use of the Wien filter induces an artificial spin resonance, which leads to a small polarization buildup in the vertical direction. This polarization build-up is proportional to the EDM. A measurement of such a build-up is a first direct measurement of the proton or deuteron EDM. The idea of using a RF Wien

filter is presented in [28, 29]. A detailed analytic explanation and a simulation with particle tracking is presented in [16]. In April 2017, an RF Wien filter, based on a stripline design will be installed in COSY [30]. During 2017 the commissioning will take place and a first deuteron EDM measurement is planned during 2018 [31].

Besides the EDM, misalignments of magnets can lead to such a polarization buildup induced by the Wien filter. This fake EDM signal has to be considered as systematic error. The mentioned simulations using particle tracking methods, show that the fake EDM buildup rate is proportional to the position of the beam within the magnetic quadrupoles. Therefore, the RMS of the beam position in the magnets is a quantity to estimate the unwanted polarization buildup due to the MDM. Two results of the simulations are presented in Tab. 2.1. By using this table, a measured orbit RMS can be converted in a systematic uncertainty of the EDM measurement. For example, a measured orbit RMS of 1.3 mm converts to a systematic uncertainty of the EDM of $5 \cdot 10^{-19} e \text{ cm}$.

Table 2.1.: *The table shows the dependence between the vertical orbit RMS, the vertical fake polarization buildup due to the MDM and the equivalent EDM signal, which produces the same vertical polarization buildup as the MDM effect. For example, an orbit RMS of 1.3 mm leads to a polarization buildup rate of $1.7 \cdot 10^{-9}$ per turn only due to the MDM. A perfectly aligned orbit and an EDM of $5 \cdot 10^{-19} e \text{ cm}$ leads to the same buildup rate. [16, figure 8.15 (b)]*

orbit RMS (mm)	polarization buildup per turn ΔS_y	EDM d_{EDM} (e cm)
1.3	$1.7 \cdot 10^{-9}$	$5 \cdot 10^{-19}$
0.13	$1.7 \cdot 10^{-10}$	$5 \cdot 10^{-20}$

In order to minimize these systematic effects, the orbit of the particle beam has to be centered in all magnets, this is achieved by an orbit correction system, consisting of BPMs and corrector magnets.

Within this thesis, the orbit correction system at COSY is investigated in order to improve the system. First of all, the beam position monitors and their existing readout electronics are analyzed. The limitations of the system are pointed out and as a result an upgrade of the readout has started.

In addition an automated measurement of the Orbit Response Matrix (ORM) and a detailed error analysis of the orbit correction result is presented. The orbit correction study ends with the analysis of an improvement of the system in terms of additional elements. A possible systematic EDM limit is calculated based on the studies and existing simulations.

2. Motivation

Besides the correction of the orbit, the polarization buildup due to the MDM and the EDM can be disentangle by measuring the polarization buildup of two beams. One is circulating clockwise, the other one counterclockwise. The two beams are injected after each other and the fields have to be reversed. The EDM signal of both scenarios is the same, whereas the MDM induced buildup changes the sign. By averaging the measured buildup rate, the MDM signal drops out and only the EDM part stays [32]. The quality of the field reversal can be estimated by measuring the relative position of the two beams, therefore an absolute beam position measurement is not needed. This circumstance is a big advantage, since a relative beam position measurement is easier than an absolute one, as shown in chapter 6.

3. Beam Dynamics in Storage Rings

For the measurement of EDMs in storage rings, a definition, description and knowledge of the particle's trajectory through the magnetic and electric elements is essential. The evolution of this trajectory is called beam dynamics. The mathematical tools to describe the beam dynamics are presented in this chapter. It starts with the fundamental Lorentz force, followed by a short description of the magnetic elements. The combination of both lead to the equations of motion, which is solved for linearly approximated fields. In addition to this ideal case dipole errors and their correction scheme is presented. The descriptions are mainly taken from [33] with additional material from [34, 35, 36].

3.1. Lorentz-Force

A storage ring consists of elements which provide electromagnetic fields. These fields act on a particle with charge q and mass m traveling with the momentum \vec{p} via the Lorentz force:

$$\frac{d\vec{p}}{dt} = \vec{F} = q\vec{E} + \frac{q}{m\gamma} (\vec{p} \times \vec{B}), \quad (3.1)$$

where \vec{E} and \vec{B} are the electric and magnetic field vectors. This force is used to accelerate, guide and focus the beam onto the desired trajectory within the accelerator. The acceleration of particles is only possible by using electric fields, since static magnetic fields lead only to a change of direction, but not to a gain in momentum. The transverse guidance of the particles is usually achieved by magnetic fields, since they are enhanced by a factor $v \approx c$ due to the fact that the particles in accelerators are relativistic. The Lorentz-force is the fundamental force which determines the equations of motion of the particles.

3.2. Coordinate System

For the description of the particle trajectory a coordinate system must be defined. In accelerator physics, the coordinate system is usually split in two parts.

3. Beam Dynamics in Storage Rings

One part describes the ideal path of the particle. The second one is an orthogonal moving coordinate system $(\vec{e}_x, \vec{e}_y, \vec{e}_z)$, which follows the ideal path. The deviation of the particle position $\delta\vec{r}$ from the ideal trajectory \vec{r}_0 can be expressed in these coordinates:

$$\vec{r}(s) = \vec{r}_0(s) + \delta\vec{r}(s). \quad (3.2)$$

Figure 3.1 shows the ideal beam path and a trajectory, which deviates by x, y from the ideal one. The vectors x and y are orthogonal to each other and

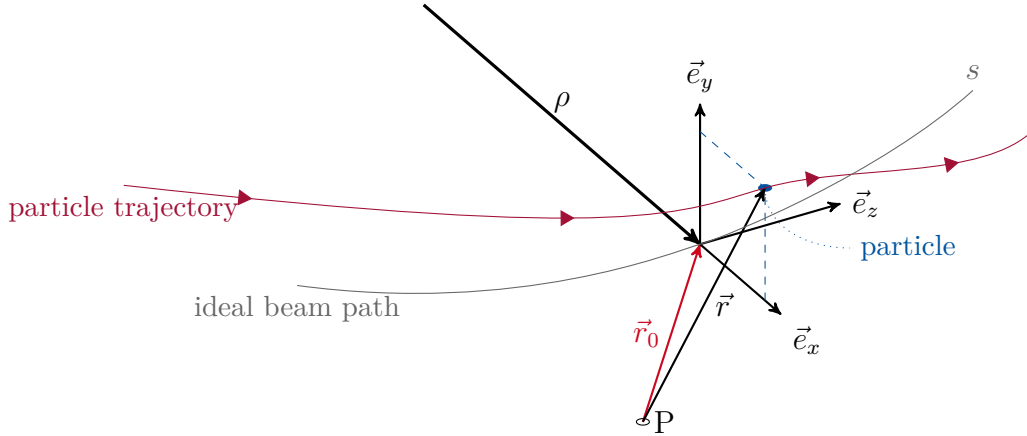


Figure 3.1.: *The commonly used moving coordinate system in accelerator physics. The ideal beam path is described in any arbitrary coordinate system (red). The particle's trajectory (bordeaux red) with respect to the ideal one is expressed in the moving coordinates $(\vec{e}_x, \vec{e}_y, \vec{e}_z)$. (adapted from [33, Fig. 1.2])*

orthogonal to the ideal beam path. The direction of x is chosen in a way, that the bending dipoles of the accelerators bend the beam in $-x$ direction. In this choice, y points upwards. The coordinate z is defined as the vector tangential to the ideal beam path s . This coordinate system is also referred to as the Frenet-Serret coordinate system.

3.3. Transverse Motion

In COSY, three types of magnets are installed: the dipole, the quadrupole, and the sextupole magnets. In all magnets, the equilibrium between the Lorentz force and the centrifugal force determines the local bending radii:

$$m\gamma v^2 \vec{\kappa} = -q\vec{v} \times \vec{B}, \quad (3.3)$$

where $\vec{\kappa} = (\kappa_x, \kappa_y, 0)$ is the transverse curvature of the trajectory. The bending radius is the reciprocal of the curvature:

$$\rho_u = \frac{1}{\kappa_u} \quad u \in \{x, y\}, \quad (3.4)$$

where the coordinate u is introduced as transverse coordinate x or y . The effect of dipole magnets and quadrupole magnets on the beam trajectory is discussed in a descriptive way in the upcoming sections.

3.3.1. Bending Magnets

Assuming only transverse magnetic fields and neglecting transverse velocity components leads to a simplified form of the bending radius in the bending dipoles:

$$\frac{1}{\rho_{x,y}} = \frac{q}{p} B_{y,x}, \quad (3.5)$$

where $p = \gamma m v$ is the momentum of the particle. This formulation of the bending radius shows, that horizontal magnetic fields lead to a vertical curvature of the trajectory, whereas vertical magnetic fields lead to an horizontal bending of the beam path. The kick angle θ , caused by a transverse magnetic field, is calculated by integrating over the curvature from the entrance to the exit of the magnet [33, p. 39]:

$$\theta = \int_{\text{en}}^{\text{ex}} \frac{ds}{\rho} = \int_{\text{en}}^{\text{ex}} B \frac{q}{p} ds \quad (3.6)$$

$$= \underbrace{\frac{q}{p}}_{1/(B\rho)} B \cdot l, \quad (3.7)$$

where l is the length of the magnet. The beam rigidity $B\rho$ is often used to normalize the magnetic strength to the momentum.

Dipole magnetic fields are the main components in a circular accelerator, since they are used to bend the beam trajectory. In addition to the main dipoles, quadrupoles are installed to focus the beam in the vertical and horizontal direction.

3.3.2. Focusing Magnets

The quadrupole magnets provide a magnetic field, which is proportional to the transverse distance measured from the center of the magnet [33, p. 44]:

$$B_x = gy = -\frac{\partial V}{\partial x} \quad (3.8)$$

$$B_y = gx = -\frac{\partial V}{\partial y}, \quad (3.9)$$

where $V = -gxy$ is the scalar potential of the magnet.

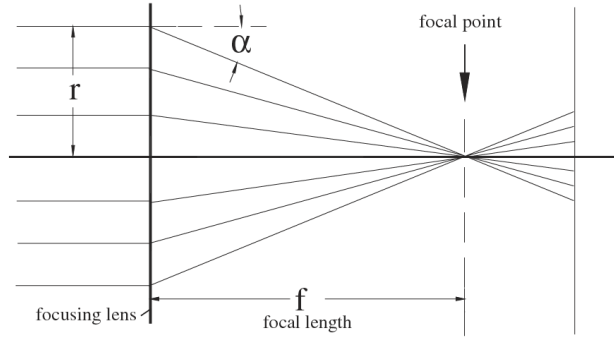


Figure 3.2.: *Focusing of a quadrupole magnet and the geometric definitions of the focal length and the focal point [33, Fig. 2.2].*

In the center of the transverse plane of the magnet, the deflection angle vanishes, since there is no magnetic field. If the beam is off centered horizontally, the magnet bends the beam towards the center. This effect is called focusing. All trajectories are focused in one spot, the focal point (Fig. 3.2). But at the same time, vertically displaced trajectories are bend to the outside and are defocused. A focusing in both planes can be achieved by combining focusing and defocusing elements.

In analogy to the bending radius, the focusing strength is defined as:

$$k = \frac{q}{p}g. \quad (3.10)$$

The focal length f of a quadrupole magnet is defined as

$$\frac{1}{f} = \frac{-\alpha}{r} = kl, \quad (3.11)$$

where l is the path length of the trajectory within the quadrupole. With the help of quadrupole magnets, particles which are slightly off centered in the

transverse direction $u \neq 0$, or whose trajectories have an angle to the ideal beam path $u' \neq 0$ are kept inside the accelerator.

They start to oscillate around the ideal beam path with an amplitude $\sqrt{\epsilon\beta}$, which depends on the magnetic elements. This oscillation is called betatron oscillation. The planes $u - u'$, position and angle in the transverse plane, are called the transverse phase spaces.

3.3.3. Equations of Motion

The betatron oscillations are solutions of the equations of motion motivated in the following. The equation of motion in the transverse planes can be derived by different methods. One method is to use the Lagrangian or the Hamiltonian of the particle motion. Another method is the classical derivation by using the Lorentz force as centrifugal force and considering the partial derivatives of the moving coordinates. Both methods are presented in detail in [33]. The resulting formulas, used within this theses are discussed and presented in the following.

Only linear approximations of the fields (dipole and quadrupole terms) and linear momentum deviations of a single particle with respect to the design momentum p_0 are presented within the focus of this thesis. The momentum deviation Δp reads:

$$\frac{1}{p} = \frac{1}{p_0 \left(1 + \frac{\Delta p}{p_0}\right)} \approx \frac{1}{p_0} \left(1 - \frac{\Delta p}{p_0} + \dots\right). \quad (3.12)$$

Using this approximation leads to the equation of motion for the horizontal direction [35, eq. 3.4]:

$$x'' + \left(k + \kappa_x^2\right) x = \kappa_x \frac{\Delta p}{p_0} \quad \text{with} \quad x'' = \frac{d^2x}{ds^2}. \quad (3.13)$$

Considering only bending in the horizontal plane leads to the equation of motion in the vertical plane:

$$y'' - ky = 0 \quad (3.14)$$

The coefficients in the two equations depend on the magnetic field along the storage ring. The solution of the differential equations is the topic of the following sections.

3.3.4. Hill's Equation

By neglecting momentum deviations, the homogeneous part of (3.13) and (3.14) have the form:

$$u'' + k(s) \cdot u = 0 \quad u \in \{x, y\}. \quad (3.15)$$

For circular accelerators, $K(s)$ has a periodicity which is one circumference $L_P = L_0$, or for periodic structures the length of the structure L_P :

$$k(s) = k(s + L_P). \quad (3.16)$$

These two equations have the form of Hill's equation [37], originally describing the lunar stability. Hill's equation (3.15) describes a harmonic oscillator with a frequency $\sqrt{k(s)}$, depending on the longitudinal position s . Hill's equation is solved by Floquet's theorem. The solution of the homogeneous part is given by [33, p. 252]:

$$u(s) = \sqrt{\epsilon_u \beta_u(s)} \cos(\Psi_u(s) + \Psi_u(s_0)), \quad (3.17)$$

where ϵ_u and $\Psi_u(s_0)$ reflect the initial conditions. The function $\beta_u(s)$ is the betatron function, which depends on the lattice of the accelerator. The phase advance $\Delta\Psi_u$ between the position s_0 and s can be calculated by:

$$\Delta\Psi_u(s) = \int_{s_0}^s \frac{1}{\beta_u(\zeta)} d\zeta. \quad (3.18)$$

The number of betatron oscillations per turn are called the betatron tune and are defined as:

$$Q_u = \frac{1}{2\pi} \int_s^{s+L_0} \frac{1}{\beta_u(\zeta)} d\zeta. \quad (3.19)$$

The first derivative of (3.17) is:

$$u'(s) = -\frac{\sqrt{\epsilon_u}}{\sqrt{\beta_u(s)}} [\alpha_u(s) \cos(\Psi_u(s) + \Psi_u(s_0)) + \sin(\Psi_u(s) + \Psi_u(s_0))] \quad (3.20)$$

$$\text{with } \alpha_u(s) := \frac{\beta_u'(s)}{2} \text{ and } \gamma_u(s) := \frac{1 + \alpha_u^2(s)}{\beta_u(s)}. \quad (3.21)$$

The functions α_u , β_u , and γ_u are known as the optical functions or Twiss parameters. The trajectory of the particle in the phase space, the plane spanned by u and u' , follows an ellipse:

$$\gamma_u(s)u^2(s) + 2\alpha_u(s)u(s)u'(s) + \beta_u(s)u'^2(s) = \epsilon_u. \quad (3.22)$$

The Twiss parameters define the shape of the phase space ellipse at one position $s = s_0$ as shown in Fig. 3.3. Along the trajectory, the shape of the ellipse changes due to the change of the Twiss parameters, but according to Liouville's theorem the area $\pi\epsilon$ is conserved if all forces are conservative and the transverse phase spaces are decoupled. Considering a single point s_0 the particle moves on the phase space ellipse by a phase advance of $Q_u \cdot 2\pi$ in each turn.

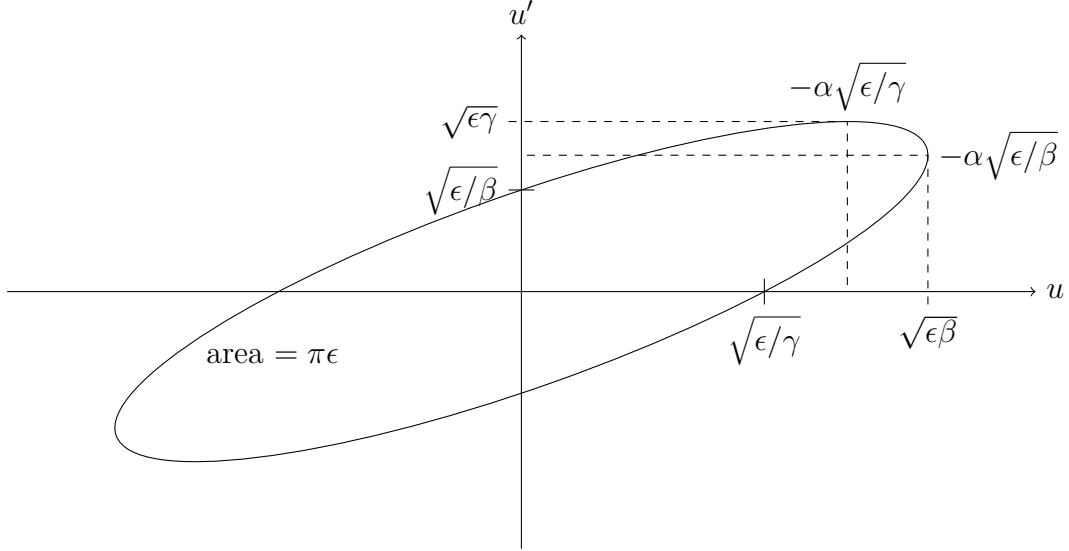


Figure 3.3.: *The transverse phase space motion of a particle is described by an ellipse in the $u - u'$ plane. The shape of the ellipse is defined by the optical functions α, β, γ , and the emittance ϵ (adapted from [33, Fig 5.2]).*

3.3.5. Dispersion

The complete solution x_c of (3.13) consists of the solution of the homogeneous equation, discussed in the previous section, and a particular solution of the inhomogeneous one:

$$x_c(s) = x(s) + x_D(s). \quad (3.23)$$

In accelerator physics, the additional term is called the dispersive orbit following the terms used in optics. The additional part x_D can be expressed as:

$$x_D(s) = D(s) \cdot \frac{\Delta p}{p_0}, \quad (3.24)$$

3. Beam Dynamics in Storage Rings

where the dispersion D is introduced as additional function. It describes the influence of momentum deviations to the horizontal beam position. The vertical dispersion vanishes, since the vertical equation of motion has no curvature term. Inserting (3.23) in (3.13) leads to the differential equation of the dispersion:

$$D''(s) + k(s)D(s) = \kappa_{0x}. \quad (3.25)$$

The solution for the dispersion is given by [33, p. 261]:

$$D(s) = \frac{\sqrt{\beta_x(s)}}{2 \sin \pi Q_x} \int_s^{s+L_P} \frac{\sqrt{\beta_x(\zeta)}}{\rho_x(\zeta)} \cos [Q_x (\Psi_x(s) - \Psi_x(\zeta) + \pi)] d\zeta. \quad (3.26)$$

A momentum deviation leads to a change of the horizontal trajectory, which causes a change of the path length of one turn ΔL . This path lengthening can be calculated by:

$$\Delta L = \int_s^{s+L_0} \kappa_x(\zeta) x(\zeta) d\zeta = \frac{\Delta p}{p_0} \int_s^{s+L_0} \kappa_x(\zeta) D(\zeta) d\zeta. \quad (3.27)$$

Defining the momentum compaction factor

$$\alpha_p = \frac{1}{L_0} \int_0^{L_0} \kappa_x(\zeta) D(\zeta) d\zeta \quad (3.28)$$

leads to the relative path change due to a momentum deviation:

$$\frac{\Delta L}{L_0} = \alpha_p \frac{\Delta p}{p_0}. \quad (3.29)$$

3.3.6. Field Errors

Up to now, only ideal fields and momentum deviations were considered in the discussion of the transverse motion. But in a realistic accelerator, additional field components due to field errors or transverse misalignment of magnets have to be considered.

For example, the vertical quadrupole field ($B_y = gx$) is assumed to be zero at the center. But if the quadrupole is horizontally misaligned by δx , the field in the center is $B_y = g\delta x$, which is a vertical dipole field. This vertical dipole field leads to a horizontal bending of the particle trajectory. In general, displaced magnets of order n produce lower order field components at the desired beam axis. These fields can be considered as perturbation in the equations of motion.

Dipole Field Errors Dipole field errors can be included in the equation of motion as a perturbation $p_{0u}(s)$:

$$u'' + (k + \kappa_u^2) u = p_{0u}(s). \quad (3.30)$$

The perturbation term represents all dipole errors independent of their source. The horizontal and vertical perturbation terms up to second order including field errors ($\Delta\kappa$, and misalignments ($\Delta x, \Delta y$)) read [33, pp. 414-415]:

$$p_{0x} = -\Delta\kappa_{x0} + (\kappa_{x0}^2 + k_0) \Delta x + (2\kappa_{x0}\Delta\kappa_{x0} + \Delta k) \Delta x \quad (3.31)$$

$$- \frac{1}{2} m (\Delta x^2 - 2x_c \Delta x - \Delta y^2 + 2y_c \Delta y)$$

$$p_{0y} = -\Delta\kappa_{0y} - k_0 \Delta y - m (x_c \Delta y + y_c \Delta x), \quad (3.32)$$

where x_c, y_c are the closed orbit deviations in the magnet. Equation (3.30) can be solved in analogy to the solution for the momentum deviation, where the solution is the dispersive function. The solution for dipole perturbations is given by:

$$u_c(s) = \frac{\sqrt{\beta_u(s)}}{2 \sin \pi Q_u} \int_s^{s+L_0} p_{0u}(\zeta) \sqrt{\beta_u(\zeta)} \cos [Q_u (\Psi_u(s) - \Psi_u(\zeta) + \pi)] d\zeta, \quad (3.33)$$

where L_0 is the circumference of the accelerator. This solution is called the closed orbit or equilibrium orbit. Around this defined closed orbit all particles perform betatron oscillations in horizontal and vertical direction. In principle this solution is a stable situation, but due to the deviation of the trajectory from the center of the beam pipe the chance that particles hit the beam pipe and are lost is higher. This effect influences the beam lifetime. More important from the EDM measurement point of view are the unwanted field contributions, which act on an off-centered particle beam.

In order to move the beam in the center of all magnets, additional dipole magnets, the corrector magnets are installed. The strength of the additional dipole fields can be varied to add additional deflection, which corrects the unwanted perturbations caused by field errors or survey errors. Each of the corrector magnets performs a kick θ_j , see (3.7), at the position of the j -th corrector magnet. The resulting orbit change is:

$$u_{\text{cor}}(s) = \frac{\sqrt{\beta_u(s)}}{2 \sin \pi Q_u} \sum_j \theta_j \sqrt{\beta_{uj}} \cos [Q_u (\Psi_u(z) - \Psi_{uj} + \pi)], \quad (3.34)$$

where β_{uj} is the beta function at corrector magnet j . In addition to corrector magnets, devices which measure the transverse beam position are needed. These

3. Beam Dynamics in Storage Rings

devices, the Beam Position Monitors (BPMs), are installed along the accelerator at positions s_i . The orbit change at one BPM due to corrector kicks reads:

$$\Delta u_i = \frac{\sqrt{\beta_{ui}}}{2 \sin \pi Q_u} \sum_j \theta_j \sqrt{\beta_{uj}} \cos [Q_u (\Psi_{ui} - \Psi_{uj} + \pi)], \quad (3.35)$$

where β_{ui} is the beta function at the i -th BPM and $\Psi_{ui} - \Psi_{uj}$ is the phase advance between BPM i and corrector magnet j . The orbit change at all BPMs can be expressed in a matrix notation:

$$\Delta \vec{u} = \mathbf{M} \vec{\theta}, \quad (3.36)$$

where the beam positions at the BPMs and the corrector magnet kicks are written in vector notation. The matrix \mathbf{M} is called the Orbit Response Matrix (ORM). The entries of this matrix are:

$$\mathbf{M}_{ij} = \frac{\sqrt{\beta_i \beta_j}}{2 \sin \pi Q} \cos [Q (\Psi_i - \Psi_j + \pi)]. \quad (3.37)$$

This equation holds for the vertical orbit and the vertical corrector magnets (horizontal dipole field). In the horizontal plane, the matrix has to be modified to also consider dispersive effects [36]:

$$\mathbf{M}_{ij} = \frac{\sqrt{\beta_i \beta_j}}{2 \sin \pi Q} \cos [Q (\Psi_i - \Psi_j + \pi)] - \frac{D_i D_j}{\left(\alpha_p - \frac{1}{\gamma^2}\right) L_0}, \quad (3.38)$$

where D is the dispersion function, α_p is the momentum compaction factor, and γ is the Lorentz factor. The additional term includes the effect, that a kick at a position with dispersion leads to a momentum shift of the beam, if the cavity is switched on. This momentum shift causes a movement of the beam which is proportional to the dispersion at the BPM. Coupling between the vertical and horizontal beam dynamics, caused by tilted quadrupoles or sextupole fields and higher order terms are neglected in the derivation of the ORM entries.

The combination of BPMs, corrector magnets, and the knowledge of the ORM allows the calculation of the corrector magnet strengths in a way, that the beam deviation from the center at the BPMs is minimized. A detailed solution of the problem

$$\min_{\vec{\theta}} \left\| \mathbf{M} \vec{\theta} - \vec{u} \right\|_2, \quad (3.39)$$

where \vec{u} is the measured orbit, is presented in 7.3. In addition the measurement of the ORM as well as the performance of the correction are discussed in the chapters 7.1 and 7.4.

3.4. Longitudinal Motion and Path Lengthening

The longitudinal motion of the particles is influenced by the accelerating cavity, which produces a longitudinal, sinusoidal electric field. The frequency of the field is a multiple integer of the beam revolution frequency. In a synchrotron, the frequency increases synchronously to the particle energy and the magnetic fields, to hold the particle trajectory stable during the acceleration. At the final energy, two operation modes are possible. In the first mode, the cavity is switched off, the beam particles circulate unbunched. In the second mode, the cavity stays on and the beam is bunched. The second case is used for beam position measurements and the orbit correction. In addition, the cavity is switched on for the planned EDM measurements since the polarization lifetime depends on the momentum deviation inside the beam. This momentum deviation is in first order minimized for bunched beams [27]. For bunched beams, the revolution frequency is fixed, which causes coupling between orbit lengthening and momentum deviations discussed in the upcoming paragraph.

The relative revolution frequency change due to path lengthening (ΔL) or due to velocity changes (Δv) is given by:

$$\frac{\Delta f}{f_0} = \frac{\Delta L}{L_0} - \frac{\Delta v}{v_0}. \quad (3.40)$$

The orbit lengthening caused by momentum deviations is given by (3.29). The velocity change due to a momentum change is in first order [38]:

$$\frac{\Delta v}{v_0} = \frac{1}{\gamma_0^2} \frac{\Delta p}{p_0}. \quad (3.41)$$

Consequently, the revolution frequency change due to a momentum change can be expressed as [39]:

$$\frac{\Delta f}{f_0} = \underbrace{\left(\alpha_p - \frac{1}{\gamma_0^2} \right)}_{\eta} \frac{\Delta p}{p_0}, \quad (3.42)$$

where η is the "phase slip factor". Stable operation of the accelerator is only possible for $\eta \neq 0$.

Additional orbit lengthening effects can be considered in (3.40) as well. For example a kick θ_j of a corrector magnet j leads to an orbit change all over the

3. Beam Dynamics in Storage Rings

ring. The resulting first order orbit lengthening ΔL_{θ_j} is given by the integral:

$$\Delta L = \int_0^{L_o} u_{\text{cor}}(\zeta) \kappa(\zeta) d\zeta \quad (3.43)$$

$$= D_j \theta_j, \quad (3.44)$$

where the definition of the dispersion (3.26) and the orbit change due to a corrector change (3.33) are used to solve the integral.

Inserting this additional orbit lengthening in (3.40) and assuming a bunched beam, where the frequency is kept constant, leads to:

$$\frac{\Delta f}{f_0} = \frac{D_j}{L_0} \theta_j + \eta \frac{\Delta p}{p_0} = 0 \quad (3.45)$$

$$\Leftrightarrow \frac{\Delta p}{p_0} = -\frac{D_j}{\eta L_0} \theta_j. \quad (3.46)$$

Possible quadratic contributions depend on the sextupole strengths in the accelerator. By adjusting the sextupole strengths in a way, that the chromaticity is zero, the quadratic term vanishes and only the linear term, mentioned above, lasts [40, 41, 42].

A corrector magnet change at a region where the dispersion is not equal zero leads to momentum change. This momentum change results in a position variation proportional to the dispersion all over the ring (3.24). Since the vertical dispersion is zero, the resulting term exists only in the horizontal plane and reads for a BPM i :

$$\Delta x_i = -\frac{D_i D_j}{\eta L_0} \theta_j. \quad (3.47)$$

This effect is already included in the horizontal ORM entries.

4. Spin Dynamics in Storage Rings

As explained in the previous chapters, polarized particles stored in an accelerator can be used for a measurement of their EDM. The formalism to describe an ensemble of polarized particles, as well as their motion in storage rings is focus of this chapter. First of all, the polarization formalism is motivated, followed by a definition of the coordinate system. The spin motion in the accelerator is then described by the Thomas-Bargmann-Michel-Telegdi equation. The chapter is based on the literature [43, 44, 45, 46].

4.1. Polarization

The spin of a particle is an additional degree of freedom, which is represented by a quantum vectorial operator $\hat{\mathbf{S}} = (\hat{\mathbf{S}}_1, \hat{\mathbf{S}}_2, \hat{\mathbf{S}}_3)$. The eigenvalue of $\hat{\mathbf{S}}^2$ for spin- $\frac{1}{2}$ particles is $s(s+1) = \frac{3}{4}$. If the z -axis is the quantization axes, the particles can only be in the states $m = \pm\frac{1}{2}$ [46].

4.1.1. Spin- $\frac{1}{2}$ Particles

A spin- $\frac{1}{2}$ particle can be represented by a Pauli spinor [43]:

$$\chi = \begin{pmatrix} u \\ d \end{pmatrix}. \quad (4.1)$$

A particle with a spin pointing in z direction is described by $u = 1$ and $d = 0$. In quantum mechanics, the expectation value of an observable with the associated hermitian operator $\hat{\Omega}$, is defined as:

$$\langle \Omega \rangle = \langle \chi | \hat{\Omega} | \chi \rangle = \chi^\dagger \hat{\Omega} \chi. \quad (4.2)$$

The definition of the density matrix ρ :

$$\rho = |\chi\rangle \langle \chi| = \begin{pmatrix} |u|^2 & ud^* \\ u^*d & |d|^2 \end{pmatrix} \quad (4.3)$$

4. Spin Dynamics in Storage Rings

leads to a reformulation of the expectation value:

$$\langle \Omega \rangle = \text{Tr} \boldsymbol{\rho} \hat{\Omega}. \quad (4.4)$$

The hermitian operators corresponding to the quantum vectorial operator $\hat{\mathbf{S}}$ of a spin- $\frac{1}{2}$ particle are the Pauli matrices [47] defined as:

$$\hat{\mathbf{S}} = \frac{\hbar}{2} \vec{\sigma}, \quad (4.5)$$

with

$$\boldsymbol{\sigma}_1 = \begin{pmatrix} 0 & 1 \\ 1 & 0 \end{pmatrix}, \quad \boldsymbol{\sigma}_2 = \begin{pmatrix} 0 & -i \\ i & 0 \end{pmatrix}, \quad \boldsymbol{\sigma}_3 = \begin{pmatrix} 1 & 0 \\ 0 & -1 \end{pmatrix}. \quad (4.6)$$

In combination with the identity matrix $\boldsymbol{\sigma}_0 = \mathbf{1}$, the three Pauli matrices are a complete basis of the hermitian 2×2 matrices. The spin vector \vec{S} of one particle is defined as the expectation value of the corresponding operator:

$$\vec{S} = \langle \hat{\mathbf{S}} \rangle = \frac{\hbar}{2} \text{Tr} \boldsymbol{\rho} \vec{\sigma}. \quad (4.7)$$

A particle beam in an accelerator contains typically 10^{10} particles. The interesting quantity of such a beam is the expectation value of the spin observables of the particle ensemble. For an ensemble of N particles, the density matrix can be extended to

$$\boldsymbol{\rho} = \frac{1}{N} \begin{pmatrix} \sum_{n=1}^N |u^{(n)}|^2 & \sum_{n=1}^N u^{(n)} d^{(n)*} \\ \sum_{n=1}^N u^{(n)*} d^{(n)} & \sum_{n=1}^N |d^{(n)}|^2 \end{pmatrix} = \frac{1}{2} (\boldsymbol{\sigma}_0 + \vec{P} \vec{\sigma}). \quad (4.8)$$

In the last step, the density matrix is expanded in the Pauli matrices, where \vec{P} is the average over all spin vectors of the ensemble:

$$\vec{P} = \frac{1}{N} \sum_{n=1}^N \vec{S}_n. \quad (4.9)$$

The polarization vector is normalized to 1 and all three components are bounded by the limits ± 1 . For a beam containing $N^{m=\frac{1}{2}}$ and $N^{m=-\frac{1}{2}}$ particles in the corresponding spin states $m = \frac{1}{2}$ and $m = -\frac{1}{2}$, the vector polarization along the quantization axis reads [46]:

$$P_V = \frac{N^{m=\frac{1}{2}} - N^{m=-\frac{1}{2}}}{N^{m=\frac{1}{2}} + N^{m=-\frac{1}{2}}}. \quad (4.10)$$

The particle beam is fully polarized for $P_V = \pm 1$ and unpolarized for $P_V = 0$.

4.1.2. Spin-1 Particles

Spin-1 particles are characterized by a three dimensional spinor:

$$\chi = \begin{pmatrix} a_1 \\ a_2 \\ a_3 \end{pmatrix}, \quad (4.11)$$

where the three quantization states $m = -1, m = 0$, and $m = 1$ belong to the three components of the spinor. In analogy with the Pauli matrices, the spin-1 operators are defined as:

$$\hat{\mathbf{S}}_1 = \frac{\hbar}{\sqrt{2}} \begin{pmatrix} 0 & 1 & 0 \\ 1 & 0 & 1 \\ 0 & 1 & 0 \end{pmatrix}, \quad \hat{\mathbf{S}}_2 = \frac{\hbar}{\sqrt{2}} \begin{pmatrix} 0 & -i & 0 \\ i & 0 & -i \\ 0 & i & 0 \end{pmatrix}, \quad \hat{\mathbf{S}}_3 = \hbar \begin{pmatrix} 1 & 0 & 0 \\ 0 & 0 & 0 \\ 0 & 0 & -1 \end{pmatrix}. \quad (4.12)$$

Together with the identity matrix \mathbf{I} , the three operators comprise four out of nine matrices needed as basis for the 3×3 space. A commonly used definition of the missing five base operators is the standard Cartesian notation:

$$\hat{\mathbf{S}}_{ij} = 3\hat{\mathbf{S}}_i\hat{\mathbf{S}}_j - 2\delta_{ij}\mathbf{I} \text{ with } (i, j) \in \{1, 2, 3\}. \quad (4.13)$$

This set of ten operators is overcomplete and the relation:

$$\hat{\mathbf{S}}_{11} + \hat{\mathbf{S}}_{22} + \hat{\mathbf{S}}_{33} = 0 \quad (4.14)$$

reflects the dependency of the chosen basis operators. Commonly, the operators $\hat{\mathbf{S}}_i$ are normalized such that:

$$\text{Tr}\hat{\mathbf{S}}_i\hat{\mathbf{S}}_j = 3\delta_{ij} \quad (4.15)$$

holds. The density matrix for spin-1 particles can be extended as:

$$\rho = \frac{1}{3} \left[\mathbf{I} + \frac{3}{2} \sum_{i=1}^3 \mathbf{P}_i \mathbf{S}_i + \frac{1}{3} \sum_{i=1}^3 \sum_{j=1}^3 \mathbf{P}_{ij} \mathbf{S}_{ij} \right], \text{ with } \mathbf{P}_{ij} = \mathbf{P}_{ji}. \quad (4.16)$$

Considering a beam containing $N^{m=-1}$, $N^{m=0}$, and $N^{m=1}$ particles, the vector polarization P_V and the tensor polarization P_T with respect to the quantization axis are defined as:

$$P_V = \frac{N^{m=1} - N^{m=-1}}{N^{m=1} + N^{m=0} + N^{m=-1}}, \quad P_T = \frac{N^{m=1} + N^{m=-1} - 2N^{m=0}}{N^{m=1} + N^{m=0} + N^{m=-1}}. \quad (4.17)$$

4. Spin Dynamics in Storage Rings

A spin-1 particle beam can only be prepared in combinations of vector and tensor polarization. The maximum vector or tensor polarization is:

$$P_V = \pm \frac{2}{3} \text{ and } P_T = 0 \quad \text{or} \quad P_V = \pm \frac{1}{3} \text{ and } P_T = \pm 1. \quad (4.18)$$

4.2. Spin Motion in Storage Rings

After defining the polarization, the connections between the beam polarization, the polarization coordinate system and the Frenet-Serret coordinate system have to be defined. In addition, the spin motion under electric and magnetic fields is discussed in the following.

4.2.1. Coordinate Systems

The comoving Frenet-Serret coordinate system $(\vec{e}_x, \vec{e}_y, \vec{e}_z)$ is used to describe the motion of the particles within the accelerator. The spin of the particles is described in the Cartesian coordinates $(\vec{e}_1, \vec{e}_2, \vec{e}_3)$. Using the axis \vec{e}_y as the quantization axis \vec{e}_3 leads to a connection of the coordinates:

$$(\vec{e}_x, \vec{e}_y, \vec{e}_z) = (\vec{e}_1, -\vec{e}_3, \vec{e}_2). \quad (4.19)$$

4.2.2. Spin Motion in Rest Frame

In the rest frame of a particle, magnetic and electric fields act on the spin via the coupling with the magnetic dipole moment $\vec{\mu}$ and the electric dipole moment \vec{d} :

$$\frac{d\vec{S}}{dt} = \vec{\mu} \times \vec{B} + \vec{d} \times \vec{E} = \vec{\Omega}_s \times \vec{S}. \quad (4.20)$$

The magnetic and electric dipole moments are proportional to the spin [48]:

$$\vec{\mu} = \frac{g}{2} \frac{q}{m} \vec{S} \quad (4.21)$$

$$\vec{d} = \eta_{\text{EDM}} \frac{q}{2mc} \vec{S}. \quad (4.22)$$

The spin precesses in a plane, perpendicular to $\vec{\Omega}$ with a frequency of Ω . In a pure magnetic field the precession is called Larmor precession.

The precession of particles with velocity \vec{v} in a magnetic field has a similar form as (4.20):

$$\frac{d\vec{v}}{dt} = -\frac{q}{m}\vec{B} \times \vec{v} = \vec{\Omega}_{\text{cyc}} \times \vec{v}. \quad (4.23)$$

The relative frequency difference is the gyromagnetic anomaly G or a :

$$\frac{\Omega_{\text{cyc}} - \Omega_s}{\Omega_{\text{cyc}}} = \frac{g - 2}{2} = G = a, \quad (4.24)$$

where G is usually used in the hadronic sector and a is used in the leptonic sector. For ideal Dirac particles without any inner structure, the g factor is 2 and the gyromagnetic anomaly vanishes [49]. Higher order corrections from for example quantum electrodynamics lead to corrections, which can be measured with high accuracy in the $g - 2$ experiments. The measured values of the gyromagnetic anomaly are summarized in Tab. 4.1.

Table 4.1.: *The measured values of the gyromagnetic anomaly for the muon, the electron, the proton, and the deuteron. [50]*

particle	Magnetic moment anomaly G
muon	$(1.165\,920\,89 \pm 0.000\,000\,63) \cdot 10^{-3}$
electron	$(1.159\,652\,180\,91 \pm 0.000\,000\,000\,26) \cdot 10^{-3}$
proton	$1.792\,847\,351 \pm 0.000\,000\,009$
deuteron	$-0.142\,987\,272\,4 \pm 0.000\,000\,001\,5$

4.2.3. Relativistic Particles

The discussed equation of spin motion is valid in the rest frame of the particle, but in an accelerator the electromagnetic fields are known in the laboratory frame. In order to describe the spin motion, a Lorentz transformation of the fields in the rest frame of the particle is needed. The resulting equation of the spin motion has the same form as the discussed Larmor precession (4.20), only the angular momentum vector is different.

The result is referred to as the Thomas-Bargmann-Michel-Telegdi (T-BMT)

4. Spin Dynamics in Storage Rings

equation [45, 51, 52, 48]:

$$\frac{d\vec{S}}{dt} = -\left(\vec{\Omega}_{\text{MDM}} + \vec{\Omega}_{\text{EDM}}\right) \times \vec{S}, \quad \text{with} \quad (4.25)$$

$$\vec{\Omega}_{\text{MDM}} = \frac{q}{m} \left[\left(G + \frac{1}{\gamma}\right) \vec{B} - \frac{G\gamma}{\gamma+1} (\vec{\beta} \cdot \vec{B}) \vec{\beta} - \left(G + \frac{1}{1+\gamma}\right) \vec{\beta} \times \frac{\vec{E}}{c} \right], \quad (4.26)$$

$$\vec{\Omega}_{\text{EDM}} = \frac{q}{mc} \frac{\eta_{\text{EDM}}}{2} \left[\vec{E} - \frac{\gamma}{\gamma+1} (\vec{\beta} \cdot \vec{E}) \vec{\beta} + c\vec{\beta} \times \vec{B} \right]. \quad (4.27)$$

Neglecting the EDM and assuming an ideal accelerator, where only the magnetic guiding field exists and the velocity is always perpendicular to this field, leads to:

$$\frac{d\vec{S}}{dt} = -\frac{q}{m\gamma} (G\gamma + 1) B_y \vec{e}_y \times \vec{S}. \quad (4.28)$$

A spin, which is parallel to the guiding field stays stable in time, this direction is called the stable spin axis \vec{n}_0 . Spins, which are not aligned with the stable spin axis, precess around this axis with the frequency Ω_{MDM} . For a realistic accelerator with transverse field components, the stable spin axis changes its orientation (4.25).

Besides the spin precession, the momentum vector rotates with the frequency $\Omega_{\text{cyc}} = \frac{q}{m\gamma}$, resulting by solving the Lorentz force equation (3.1):

$$\frac{d\vec{p}}{dt} = \frac{q}{m\gamma} p_z \vec{e}_z \times B_y \vec{e}_y. \quad (4.29)$$

The number of spin revolutions per particle revolution can be expressed as the spin tune ν :

$$\nu = \frac{\frac{q}{m\gamma} (\gamma G + 1)}{\frac{q}{m\gamma}} - 1 = \gamma G. \quad (4.30)$$

One revolution is subtracted, since the spin tune is defined in the comoving coordinate system, which itself precesses once per particle turn with respect to the laboratory frame.

5. Accelerator Complex around COSY

The accelerator COSY, COoler SYnchrotron, at Forschungszentrum Jülich provides polarized protons or deuterons for experiments. With its capabilities of cooling and beam manipulating, COSY is a perfect environment to investigate tools and systems, needed for a dedicated EDM storage ring. This chapter describes the accelerator and the EDDA detector, used as polarimeter.

5.1. COSY - Cooler Synchrotron

The accelerator complex around COSY at Forschungszentrum Jülich consists of two ion sources, the cyclotron JULIC¹, the Cooler Synchrotron COSY itself and beam lines as interconnections. A schematic drawing of the accelerator COSY, its internal experimental areas and the pre-accelerator JULIC is shown in Fig. 5.1.

The two ion sources provide either negatively charged hydrogen or deuterium, both polarized or unpolarized [53]. The negatively charged particles are transported towards the cyclotron JULIC. The cyclotron accelerates the ions up to a kinetic energy of 45 MeV and 75 MeV, for the H^- and D^- ions resp. [54]. After the pre-acceleration, the particle beam is injected into the COSY ring via stacked stripping injection. The typical intensity is in the range between 10^9 and 10^{10} particles per fill.

The main accelerator and storage ring COSY [55, 56] is 184 m long and provides beam momenta from 300 MeV/c to 3.7 GeV/c. Two electron coolers are available. The 100 keV e-cooler is able to cool the beam up to a momentum of 600 MeV/c for protons and 1200 MeV/c for deuterons [57]. The 2 MeV e-cooler, installed in 2013, is able to cool the beam up to the maximum momentum accessible with COSY [58]. In addition, stochastic cooling is possible, starting from 1.5 GeV/c [59].

Besides the cooling systems, diagnostic systems are available. The diagnostic systems include a beam profile monitor to measure the transverse beam profile, by using residual gas ionization [60]. The transverse beam position is measured

¹JULIC - Jülich Light Ion Cyclotron

5. Accelerator Complex around COSY

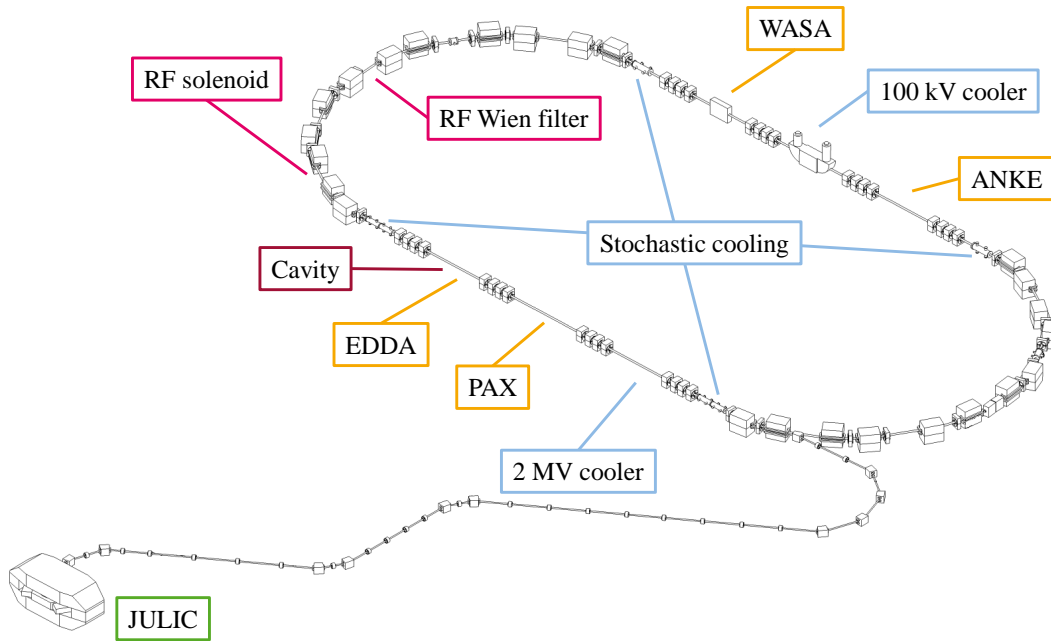


Figure 5.1.: Sketch of the COSY storage ring, the cyclotron JULIC and the injection beamline. The experimental areas are marked in orange, the cooling devices are depicted in blue. The currently installed RF spin manipulators drawn in magenta. The accelerating and bunching cavity is directly placed behind the EDDA detector.

at several places around the ring with beam position monitors, which are described in more detail in chapter 6. The beam intensity is estimated with a beam current transformer [61].

In addition to the mentioned systems, devices to manipulate the polarization are placed at COSY. For example, a RF solenoid [62] and a RF Wien filter [63] are installed. Among others, these devices are used to cross depolarizing resonances by flipping the polarization by 180° . By using a flip around 90° , the polarization is transferred from the vertical direction in the horizontal plane [64, 65].

In order to perform particle physics experiments, four internal experimental places, where targets and particle detectors can be installed are available: PAX², EDDA³, WASA⁴, and ANKE⁵. The four names are the names of the experi-

²PAX - Polarized Antiproton eXperiments

³EDDA - Excitation function Data acquisition Designed for Analysis of phase shifts

⁴WASA - Wide Angle Shower Apparatus

⁵ANKE - Apparatus for Studies of Nucleon and Kaon Ejectiles

ments performed at these places [66, 67, 68, 69]. For the experiments done to investigate the feasibility of EDM measurements at COSY, the EDDA detector is used to measure the polarization. This allows for determination of the spin precession frequency f_s .

5.2. EDDA Polarimeter

As mentioned, the EDDA detector is used as a polarimeter. The polarization of the particle beam is measured by analyzing the angular distribution of elastically scattered protons or deuterons. Upstream the EDDA detector, a carbon block is mounted as a target slightly above the center of the beam pipe. In order to hit the target with particles, different methods can be applied. One method is to move the beam slowly onto the target by creating a local orbit bump with corrector magnets. Another way is to heat the beam vertically by applying an RF electric field on a strip-line unit. The amplitude of the field is white noise distributed around a betatron sideband frequency. By using these mechanisms, the beam is slowly extracted during a time period of typically 100 s to 1000 s.

The cross section σ for the elastically scattered spin $\frac{1}{2}$ -particles depends on the polarization and reads [44]:

$$\sigma(\varphi, \theta) = \sigma_0(\theta) \cdot (1 + A_y P_y \cos \varphi - A_x P_x \sin \varphi), \quad (5.1)$$

where $P_{x,y}$ are the polarization components in vertical and radial direction, $A_{x,y}$ are the corresponding analyzing powers, and φ is the azimuthal angle in the $x - y$ -plane. The cross section for an unpolarized beam is given by σ_0 . The analyzing power depends on the polar scattering angle θ , the target material, the particle species and its momentum. A schematic view of the scattered particle and the variables is given in Fig. 5.2.

For spin 1-particles, the corresponding cross section is given by [44]

$$\begin{aligned} \sigma(\varphi, \theta) = \sigma_0(\theta) \cdot & \left[1 + \frac{1}{2} A_{zz} P_{zz} + \left(\frac{3}{2} A_y P_y + \frac{2}{3} A_{xz} P_{xz} \right) \cos \varphi \right. \\ & + \frac{1}{6} (A_{xx} - A_{yy}) (P_{xx} - P_{yy}) \cos(2\varphi) \\ & + \left(-\frac{3}{2} A_x P_x + \frac{2}{3} A_{xz} P_{xy} \right) \sin \varphi \\ & \left. + \frac{1}{3} (A_{xx} - A_{yy}) P_{xy} \sin(2\varphi) \right]. \end{aligned} \quad (5.2)$$

In addition to the vector polarization P_i with $i \in x, y$, the tensor polarization P_{ij} and the corresponding analyzing power A_{ij} with $i, j \in x, y, z$ are considered.

5. Accelerator Complex around COSY

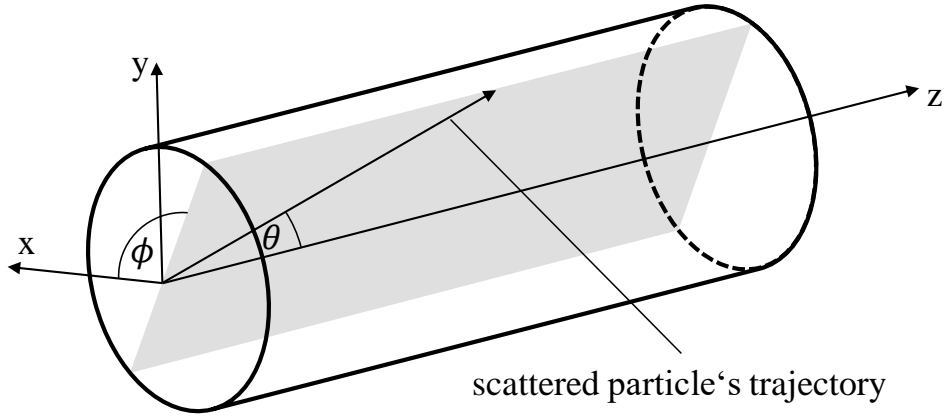


Figure 5.2.: Definition of the scattering angles φ and θ .

For a beam with vanishing tensor polarization, as used for the experiments presented within this thesis, the cross section simplifies to:

$$\sigma = \sigma_0 \left[1 + \frac{3}{2} A_y P_y \cos \varphi - \frac{3}{2} A_y P_x \sin \varphi \right]. \quad (5.3)$$

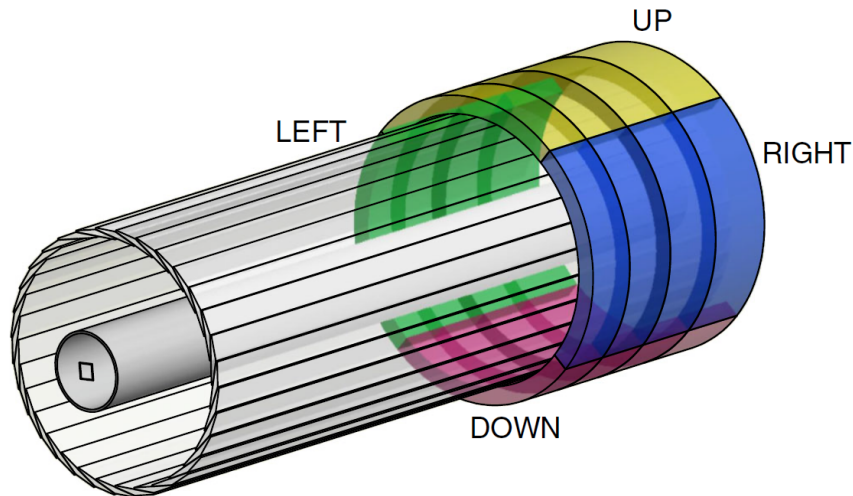


Figure 5.3.: The sketch of the EDDA detector shows the scintillating bars and rings. The four groups which are used for polarization measurements are colored [70].

The polarization of the beam can be measured by analyzing the angle dependence of the scattered particles, which is done with the EDDA detector. It consists of 32 scintillating bars mounted cylindrically around the beam pipe.

On top of the bars and perpendicular to them, half rings are installed. The last four half rings and eight bars, covering the angle range $9^\circ \leq \theta \leq 14.4^\circ$ and $\Delta\varphi = 90^\circ$ are grouped. The complete azimuthal range is covered by four groups, namely Up, Right, Down and Left. A sketch of the detector and the four groups is given in Fig. 5.3. For each group, covering the angle range Ω , an effective analyzing power can be calculated:

$$\overline{A}_y^s = \frac{\int A_y(\theta) \sin \varphi d\Omega}{\int d\Omega} \quad (5.4)$$

$$\overline{A}_y^c = \frac{\int A_y(\theta) \cos \varphi d\Omega}{\int d\Omega}. \quad (5.5)$$

Assuming perfectly aligned detectors with the same efficiency for all elements, the vertical and radial polarization can be calculated by estimating the asymmetries in the count rates N in the detector quadrants Left-Right and Up-Down:

$$P_y = \frac{2}{3\overline{A}_y^{c,L}} \frac{N_L - N_R}{N_L + N_R} \quad (5.6)$$

$$P_x = \frac{2}{3\overline{A}_y^{s,U}} \frac{N_U - N_D}{N_U + N_D}, \quad (5.7)$$

where $\overline{A}_y^{c,L}$ and $\overline{A}_y^{s,U}$ are the averaged analyzing powers for the Left and Up detectors resp.

By using a so called time stamping of all detected events, which enables an assignment of a turn number to the scattered event, it is possible to measure the radial polarization depending on the turn number [70]. In classical scattering experiments, the time stamping is not important, since all events are mostly analyzed independently. For the experiments described in this thesis, the precise time information is important, since this allows to analyze the evolution of the polarization from turn to turn (1 μ s) and on long term basis (1000 s). With this technique, it is possible to measure the spin precession frequency, which results in a time dependent horizontal polarization:

$$P_x(t) = P_{x,0} \sin(\omega_s t) \approx P_{x,0} \sin(\gamma G \omega_{\text{rev}} t), \quad (5.8)$$

where ω_{rev} is the revolution frequency of the beam. The frequency of the horizontal polarization is determined by analyzing the Fourier spectra of the detected events [71, 72].

6. Beam Position Monitor System at COSY

This chapter introduces the existing BPM system at COSY. First of all, commonly used BPMs are described, followed by the definition of uncertainties, which influence a beam position measurement. Besides the physical monitor device, the readout electronics with its capabilities and limits with respect to the orbit correction is described. The chapter closes with an empirical description and error analysis of the existing BPM system.

6.1. Commonly used BPMs

In accelerators the transverse beam position along the particle trajectory is one of the important beam parameters. This parameter is measured by BPMs. For circular accelerators usually two systems are used: button BPMs or shoebox BPMs. Both systems measure the electric field of the passing, bunched particle beam. The beam position is calculated by analyzing the measured electric field distribution. Button BPMs are used at electron machines, whereas shoebox BPMs are used at hadron accelerators. Since COSY is a hadron accelerator, this chapter focuses on the shoebox design.

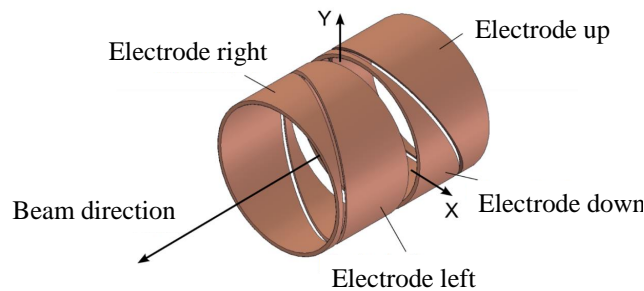


Figure 6.1.: *Sketch of a round BPM, which measures the vertical and horizontal beam position, adopted from [73].*

Figure 6.1 is the sketch of a round shoebox BPM. It consists of two pairs of electric pickup electrodes, one for each plane. The dimensions of the BPM have

6. Beam Position Monitor System at COSY

to fit to the beam pipe of the accelerator. At COSY, two types of BPMs are installed [61]:

Round BPMs with a length of $l = 100$ mm and a diameter $d = 150$ mm are installed in the straight sections.

In the arcs, where the beam pipe is rectangular, rectangular BPMs are installed. Their dimensions are: length $l = 100$ mm, height $h = 60$ mm and width $w = 150$ mm.

In both BPM types, the passing beam induces a voltage in each electrode. The shoebox design with a diagonal cut of the two electrodes lead to linear dependence between this voltage and the the beam positions x, y with respect to the center of the BPM:

$$U_{L,R} = \frac{q_B l \left(1 \pm \frac{x}{d}\right)}{C} \quad (6.1)$$

$$U_{U,D} = \frac{q_B l \left(1 \pm \frac{y}{d}\right)}{C}, \quad (6.2)$$

where l, d and C are the BPM parameters length, diameter and capacitance. For the rectangular BPMs, the diameter has to be replaced by the width or the height of the BPM. The $+$ sign is used for the electrodes positioned left and up of the beam pipe center, whereas the $-$ sign is used for the two other electrodes. The variable q_B is the charge density. In first order, it is given by:

$$q_B = \frac{Nq}{L}, \quad (6.3)$$

where N is the number of particles, L the bunch length and q the particle's charge.

By calculating the ratio of the difference and sum of the signals, measured at opposite electrodes, all parameters besides the position and the diameter drop out. The beam position reads:

$$x = \frac{d}{2} \cdot \frac{U_L - U_R}{U_L + U_R}, \quad y = \frac{d}{2} \cdot \frac{U_U - U_D}{U_U + U_D}, \quad (6.4)$$

where the indexes L, R, U, D indicate the position of the electrodes left, right, up or down. For the rectangular BPM the position dependence is given by:

$$x = \frac{w}{2} \cdot \frac{U_L - U_R}{U_L + U_R}, \quad y = \frac{h}{2} \cdot \frac{U_U - U_D}{U_U + U_D}. \quad (6.5)$$

The detailed calculations are discussed in [74, 75]. Besides the linear response of the BPMs, which is ensured by design, the uncertainties of the measurement

are important for the EDM measurement. Sources of these uncertainties are discussed in the upcoming section.

6.2. Uncertainties of Beam Position Measurements

The ideal BPM measures the beam position with high resolution and a perfect accuracy. This means, that the spread in the position measurement with a stable beam is minimal (resolution). In addition, the measured beam position should be the same as the true one (accuracy). Figure 6.2 depicts the two definitions in a descriptive way.

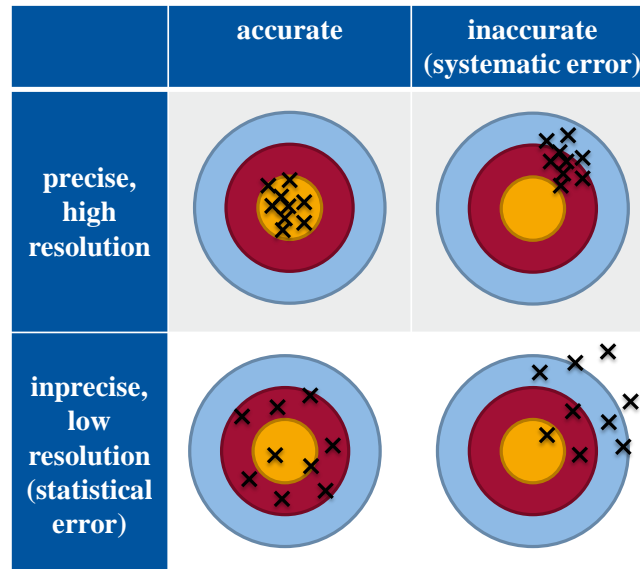


Figure 6.2.: *Descriptive sketch of the definitions accuracy and precision/resolution.*

The accuracy of the beam position measurement depends on the alignment accuracy of the BPM itself and the manufacturing accuracy. The resolution of the BPM as a hardware device depends on the noise on the electrodes. In addition to these effects, the accuracy and resolution of the readout electronics, including the signal processing chain, has to be considered.

For the EDM measurement in Wien filter mode, the BPM system should provide accurate and precise data. For a measurement setup with beam based calibration of the BPMs or with two counter rotating beams, the BPMs have to be precise, but to first order the accuracy drops out.

6.2.1. Resolution Limited by Thermal Noise

The theoretical limit of the resolution of the BPMs is the thermal noise of the BPM, including the pre-amplifiers. The thermal noise is given by the Johnson-Nyquist theorem:

$$\overline{U_{\text{noise}}^2} = 4Rk_{\text{B}}T\Delta f, \quad (6.6)$$

where R is the resistance, T the temperature, k_{B} the Boltzmann's constant and Δf the band width of the system. For a combination of capacity, inductance and resistor, R needs to be replaced by the real part of the admittance. The admittance Y as a function of the frequency for the pre-amplifier and the capacitive electrode reads [76, chap. 3]:

$$Y(f) = \frac{1}{R + \frac{i}{2\pi fC}}. \quad (6.7)$$

Integrating around the beam frequency of f_0 with a width of Δf results in the thermal noise:

$$U_{\text{noise}} = \sqrt{4k_{\text{B}}T \int_{f_0 - \Delta f/2}^{f_0 + \Delta f/2} \text{Re}(Y(f)) df} \quad (6.8)$$

$$= \sqrt{\frac{4k_{\text{B}}T}{\pi C} \arctan(2\pi fRC) \Big|_{f_0 - \Delta f/2}^{f_0 + \Delta f/2}}. \quad (6.9)$$

The resistance of the pre-amplifiers is $R_{\text{pre}} = 500 \text{ k}\Omega$. The BPM electrodes have a capacitance of $C_{\text{electrode}} = 80 \text{ pF}$. Assuming a temperature of $T = 300 \text{ K}$ and a broad band filter with a width of $\Delta f = 100 \text{ kHz}$ around the beam frequency of $f_0 = 750 \text{ kHz}$, the noise is calculated to $U_{\text{noise}} = 28 \text{ }\mu\text{V}$. This voltage has to be compared to the signal level of the electrodes, given by (6.2). The induced voltages for a centered beam with a typical bunch length of 40 m are calculated to:

$$U_{\text{L,R}} = \begin{cases} 90 \text{ mV} & N = 1.8 \cdot 10^{10} \text{ particles} \\ 1.9 \text{ mV} & N = 3.8 \cdot 10^8 \text{ particles} \end{cases}. \quad (6.10)$$

Using Gaussian error propagation for (6.4) and assuming an average of 256 measurements results in the position noise limit of the BPMs:

$$\sigma_{x,\text{noise}} = \begin{cases} 0.2 \text{ }\mu\text{m} & N = 1.8 \cdot 10^{10} \text{ particles} \\ 11 \text{ }\mu\text{m} & N = 3.8 \cdot 10^8 \text{ particles.} \end{cases} \quad (6.11)$$

In addition to this thermal limit, the noise of the readout electronics has to be considered.

In order to minimize the thermal noise, a project to develop BPMs, based on measuring the magnetic field distribution of the particle beam by using so called Rogowski pickup coils [77], readout with SQUIDS (Superconducting QUantum Interference Device) is ongoing [78]. The beam position resolution of such a device will be in the order of nm.

6.2.2. Readout Electronics

The COSY BPM readout electronics start directly at the electrodes with a pre-amplifier, which amplifies each signal by $g_{\text{pre}} = (13.5 \pm 0.1)$ dB [79]. The amplified signal is fed in an analog electronics device [80], where the high frequency signals are mixed with the revolution frequency and filtered by a band-pass filter. After these processing steps, the difference Δ_A and the sum Σ_A of the signals are generated. The resulting voltages are amplified with adjustable amplification gains g_Δ , and g_Σ . At the end, the amplified voltages are digitized [81] with an 8 bit ADC (Analog to Digital Converter) for the difference and a 7 bit ADC for the sum. Both ADCs accept a maximum input voltage of 1 V. The complete readout chain can be expressed mathematically by:

$$U_{\text{P,L}} = 10^{\frac{g_{\text{pre}}}{20}} U_L, \quad U_{\text{P,R}} = 10^{\frac{g_{\text{pre}}}{20}} U_R \quad (6.12)$$

$$\left. \begin{aligned} \Delta_A &= 10^{\frac{g_\Delta}{20}} (U_{\text{P,R}} - U_{\text{P,L}}) \\ \Sigma_A &= 10^{\frac{g_\Sigma}{20}} (U_{\text{P,R}} + U_{\text{P,L}}) \end{aligned} \right\} \text{analog} \quad (6.13)$$

$$\left. \begin{aligned} \Delta_D &= \frac{\Delta_A}{1\text{V}} \cdot 256 \\ \Sigma_D &= \frac{\Sigma_A}{1\text{V}} \cdot 128 \end{aligned} \right\} \text{digital}. \quad (6.14)$$

Typically, the digitized sum and difference signals are averaged over 4 ms, which corresponds to 256 datapoints. After all the processing steps, the beam position is calculated out of the digitized voltages by using (6.4):

$$x = \frac{d U_L - U_R}{2 U_L + U_R} \quad (6.15)$$

$$= \frac{d}{2} 10^{\frac{g_\Sigma - g_\Delta}{20}} \frac{\Delta_D}{\Sigma_D} \frac{1}{2}. \quad (6.16)$$

In the following, the resolution and accuracy of the readout system are discussed.

Resolution

The resolution of the position measurement can be calculated by Gaussian error propagation with the knowledge of the width of the digitized signals σ_{Δ_D} and

6. Beam Position Monitor System at COSY

σ_{Σ_D} . The statistical uncertainty on the beam position reads:

$$\sigma_{x,\text{stat.}} = x \cdot \sqrt{\frac{\sigma_{\Delta_D}^2}{\Delta_D} + \frac{\sigma_{\Sigma_D}^2}{\Sigma_D}} \quad (6.17)$$

$$= \frac{d}{2} 10^{\frac{g_{\Sigma} - g_{\Delta}}{20}} \frac{\Delta_D}{\Sigma_D} \frac{1}{2} \cdot \sqrt{\frac{\sigma_{\Delta_D}^2}{\Delta_D} + \frac{\sigma_{\Sigma_D}^2}{\Sigma_D}}. \quad (6.18)$$

The resolution of the digitizers is in the order of $2 \text{ LSB}^1 \approx 8 \text{ mV}$, which results in the resolution of the mean value of 0.5 mV for the difference signal and 1 mV for the sum signal. A distribution of the digitized difference and sum signals, measured with one BPM at COSY with a beam containing $2.9 \cdot 10^9$ particles is presented in Fig. 6.3.

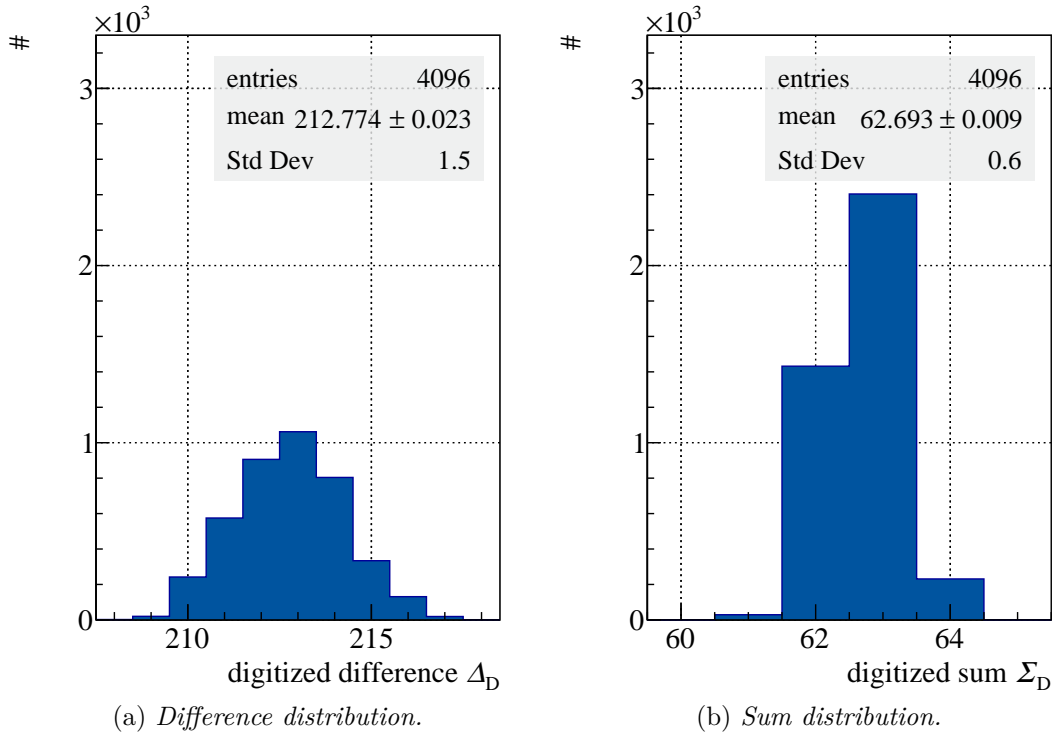


Figure 6.3.: Measured distributions of the digitized difference (a) and sum (b) signals for $2.9 \cdot 10^9$ particles. The settings of the electronics are: $g_{\Delta} = 48 \text{ dB}$, $g_{\Sigma} = 24 \text{ dB}$, and $\Delta f = 10 \text{ kHz}$. The measured beam position is calculated to $x = (14.4710 \pm 0.0025) \text{ mm}$.

The estimated resolution of the position for $1.8 \cdot 10^{10}$ particles and $3.8 \cdot 10^8$ particles depending on the beam position is shown in Fig. 6.4 as blue resp. red curve. Since the digitization range is limited, the gains of the analog signal

¹LSB - Least Significant Bit

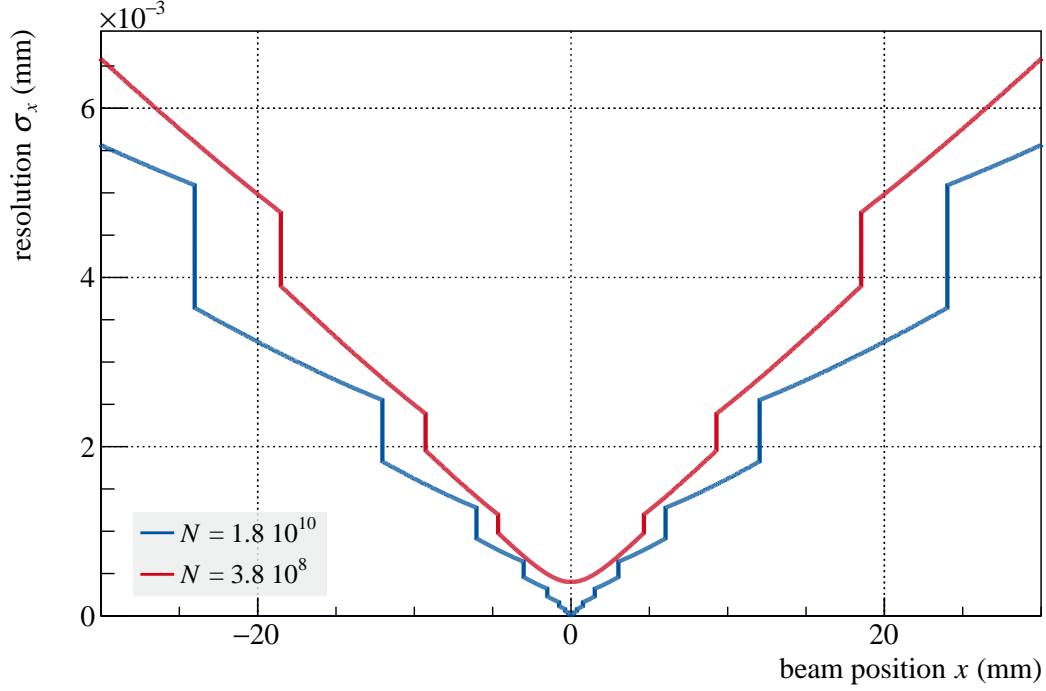


Figure 6.4.: Resolution of the BPM system, depending on the beam position x and on the number of particles N . The steps occur, because the gain of the difference signal processing has to be adjusted. The difference between the red and blue curve is a result of the limited gain of the difference signal chain, which is already reached at ± 5 mm for $3.8 \cdot 10^8$ particles.

processing have to switch depending on the beam position (g_{Δ}) and depending on the number of particles (g_{Σ} , g_{Δ}). The switching of the difference gain results in the steps of the curves. For the red curve, the maximum gain is already reached at a position of ± 5 mm which results in the shown limit on the resolution of $3.5 \mu\text{m}$. For beams with more particles, this limit is going down below $1 \mu\text{m}$.

Compared to the thermal noise, the resolution of the signal processing electronics is for low number of particles lower than the thermal noise and can be neglected. For high number of stored particles, the resolution of the electronics is the dominating effect.

As a conclusion of the discussed effects, the BPM system provides beam position measurements with a resolution in the order of $1 \mu\text{m}$ for 10^9 particles. This resolution corresponds to an EDM sensitivity of roughly $10 \cdot 10^{-22} e \text{ cm}$, by using the results presented in Tab. 2.1.

These values are achievable by transferring all data points to the control system.

6. Beam Position Monitor System at COSY

Because of limited bandwidth in the existing network, the beam position is averaged directly in the electronics and rounded to 0.01 mm. This rounding error is the limiting factor in the fast acquisition mode of the BPMs. Besides this rounding, the accuracy of the system has to be taken into account.

Accuracy

The accuracy of the readout can be calculated by using the accuracy of the parts of the electronics. The uncertainty of the switchable gains for example is in the specification set to $\sigma_g = \pm 0.5$ dB. Using this number and estimating the error on the position leads to:

$$\sigma_{x,\text{sys}} = |x| \sqrt{2} \left(\frac{1}{20} \log(10) \sigma_g \right) \quad (6.19)$$

$$= \frac{d}{2} 10^{\frac{g_{\Sigma} - g_{\Delta}}{20}} \frac{|\Delta_D|}{\Sigma_D} \frac{1}{2} \cdot \sqrt{2} \left(\frac{1}{20} \log(10) \sigma_g \right). \quad (6.20)$$

In addition, the difference digitizer measures always some small voltage offset for an input of 0 V, which results in an offset of ≈ 10 LSB. Considering both effects and calculating the accuracy with respect to the beam position for $1.8 \cdot 10^{10}$ particles and $3.8 \cdot 10^8$ particles results in the blue and red curves, shown in Fig. 6.5. The resulting accuracy is three orders of magnitude worse than the resolution of the system. The curve corresponding to $3.8 \cdot 10^8$ particles shows around the zero position a flat line. This limit occurs due to the effect of an offset in the difference digitizer and the limit in the difference gain settings. This effect can be displayed by calculating the measured beam position, including the mentioned offset, against the true beam position. Figure 6.6 provides the curves for $1.8 \cdot 10^{10}$ particles and $3.8 \cdot 10^8$ particles.

Excluding the center position, the measured position corresponds to the true beam position. In the center, the measured position converges against a limit and a blind spot appears. This blind spot depends on the offset introduced by the electronics and is different for each readout set. For later use of measured data, an empirical function, describing this blind spot with two parameters x_{offset} and x_{lin} is used:

$$x_{\text{meas}}(x_{\text{true}}) = \begin{cases} x_{\text{true}} & x_{\text{true}} < -x_{\text{lin}} \\ -x_{\text{offset}} - (x_{\text{true}} - x_0)^2 \cdot a & -x_{\text{lin}} \leq x_{\text{true}} < -x_0 \\ -x_{\text{offset}} & -x_0 < x_{\text{true}} \leq 0 \\ +x_{\text{offset}} & 0 < x_{\text{true}} \leq x_0 \\ +x_{\text{offset}} + (x - x_0)^2 \cdot a & x_0 < x_{\text{true}} \leq x_{\text{lin}} \\ x_{\text{true}} & x_{\text{true}} > x_{\text{lin}} \end{cases}. \quad (6.21)$$

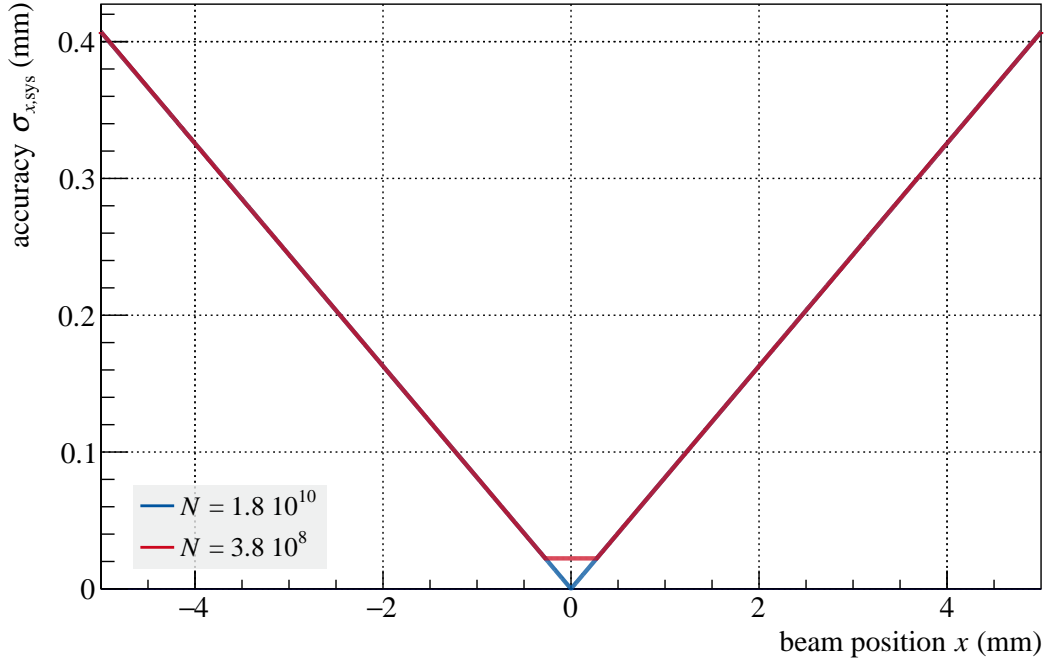


Figure 6.5.: Achievable accuracy taking the uncertainty on the gains as error source.

The coefficients a and x_0 are:

$$x_0 = 2x_{\text{offset}} - x_{\text{lin}} \quad (6.22)$$

$$a = \frac{x_{\text{lin}} - x_{\text{offset}}}{(x_{\text{lin}} - x_0)^2}. \quad (6.23)$$

The parameter x_0 is the lower limit of the measured beam position, whereas the parameter x_{lin} is the true beam position, where the linear part of the function starts. The transition between both parts is described by a second order polynomial to provide a continuously differentiable function $\forall x_{\text{true}} \neq 0$.

In addition to the discussed error sources, the alignment of the BPM itself, the adjustment of the pre-amplifiers and the calibration factor of the BPM are systematic error sources. These sources have to be added to the discussed one of the gains.

In summary, an optimistic estimator for the accuracy by using the existing readout is 0.1 mm.

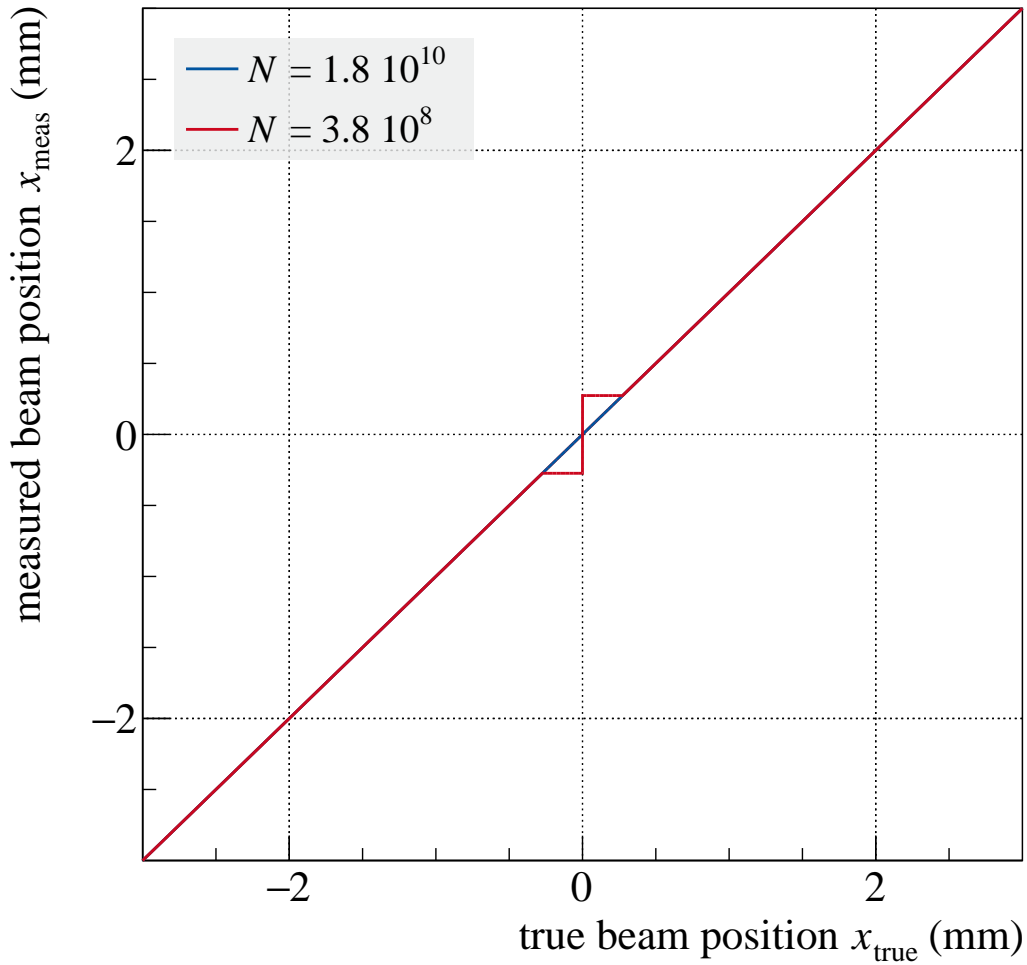


Figure 6.6.: *Function describing the relation between the true beam position and the measured beam position.*

6.3. Planned Upgrade of the Readout Electronics

For the year 2017 an upgrade of the readout electronics for all BPMs is planned. The new system Libera Hadron²[82] will digitize the voltages of the two electrodes directly after amplification with a fixed pre-amplifier. With this new setup, the discussed problem of the blind spot and the gain switching will disappear. The resolution of the new system will be in the order of $4 \mu\text{m}$ for a perfectly matched pre-amplified signal [83, p. 11].

The accuracy of the alignment and the one of the calibration will stay and

²Libera Hadron: High performance beam position monitor electronics for hadron circular machines.

6.3. Planned Upgrade of the Readout Electronics

have to be addressed separately. One option to get the calibration factor is to use the Linear Optics from Closed Orbits (LOCO) algorithm [84]. The LOCO algorithm is based on a fit of a simulated orbit response matrix to a measured one. The parameters which are varied are usually the quadrupole strength, the BPM and corrector magnet calibrations, as well as BPM rolls. A first implementation of LOCO for COSY is presented in [85].

For the advanced method of using clockwise and counterclockwise rotating beams, the accuracy is not important, since only relative beam position measurements are necessary. A statistical uncertainty of $4\text{ }\mu\text{m}$ in the RMS of the difference of the two orbits results in a polarization buildup of $\Delta S_y \approx 10^{-12}$ per turn [32], which is similar to the buildup due to an EDM of $d_{\text{EDM}} \approx 10^{-22} e\text{ cm}$ [16]. For the mentioned development of Rogowski pick-ups and a SQUID readout, the EDM uncertainty will shrink proportional to the gain in resolution.

7. Orbit Response Matrix

The Orbit Response Matrix (ORM) is the response of the beam position at all BPMs for a change in one of the corrector magnets. This response depends on the optical functions of the accelerator lattice and can be calculated by using the β functions, the dispersion and the phase advances between the corrector magnets and BPMs. Besides the calculation by using this information, the matrix can be measured directly. One way of measuring this matrix is to measure the change in the beam position depending on the change of a single corrector magnet. Repeating this procedure consecutively for all magnets results in a complete ORM. In the following a newly developed software to measure the ORM at COSY including a detailed analysis of the measured data points is presented. The measured ORM can later be used to correct the orbit or to match the model ORM to the measured one by applying the LOCO algorithm mentioned in chapter 6.3 and described in [85]. The orbit correction algorithm is described in section 7.3.

7.1. Measurement Software

In order to provide the ORM measurement, the software needs to be connected to the corrector magnets, the timing system and the BPMs. All the listed systems are accessible via Ethernet. The connection to the corrector magnets is used to change the deflection angle. After receiving a trigger from the timing system, the BPMs send their measurements to the software. The data are correlated to the applied kick angle with the help of timestamps, provided by the timing system.

In addition to the hardware devices, the software uses an existing interface to a database, which stores information about the conversion between physical units (deflection angle) and technical units (current in the magnet). For data storage and analysis the ROOT framework [86] is used. A schematic layout of the software architecture is given in Fig. 7.1.

The procedures to set the magnet strengths, the BPM triggers as well as the timing system connections are described in the following.

7. Orbit Response Matrix

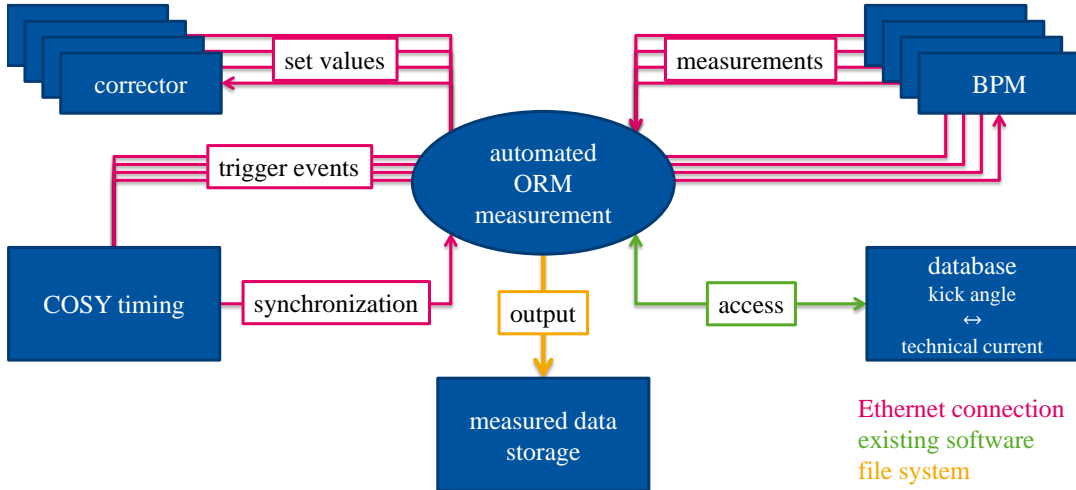


Figure 7.1.: *The ORM measurement software is connected via Ethernet to the corrector magnets, the BPMs, and the COSY timing system. Calibration information about the corrector magnets are accessible from a database through an existing software interface. These information are used to control the corrector magnets. The timing system triggers the BPM measurement. The measured BPM data are received, combined with the timing information and stored on disk in the ROOT file format for a later ORM calculation.*

7.1.1. Corrector Magnet Settings

The kick angle of one corrector magnet can be calculated by using (3.7):

$$\theta = \frac{1}{B\rho} \int B_{\text{cor}} ds.$$

The magnetic field B_{cor} is a function of the current in the coil of the magnet. This dependence is approximated by a linear function. In addition the integral is replaced by an effective field. Both approximations lead to:

$$\theta = \frac{1}{B\rho} \frac{1}{f_{\text{calib}}} \cdot I \quad (7.1)$$

$$\Leftrightarrow I = f_{\text{calib}} \cdot B\rho \cdot \theta. \quad (7.2)$$

Equation (7.2) is used to transform between technical current changes and the physical kick angle, which bends the particle trajectory. The calibration factors f_{calib} are unique for each magnet and stored in the database.

All corrector magnets at COSY are connected to single, independent power supplies. These power supplies are controlled by function generators producing

a bit pattern, which represents the set value of the current. This bit pattern is modified to apply the corrector magnet change $\Delta\theta_{\text{step},i}$ for magnet i . A typical change of the corresponding current ΔI is shown in Fig. 7.2. The trigger events for the BPM measurements are indicated on top of the current run.

The smallest step size is given by the digital resolution of the power supplies, which is:

$$\sigma_{I,\text{dig}} = \frac{1}{2047} \cdot I_{\text{max}}. \quad (7.3)$$

But the measured stability is a factor two worse [87]:

$$\sigma_I = \frac{2}{2047} \cdot I_{\text{max}} = 0.1\% \cdot I_{\text{max}}. \quad (7.4)$$

Later on, this uncertainty is considered in the calculation of the ORM.

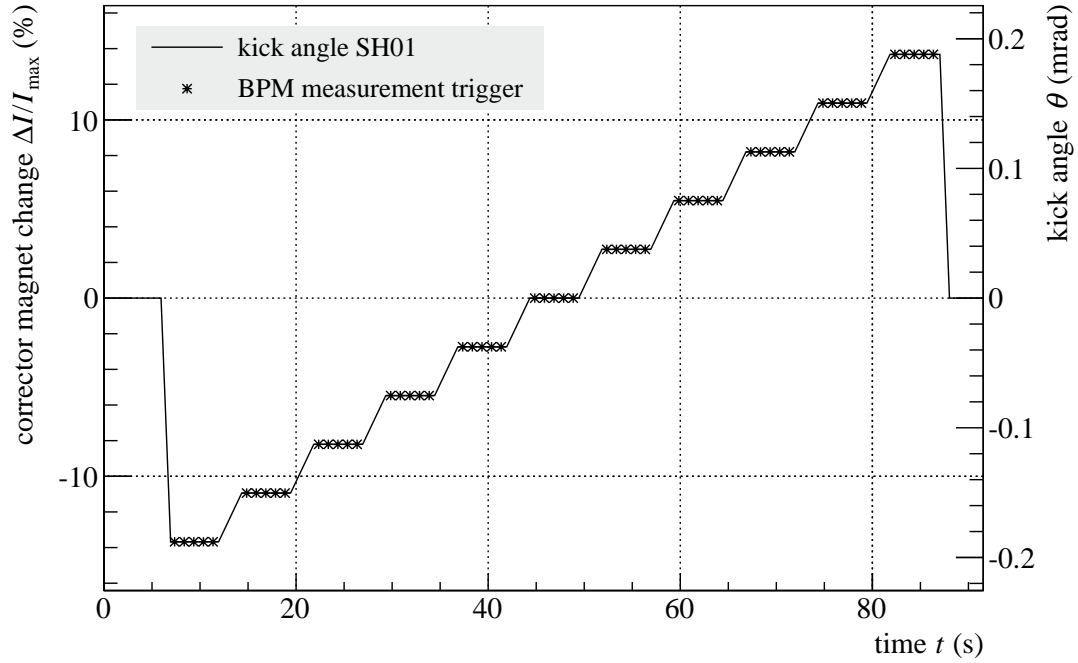


Figure 7.2.: *Current steps of the horizontal corrector magnet SH01 used for the orbit response matrix measurement. The stars indicate the BPM trigger events. For this measurement, the following parameters were used: $N_{\text{steps}} = 11$, $\Delta\theta_{\text{step}} = 0.05$ mrad, and $t_{\text{step}} = 5$ s.*

For each ORM measurement, the number of steps per corrector magnet N_{steps} , the kick angle per step $\Delta\theta_{\text{step}}$, and the duration of the kick t_{step} are adjustable. The corresponding variables and their default settings are listed in Tab. 7.1.

7. Orbit Response Matrix

During the time periods t_{step} , for which all corrector strengths are constant, the measurements of the beam position are performed.

Table 7.1.: *The variables, listed, can be modified to adjust the ORM measurement. The listed values are the ones, used for the measurement of the presented data.*

system	description	variable	value
corrector magnets	number steps per corrector	N_{steps}	11
	kick angle per step	$\Delta\theta_{\text{step}}$ (mrad)	0.05
	duration of kick	t_{step} (ms)	5000
BPM trigger	trigger repetition time	t_{trig} (ms)	1000
	trigger time gap	$t_{\text{trig,gap}}$ (ms)	500

7.1.2. Beam Position Monitor Readout

Each of the BPM readout electronics is configured to measure the beam position with each incoming trigger signal. The measured position is transmitted via Ethernet to the automated ORM measurement software. Since the transmitted data have no time information, a timestamp is attached to the data at the arrival at the measurement software. This timestamp is the time in ms after the cycle started. The algorithm to calculate the timestamp is explained in the following section. This timestamp is used to correlate the beam position measurement to the setting of the corrector magnets, which is stored internally in the software. The typical response of the measured change of the closed orbit is shown in Fig. 7.3 for the two horizontal BPMs bpmx18 and bpmx19. In the presented examples, the step-wise change of the closed orbit induced by the change of the corrector magnet SH01 is clearly present.

The timing of the BPM trigger is adjustable with two parameters. The first parameter is the trigger repetition time t_{trig} . This time defines the temporal distance between consecutive trigger events. The second parameter is the time gap $t_{\text{trig,gap}}$. This variable defines the gap between the end of one corrector change and the beginning of the BPM measurements, as well as the time distance between the last BPM measurement and the next corrector change. The number of trigger events N_{trig} per corrector step is calculated by:

$$N_{\text{trig}} = \frac{t_{\text{step}} - 2t_{\text{trig,gap}}}{t_{\text{trig}}}. \quad (7.5)$$

For the calculation of the ORM, including an error estimation, a noise measurement for each BPM is needed. This measurement is done within the second

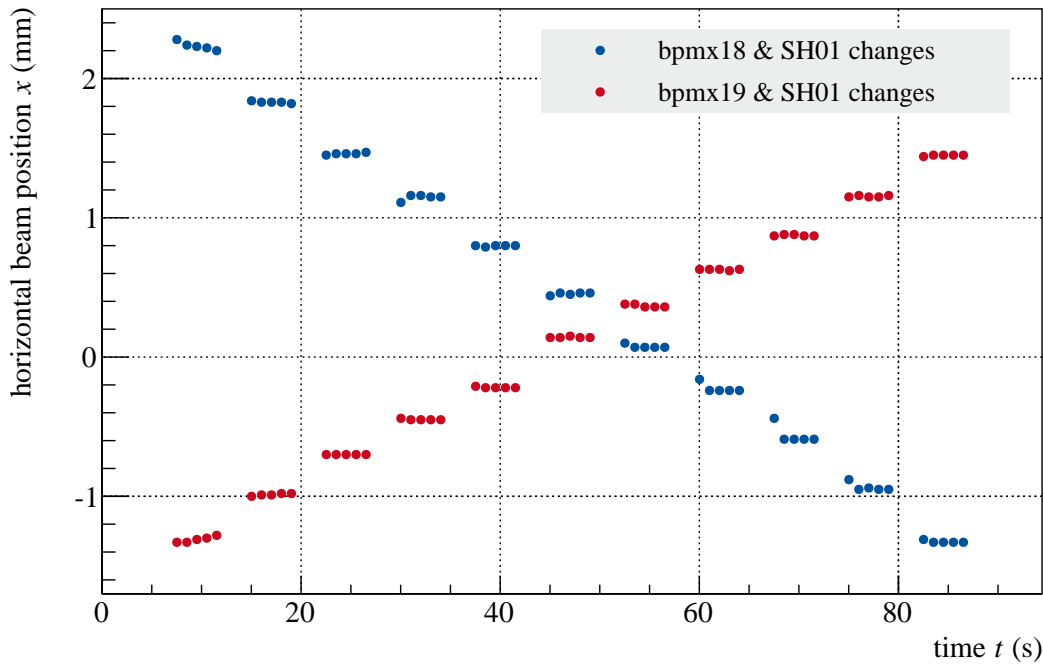


Figure 7.3.: *Response of the beam position, measured with bpmx18 and bpmx19, for the change of the corrector magnet SH01, shown in Fig. 7.2.*

cycle of the complete measurement. In this cycle, no corrector change is applied and the BPMs are triggered with the same trigger signals as during the ORM measurement. A detailed discussion of the noise measurement and other systematic effects, influencing the ORM measurement is presented in 7.2.2.

7.1.3. Timing

The COSY timing system is a central trigger event distributor, which triggers all needed hardware within an accuracy of 100 ns [88]. All BPMs and all corrector magnets are triggered by this system. In addition, the timing sender sends, on request, information about the COSY status every 2 s over Ethernet. The package sent includes COSY status information like the time in the cycle or the cycle length. The developed software receives this information and uses it for time stamping the incoming BPM measurements: On receiving the information package, the software starts running a local clock, based on the machine time, to interpolate between successive time packages. The incoming BPM events are then time-stamped with this interpolated time. The distance between the timestamp and the trigger event, which is set in the central timing system, is called readout delay $\Delta t_{\text{readout}}$. The distribution of the readout delay times of all

7. Orbit Response Matrix

BPM measurements during the ORM measurement is shown in Fig. 7.4. The averaged readout delay amounts

$$\overline{\Delta t_{\text{readout}}} = 170 \text{ ms.} \quad (7.6)$$

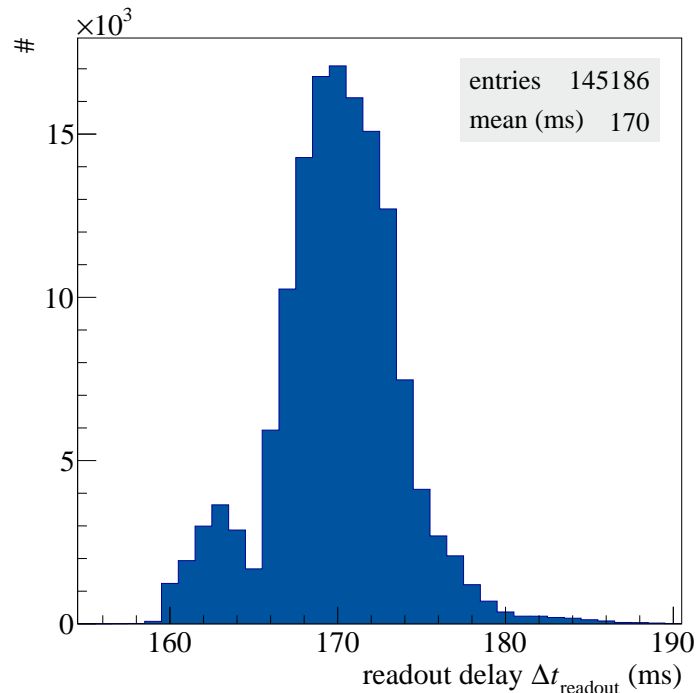


Figure 7.4.: *The delay between the BPM trigger and the arrival of the BPM's readout is calculated for all BPM events. Their average delay amounts 170 ms, which is smaller than the difference between a corrector magnet change and a BPM trigger event ($t_{\text{trig,gap}} = 500 \text{ ms}$)*

The trigger gap between a corrector magnet change and a BPM trigger should be adjusted to a value which is larger than this readout delay. If this condition is fulfilled, the interpolated timestamp is accurate enough to exclude a wrong correlation between the corrector magnet strength and the BPM measurement. In the presented measurements, this condition is fulfilled:

$$t_{\text{trig,gap}} = 500 \text{ ms} \geq 170 \text{ ms} = \overline{\Delta t_{\text{readout}}}. \quad (7.7)$$

All the measured beam positions, including their timestamps, the active corrector magnet change and settings of the BPMs itself are stored in a ROOT file for a later analysis and calculation of the ORM.

7.2. Orbit Response Matrix Calculation

The ROOT file, which is created and filled with measurements by the software, described in the previous section, is used to calculate the ORM. Each entry of the ORM $M_{i,j}$ represents the response of the beam position, measured with the BPM i , to a change of the corrector magnet j . For the calculation of the ORM element, including its error, the following information are needed. First of all, the noise of the beam position measurement is estimated. In a second step systematic effects, introduced by global closed orbit changes over time are calculated and considered in the ORM calculation. In addition to systematic changes of the accelerator, systematic effects, introduced by the readout electronics are considered in the calculation. All the mentioned effects are discussed in the following.

7.2.1. Noise Measurement

The noise of the beam position measurement, including the readout chain and the beam stability, is estimated by analyzing the noise measurement cycle. This noise measurement is performed by using the same accelerator settings as during the ORM measurement, without changing any corrector magnets. The beam positions measured by all BPMs are plotted against the cycle time.

In the vertical plane, the beam is stable over time and the standard deviation of all measurements is calculated for each BPM. This standard deviation is later used for the error estimation during the ORM calculation.

In the horizontal plane the beam moves during the first 10 seconds during the activation operation of the guiding dipoles. This movement can be described by an exponential function. The time constant τ of the exponential function is the same for all horizontal BPMs, the amplitude A is different for all BPMs. To describe this behavior a global fit to all horizontal data points is performed. For each BPM the function

$$f_{\text{noise},i}(t) = \bar{x}_i - A_i \cdot e^{-\frac{t}{\tau}} \quad (7.8)$$

is fitted. The parameters A_i and \bar{x}_i are calculated for each BPM. The time constant τ is one common parameter for all fits. The resulting noise measurement for bpmx25, including the global fit, is shown in Fig. 7.5. For the horizontal BPMs, the standard deviation σ_i for BPM i is calculated by:

$$\sigma_i = \sqrt{\frac{1}{N-1} \sum_{l=0}^N (x_{i,l} - f_{\text{noise},i}(t_l))^2}. \quad (7.9)$$

7. Orbit Response Matrix

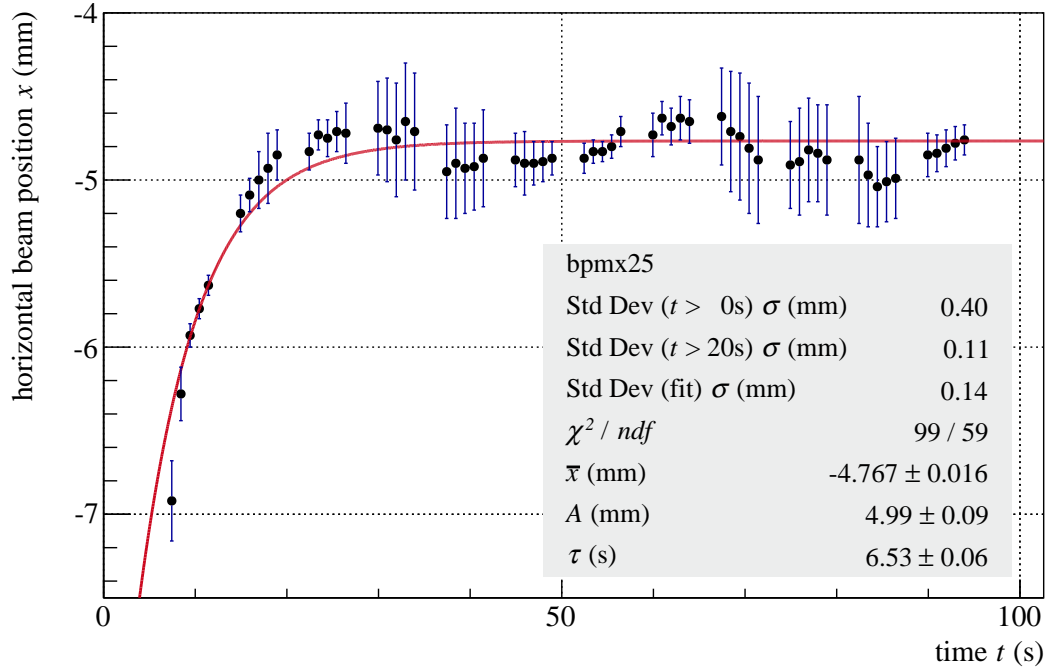


Figure 7.5.: Noise measurement for bpmx25. The data points are the measured beam position during one cycle without any corrector magnet changes. The red curve is a global fit, parameterizing the activation operation of the guiding dipoles.

As a comparison, the standard deviation using all data points and no fit, and the standard deviation using only the data points after 20 seconds are calculated as well. The results from all three methods are given in Fig. 7.5. The standard deviations, using the fit and using the data points after 20 seconds result in the same resolution for one single beam position measurement: $\sigma = 0.1$ mm. This value is later used for the noise estimation for the ORM entry calculation. The shown bpmx25 is the BPM with the highest noise. The distribution of the standard deviations, calculated for all BPMs are presented in Fig. 7.6. As a comparison, the digital resolution $\sigma_{\text{dig}} = 10 \mu\text{m}$ of the BPM system is marked with a green line.

The mean values of the two distributions are:

$$\bar{\sigma}_x = 21 \mu\text{m} \quad (7.10)$$

$$\bar{\sigma}_y = 11 \mu\text{m}. \quad (7.11)$$

These values reflect a combination of the stability of COSY, after subtracting the mentioned exponential horizontal beam movement, as well as the resolution of the BPM system.

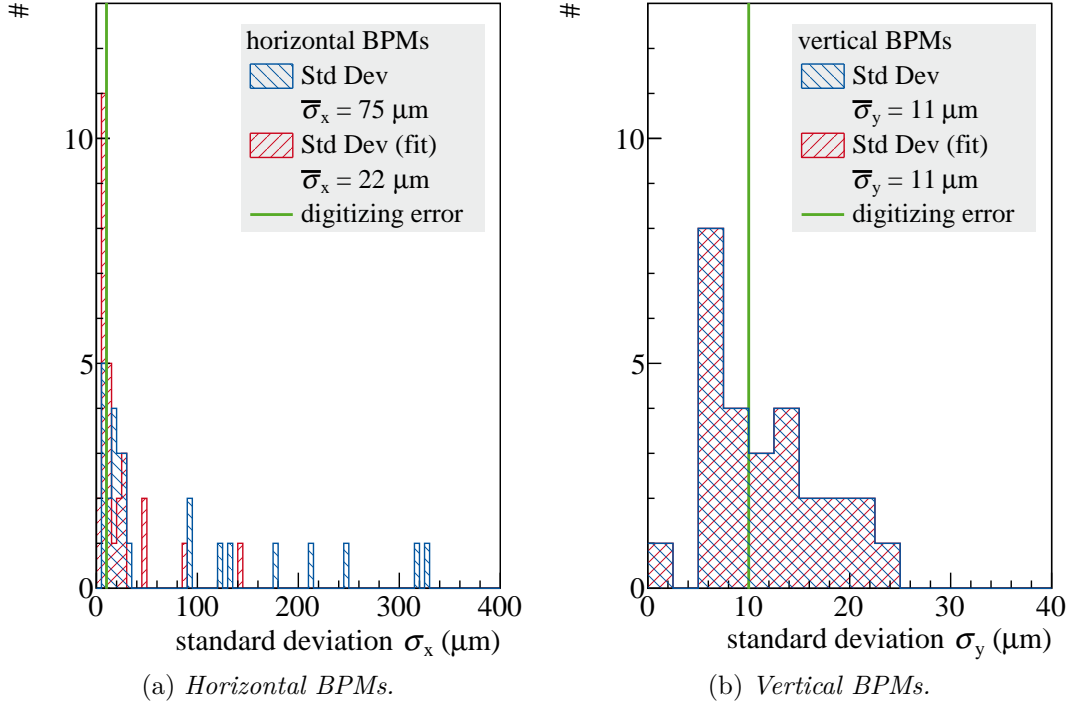


Figure 7.6.: *Distribution of the standard deviations for the horizontal and vertical BPMs. The standard deviation is calculated for all measured beam positions without considering the horizontal beam movement (blue) and with considering the performed exponential fit to the horizontal measurements (red). As comparison, the digital resolution of the BPM electronics is indicated by a vertical green line at $\sigma_{x,y} = 10 \mu\text{m}$*

One possible source of the horizontal beam movement is the inductance of the main dipoles. The inductance and the resistance of one dipole are:

$$R_{\text{dipole}} = 3.06 \text{ m}\Omega, L_{\text{dipole}} = 15.6 \text{ mH}. \quad (7.12)$$

The time constant during the ramp of the magnet is to first order: $\tau_{\text{dipole}} = \frac{L_{\text{dipole}}}{R_{\text{dipole}}} = 5.1 \text{ s}$. This simple approximation is in good agreement with the time constant of $(6.53 \pm 0.06) \text{ s}$ calculated with the global fit. Additional effects like Eddy currents in the iron and in the beam pipe increases the time constant τ_{dipole} towards the measured time constant. The amplitudes A_i for each BPM of the global fit are presented in Fig. 7.7. They are plotted against the longitudinal position of the BPM in COSY. The obtained curve is proportional to the dispersion function of the COSY optics used during the measurement. This distribution underlines the assumption, that the horizontal beam movement is

7. Orbit Response Matrix

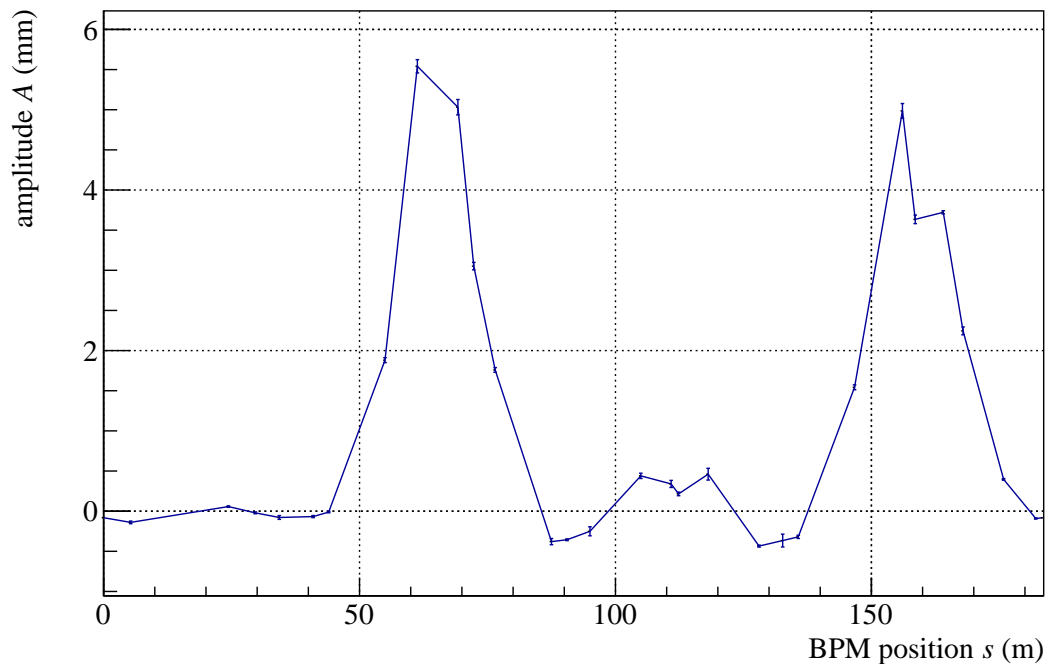


Figure 7.7.: *The fitted amplitudes A_i for all horizontal BPMs plotted against the position s of the BPM.*

caused by the guiding dipoles of COSY. This exponential curvature of the beam position is considered in the calculation of the ORM entries.

As additional systematic effects, the properties of the electronics (cp. chapter 6) have to be considered. As one example, the noise measurement of bpmx27, presented in Fig. 7.8, is evaluated and discussed. The measured beam positions over time show the already discussed exponential behavior. On top of this effect, the properties of the readout electronics influence the measured beam position. The data points show a clear step from -0.2 mm to 0.2 mm at about 50 s. This effect is typical for the measurements around the 0 position and can be described by (6.21). The combination of (7.8) and (6.21) can be used to fit the BPM model as well as the true beam position over time:

$$f_{\text{noise}}(t) = x_{\text{meas}}(x_{\text{true}}(t)) \quad (7.13)$$

$$x_{\text{true}}(t) = \bar{x}_{\text{bpmx27}} - A_{\text{bpmx27}} \cdot e^{-t/\tau}. \quad (7.14)$$

The parameters A_{bpmx27} and \bar{x}_{bpmx27} consider the beam properties, whereas the function x_{meas} depends on the parameters x_{lin} and x_{offset} , which describe the electronics' properties. The resulting function is shown in orange in Fig. 7.8. The fitted beam position, without the effect of the electronics is shown as a red curve. The noise of bpmx27 is estimated by calculating the standard deviation

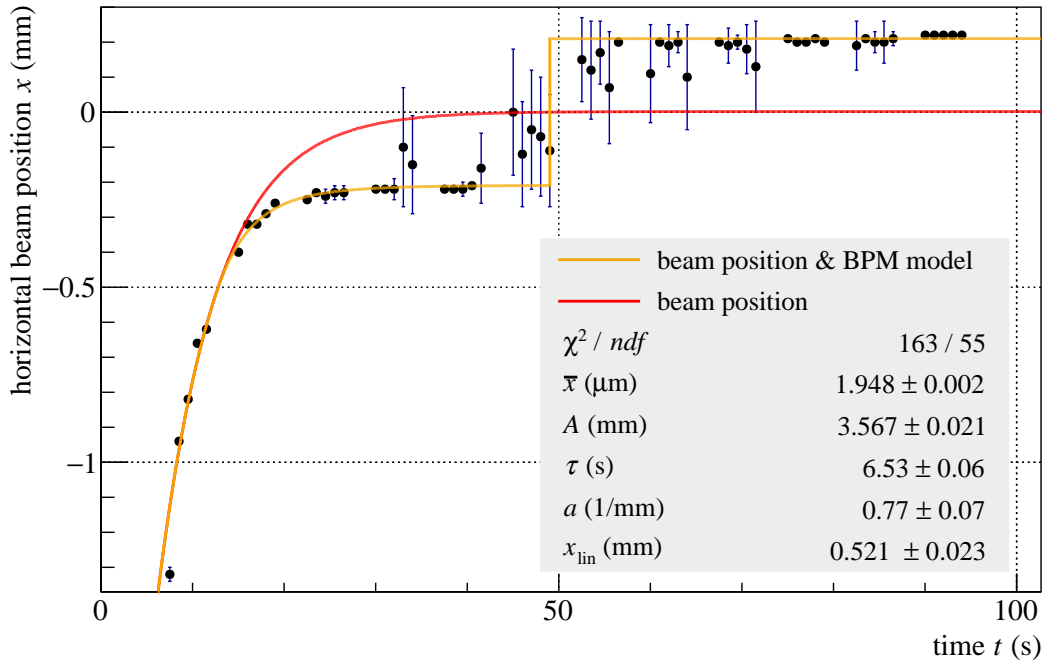


Figure 7.8.: Noise measurement of *bpmx27*. The beam moves towards the electrical center of the BPM. Since the readout electronics is not capable to measure exactly zero, the data points show the typical step and the offset. A fit including the BPM readout electronics model and the global time constant τ is performed to describe the measured beam positions (orange). The resulting estimate for the true beam position is illustrated as a red curve.

of the measured data points with respect to the fitted function f_{noise} .

All in all, the noise measurements show, that systematic effects like beam movement or electronic properties have to be considered in the error estimate. By describing the mentioned systematics, the noise of the BPM system and the stability of the beam is in the order of $21 \mu\text{m}$ for the horizontal BPMs and $11 \mu\text{m}$ for the vertical ones, which is compatible to the digitizing error of the readout electronics. The estimated noise of each BPM is considered in the following calculations.

7.2.2. Matrix Entry Calculation

The ORM entries are calculated by analyzing the measured beam positions with respect to the corrector magnet setting. The measured beam positions are first corrected by the noise measurement to get rid of the exponential beam

7. Orbit Response Matrix

movement. This correction is done by subtracting the fitted function (7.8) $f_{\text{noise},i}(t)$ from the beam position $x_{i,j}$ measured at time t_j with BPM i :

$$\Delta x_{i,j} = x_{i,j} - f_{\text{noise},i}(t_j). \quad (7.15)$$

The corrected beam positions are used to calculate the change of the orbit, induced by a change of the corrector magnet. For each setting of the magnet, N_{trig} measurements of the beam position are done. These measurements are averaged:

$$\bar{x}_{\text{step},i} = \frac{1}{N_{\text{trig}}} \sum_{j=1}^{N_{\text{trig}}} \Delta x_{i,j}. \quad (7.16)$$

The variance $\sigma_{x,\text{step},i}^2$ is calculated for each step and each BPM:

$$\sigma_{x,\text{step},i}^2 = \frac{1}{N_{\text{trig}} - 1} \sum_{j=1}^{N_{\text{trig}}} (\Delta x_{i,j} - \bar{x}_{\text{step},i})^2. \quad (7.17)$$

The error of the mean value \bar{x}_{step} is estimated by using the maximum of the variance obtained by analyzing the noise measurement (7.9) and the variance calculated during the averaging:

$$\sigma_{\bar{x}_{\text{step},i}} = \frac{1}{\sqrt{N_{\text{trig}}}} \max(\sigma_i, \sigma_{x,\text{step},i}). \quad (7.18)$$

The described procedure results in N_{steps} averaged measurements for each combination of BPM i and corrector magnet j . For each combination, the calculated average is plotted against the corrector magnet change. The error on the corrector magnet change is estimated by using (7.4). On the resulting N_{steps} data points, a straight line is fitted:

$$x_i = x_{0,i} + M_{i,j} \cdot \theta_j. \quad (7.19)$$

The slope of this fit is the matrix entry $M_{i,j}$. For the already discussed combination corrector magnet SH01 and BPM bpmx18, the resulting measurements are presented in Fig. 7.9.

The measured ORM entry is:

$$M_{\text{bpmx18,SH01}} = (-9.22 \pm 0.04) \frac{\text{mm}}{\text{mrad}}. \quad (7.20)$$

For the measurements, where the beam is already near the electronic center, or where the beam moves during the change of the corrector magnets through the electronic center of the BPM, the measurement is systematically dominated by

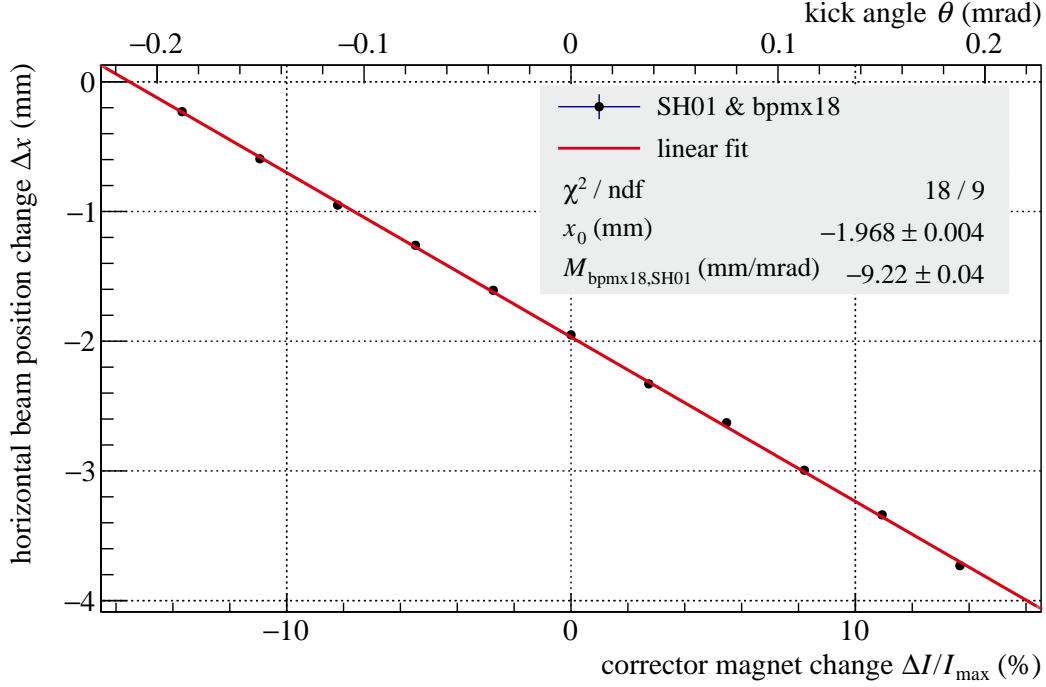


Figure 7.9.: The horizontal beam positions measured with bpmx18 depending on the strength change of corrector magnet SH01 are marked with blue points. The red line is the fitted function (7.19). The fit parameter $M_{\text{bpmx18,SH01}}$ is the corresponding, measured ORM entry.

the behavior of the readout electronics. Nevertheless, the ORM entry can be calculated by including equation (6.21) in the fit. For these cases, the measured beam position can be described by:

$$x(\theta) = x_{\text{meas}}(M_{i,j} \cdot (\theta - \theta_0)) + x_0, \quad (7.21)$$

where x_{meas} is the function (6.21) describing the readout electronics. The parameters, which are adjusted to describe the data points are a , x_{lin} , x_0 , θ_0 and $M_{i,j}$. The first two parameters characterize the electronics, whereas the third parameter reflects the cycle-to-cycle variations. The parameter θ_0 is the corrector magnet strength, which moves the beam to the center of the BPM and the last parameter is the ORM entry. One example of such set of data points is shown in Fig. 7.10 for the combination of BPM bpmx10 and magnet SH01. The fit, including the BPM model is shown as a red line. The orange line is the simple linear BPM response without the BPM model parameters. By using only the simple linear BPM response, the resulting ORM entry is overestimated by 8%.

All presented examples are measurements with horizontal corrector magnets

7. Orbit Response Matrix

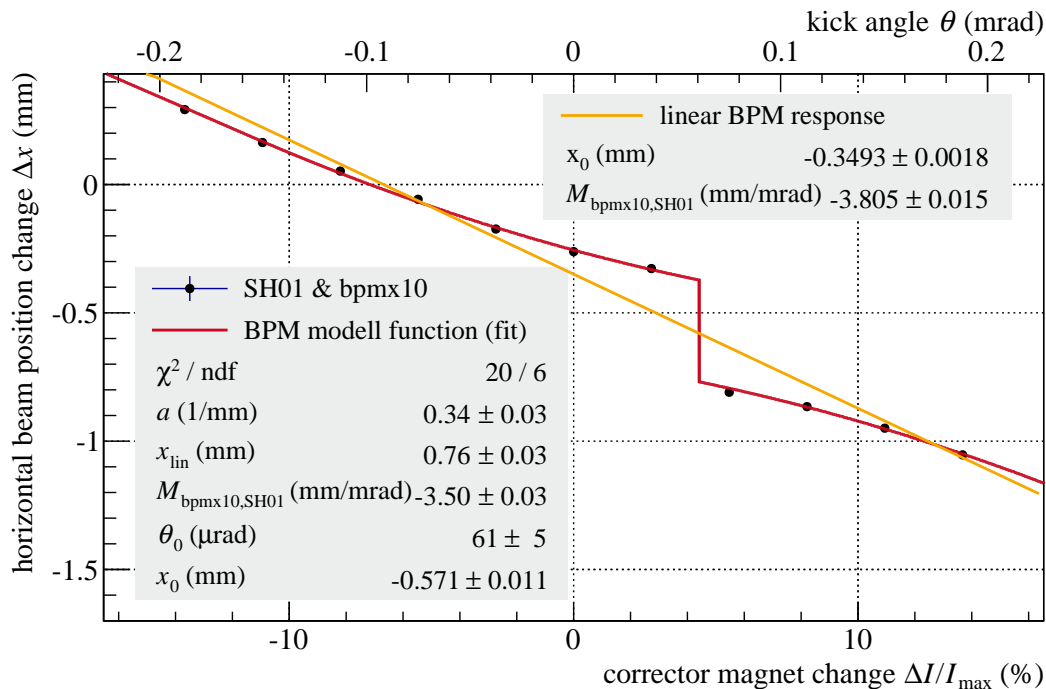


Figure 7.10.: Measurement of the ORM entry *SH01* & *bpmx10*. The beam is already near the electrical center of *bpmx10*. The effect of the non linearity of the bpm readout electronics dominates the position measurement. Nevertheless, the matrix entry $M_{bpmx10, SH01}$ can be measured by fitting the BPM electronics model.

and horizontal BPMs. In the vertical plane, only the effect of the BPM readout electronics model has to be taken into account and is included in the presented measurement result. The effect of the exponential drift of the beam position at the beginning of the measurement is nonexistent, which indicates, that this effect is caused by the main dipoles which influence only the horizontal beam position. The resulting ORM, including all discussed effects is shown in Fig. 7.11. The matrix has a block diagonal structure, since the vertical corrector magnets influence mainly the vertical BPMs and the horizontal BPMs respond to the horizontal corrector magnets. The upper left block (horizontal BPMs and horizontal magnets) has entries between -0.75 mm/mrad and 1.31 mm/mrad. Their vertical-vertical response is in the range -0.79 mm/mrad to 0.65 mm/mrad. Within the two mentioned blocks, the entries have a typical structure of diagonal lines. This structure is caused by the cosine term in the equation for the ORM matrix entries (3.38). The off-diagonal block entries are in the range of -0.03 mm/mrad to 0.02 mm/mrad, which is approximately a factor 40 smaller. In addition, the vertical-horizontal and horizontal-vertical ORM entries show no inner structure of the matrix. In conclusion, the ORM

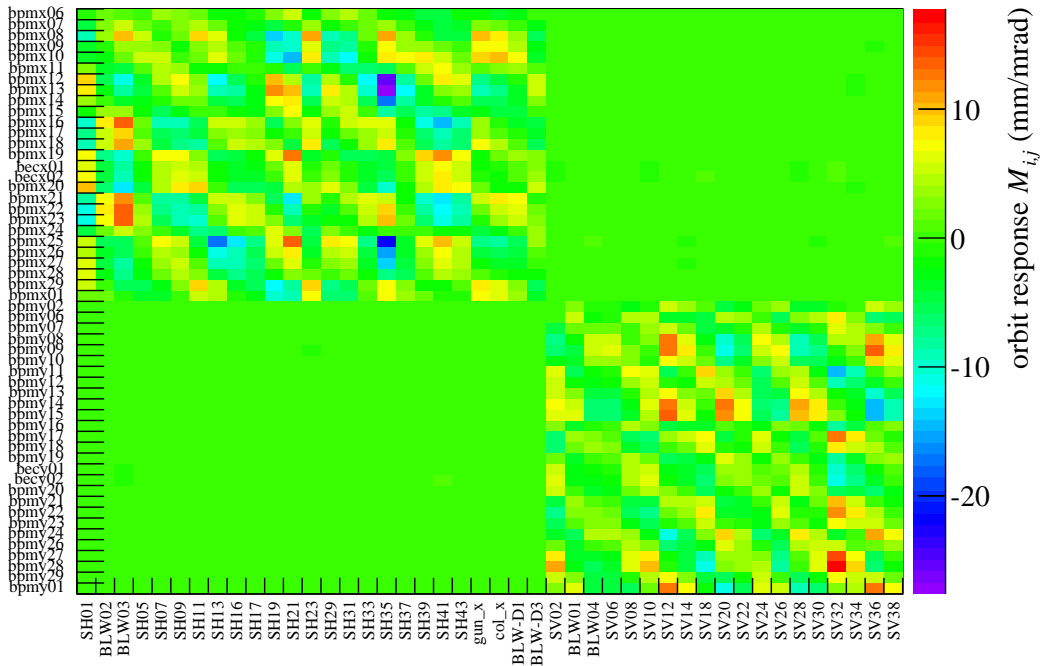


Figure 7.11.: *The complete measured ORM. The corrector magnets are listed on the x axis, the y axis lists the BPMs. The color code is the response of each BPM to an applied kick angle of the corresponding corrector magnet. The block matrix structure, as described in the text, is clearly visible: The horizontal-horizontal as well as the vertical-vertical entries are by a factor ≈ 40 higher than the horizontal-vertical combinations.*

measurement software functions as desired and the calculation of the ORM is possible with an accuracy of 0.5% for each entry. Two effects, which can influence the ORM measurement have to be considered in the calculation and measurement. The first effect is an exponential horizontal movement of the beam with a time constant $\tau = (6.52 \pm 0.06)$ s. This systematic effect can be controlled by fitting a global exponential function, parameterizing the effect to the data points. As a side product, the distribution of the dispersion of the accelerator can be calculated. Instead of describing the beam movement by an exponential function, the measurement can be started later in the measurement cycle. This starting time has to be chosen in a way, that the exponential beam movement is smaller than the resolution of the BPMs during the ORM entry

7. Orbit Response Matrix

measurement. This starting time t_1 can be calculated by:

$$\begin{aligned} x(t_2) - x(t_1) &< \sigma_x \\ \Leftrightarrow A \cdot (e^{-t_2/\tau} - e^{-t_1/\tau}) &< \sigma_x \\ \Leftrightarrow t_1 &> -\ln\left(e^{-t_2/\tau} + \frac{\sigma_x}{A}\right) \cdot \tau. \end{aligned}$$

Using the maximum Amplitude $A_{\text{bpmx12}} = 5.5 \text{ mm}$, the measured resolution $\bar{\sigma}_x = 20 \mu\text{m}$ and a measurement time of $t_2 - t_1 = 80 \text{ s}$ for one complete set of measurements, leads to a starting time of $t_1 = 20 \text{ s}$.

The second systematic effect is the measurement offset around 0. It can be addressed by measuring more than five different corrector magnet settings for each ORM entry. With these data points a combined fit, including a BPM model and the requested ORM entry is possible.

Besides these two effects, a crucial point is the stability of the beam, without changing any magnet. This effect is estimated by analyzing the noise measurement, which leads to an overall stability of the horizontal measurements of $\bar{\sigma}_x = 22 \mu\text{m}$ respectively $\bar{\sigma}_y = 11 \mu\text{m}$. Both values include the stability of the accelerator, as well as the resolution of the BPMs including the readout chain.

7.3. Orbit Correction

The closed orbit of an accelerator is the measured beam position at all BPMs, written in one vector \vec{y} . The deviation of this closed orbit from the center is one source of systematic effects of the EDM measurement (cf. 2.4). The beam positions can be corrected by using corrector dipole magnets, which kick the beam by kick angles $\vec{\theta}$. The task of the orbit correction is to find a combination of corrector kicks to minimize the orbit deviations.

The orbit correction algorithms are based on the mathematical problem of solving a system of linear equations:

$$\mathbf{M}\vec{\theta} = \vec{y}, \quad \mathbf{M} \in \mathbb{R}^{m \times n}, \quad \vec{\theta} \in \mathbb{R}^n, \quad \vec{y} \in \mathbb{R}^m. \quad (7.22)$$

At COSY the number of BPMs $m = 63$ (32 horizontal, 31 vertical) is higher than the number of corrector magnets $n = 41$. This leads to an over-determined system, which is solved by finding the solution of the linear least square problem:

$$\min_{\vec{\theta}} \left\| \mathbf{M}\vec{\theta} - \vec{y} \right\|_2, \quad \mathbf{M} \in \mathbb{R}^{m \times n}, \quad \vec{\theta} \in \mathbb{R}^n, \quad \vec{y} \in \mathbb{R}^m. \quad (7.23)$$

The vector two norm $\|\vec{y}\|_2 = \sqrt{\sum_{i=0}^N y_i^2}$ is used as a norm for the minimization process.

7.3.1. Correlated Data

Equation (7.23) holds, if the measurement uncertainties of the measured orbit \vec{y} are uncorrelated and equal for all BPMs. For the case of correlated data and/or unequal uncertainties, the equation needs to be modified by the covariance matrix \mathbf{C}_y [89]:

$$\min_{\vec{\theta}} (\mathbf{M}\vec{\theta} - \vec{y})^\top \mathbf{C}_y^{-1} (\mathbf{M}\vec{\theta} - \vec{y}), \quad (7.24)$$

$$\mathbf{M} \in \mathbb{R}^{m \times n}, \quad \vec{\theta} \in \mathbb{R}^n, \quad \vec{y} \in \mathbb{R}^m, \quad \mathbf{C}_y \in \mathbb{R}^{m \times m}.$$

In finding the solution, first a transformation to independent variables is necessary. This transformation, the Cholesky factorization, can always be found since the covariance matrix is positive definite [90]:

$$\mathbf{C}_y = \mathbf{L}\mathbf{C}_{y'}\mathbf{L}^\top. \quad (7.25)$$

The transformation matrix \mathbf{L} is lower triangular and the covariance matrix $\mathbf{C}_{y'}$ is diagonal. The transformation matrix $\mathbf{P} = \mathbf{L}^{-1}$ transforms the measured orbit \vec{y} to the new independent variables \vec{y}' :

$$\vec{y}' = \mathbf{P}\vec{y} \quad (7.26)$$

$$\mathbf{M}' = \mathbf{P}\mathbf{M}. \quad (7.27)$$

The solution of the minimization problem, including $\mathbf{C}_{y'}$, reads [89, p. 113]

$$\hat{\vec{\theta}} = (\mathbf{M}'^\top \mathbf{C}_{y'}^{-1} \mathbf{M}')^{-1} \mathbf{M}'^\top \mathbf{C}_{y'}^{-1} \vec{y}'. \quad (7.28)$$

Since the matrix $\mathbf{C}_{y'}$ is diagonal and has the diagonal elements η_1^2 to η_m^2 , its inverted matrix is simply:

$$\mathbf{C}_{y'}^{-1} = \text{diag}(1/\eta_1^2, 1/\eta_2^2, \dots, 1/\eta_m^2) = \boldsymbol{\eta}^2. \quad (7.29)$$

Scaling the ORM and the orbit with its uncertainties,

$$\mathbf{M}_S = \boldsymbol{\eta}\mathbf{M}' \quad (7.30)$$

$$\vec{y}_S = \boldsymbol{\eta}\vec{y}', \quad (7.31)$$

7. Orbit Response Matrix

leads to a rewritten form of (7.28):

$$\hat{\theta} = - \left(\mathbf{M}_S^\top \mathbf{M}_S \right)^{-1} \mathbf{M}_S^\top \vec{y}_S. \quad (7.32)$$

The matrix inversion $\left(\mathbf{M}_S^\top \mathbf{M}_S \right)^{-1}$ can be solved with different methods. One method, commonly used, is the Singular Value Decomposition SVD.

7.3.2. Singular Value Decomposition

Every matrix $\mathbf{Z} \in \mathbb{R}^{m \times n}$ can be decomposed in its singular values [91, chapter 3]:

$$\mathbf{Z} = \mathbf{U} \mathbf{\Sigma} \mathbf{V}^\top \quad (7.33)$$

where $\mathbf{\Sigma} \in \mathbb{R}^{m \times n}$ is a diagonal matrix, consisting of the singular values σ_i :

$$\mathbf{\Sigma} = \left(\begin{array}{ccc|ccc} \sigma_1 & & & & \vdots & \\ & \ddots & & \dots & 0 & \dots \\ & & \sigma_n & & \vdots & \\ \hline & & & & \vdots & \\ \dots & 0 & \dots & \dots & 0 & \dots \\ & \vdots & & & \vdots & \\ & & & & \vdots & \end{array} \right), \quad \text{with } \sigma_1 \geq \sigma_2 \geq \dots \geq \sigma_n \geq 0. \quad (7.34)$$

The matrices $\mathbf{U} \in \mathbb{R}^{m \times m}$ and $\mathbf{V} \in \mathbb{R}^{n \times n}$ are unitary, therefore the following relations hold:

$$\mathbf{U} \mathbf{U}^\top = \mathbf{V}^\top \mathbf{V} = \mathbf{1}. \quad (7.35)$$

If the inverse of matrix \mathbf{Z} exists, it reads:

$$\mathbf{Z}^{-1} = \mathbf{V} \mathbf{\Sigma}^{-1} \mathbf{U}^\top. \quad (7.36)$$

The SVD of $\mathbf{M}_S = \mathbf{U}_S \mathbf{\Sigma}_S \mathbf{V}_S^\top$ can be used to solve (7.32):

$$\hat{\theta} = - \left(\mathbf{M}_S^\top \mathbf{M}_S \right)^{-1} \mathbf{M}_S^\top \vec{y}_S \quad (7.37)$$

$$= - \left(\left(\mathbf{U}_S \mathbf{\Sigma}_S \mathbf{V}_S^\top \right)^\top \left(\mathbf{U}_S \mathbf{\Sigma}_S \mathbf{V}_S^\top \right) \right)^{-1} \left(\mathbf{U}_S \mathbf{\Sigma}_S \mathbf{V}_S^\top \right)^\top \vec{y}_S \quad (7.38)$$

$$= - \left(\mathbf{V}_S \mathbf{\Sigma}_S \mathbf{U}_S^\top \mathbf{U}_S \mathbf{\Sigma}_S \mathbf{V}_S^\top \right)^{-1} \left(\mathbf{V}_S \mathbf{\Sigma}_S \mathbf{U}_S^\top \right) \vec{y}_S \quad (7.39)$$

$$= - \left(\mathbf{V}_S \mathbf{\Sigma}_S^{-2} \mathbf{V}_S^\top \right) \left(\mathbf{V}_S \mathbf{\Sigma}_S \mathbf{U}_S^\top \right) \vec{y}_S \quad (7.40)$$

$$= - \mathbf{V}_S \mathbf{\Sigma}_S^{-1} \mathbf{U}_S^\top \vec{y}_S. \quad (7.41)$$

In the step from the second to the third line, the unitary of Σ_S was used. The resulting kick angles $\hat{\theta}$ are the solution of the minimization problem (7.24), including the covariance matrix C_y .

The quality of the orbit correction is proportional to the RMS of the residual orbit y_{res} which is defined as:

$$\vec{y}_{\text{res}} = \mathbf{M}\hat{\theta} + \vec{y}. \quad (7.42)$$

Its RMS, with respect to the measured covariance matrix $C_{y,\text{res}}$ is estimated by:

$$\text{RMS}_{y_{\text{res}}} = \sqrt{\frac{\vec{y}_{\text{res}}^T C_{y,\text{res}} \vec{y}_{\text{res}}}{m}}, \quad (7.43)$$

where m is the number of BPMs.

Truncated SVD Small errors in the measured orbit \vec{y} or in the measured ORM \mathbf{M} can lead to large errors in the calculated kick angles. Assuming the exact solution and the perturbed solution follow the relations:

$$\mathbf{M}_S^{\text{exact}} \vec{\theta}^{\text{exact}} = \vec{y}_S^{\text{exact}}, \quad \mathbf{M}_S \vec{\theta} = (\mathbf{M}_S^{\text{exact}} + \sigma_M) \vec{\theta}, \quad \vec{y}_S = \vec{y}_S^{\text{exact}} + \vec{\eta}, \quad (7.44)$$

an upper bound of the kick angle errors is given by [91, p. 54], [92, pp. 80-82]:

$$\frac{\|\vec{\sigma}_\theta\|_2}{\|\vec{\theta}^{\text{exact}}\|_2} \leq \kappa(\mathbf{M}) \left(\frac{\|\vec{\eta}\|_2}{\|\vec{y}^{\text{exact}}\|_2} + \frac{\|\sigma_M\|_2}{\|\mathbf{M}\|_2} \right), \quad (7.45)$$

where $\kappa(\mathbf{M})$ is the condition number of the matrix \mathbf{M} . This condition number is defined as:

$$\kappa(\mathbf{M}) = \|\mathbf{M}\| \|\mathbf{M}^{-1}\|. \quad (7.46)$$

For the 2-norm, the condition number is simply given by the fraction of the largest σ_1 to the smallest σ_n singular value [91, p. 29]:

$$\kappa(\mathbf{M}) = \frac{\sigma_1}{\sigma_n} \geq 1. \quad (7.47)$$

For a big difference between the largest and the smallest singular value, the uncertainty of the matrix and the uncertainty of the measured orbit gets amplified and leads to a large uncertainty of the solution $\hat{\theta}$. This amplification effect can be regularized by using the Truncated Singular Value Decomposition TSVD approach, which modifies the inverted matrix Σ_S^{-1} . The modification of the matrix is done, by taking only the k most significant singular values into

7. Orbit Response Matrix

account. The resulting inverse singular value matrix reads:

$$\Sigma_{\mathbf{S},k,i}^{-1} = \begin{cases} \frac{1}{\sigma_i} & i \leq k \\ 0 & i > k \end{cases}, \quad (7.48)$$

where k is the number of used singular values. The parameter k is the regularization parameter, which lies between 1 and n . The solution $\hat{\theta}_k$ depends on the cut value k and reads:

$$\hat{\theta}_k = -\mathbf{V}_S \Sigma_{\mathbf{S},k}^{-1} \mathbf{U}_S^\top \vec{y}_S. \quad (7.49)$$

The corresponding residual orbit results in:

$$\vec{y}_{\text{res},k} = \mathbf{M} \hat{\theta}_k + \vec{y} = -\mathbf{M} \mathbf{V}_S \Sigma_{\mathbf{S},k}^{-1} \mathbf{U}_S^\top \vec{y}_S + \vec{y}. \quad (7.50)$$

In addition, the condition number gets modified and results in [91, p. 65]:

$$\kappa_k(M) = \sigma_1 / \sigma_k. \quad (7.51)$$

Since the singular values are ordered in decreasing sequence, the condition gets larger for increasing k values. For small values of k , the uncertainties of the ORM and the orbit are amplified with a small factor, but the solution $\hat{\theta}_k$ is far away from the exact solution. For large values of k , the solution $\hat{\theta}_k$ reaches the exact solution, but the uncertainties are amplified by a large factor. Both effects can be calculated and the optimal regularization parameter k is a tradeoff of both effects. Since the quality of the correction is measured by the RMS of the residual orbit, the influence of the cut value k on the residual orbit is studied as well as the uncertainty of the residual orbit. On one hand, the error induced by cutting on the singular values, called bias, is given by:

$$\Delta \vec{y}_{\text{res},\text{bias}} = -\mathbf{M} \mathbf{V}_S \left(\Sigma_{\mathbf{S}}^{-1} - \Sigma_{\mathbf{S},k}^{-1} \right) \mathbf{U}_S^\top \vec{y}_S + \vec{y}. \quad (7.52)$$

The RMS of this bias allows in combination with the statistical uncertainty an estimation of the optimal parameter k . The function, describing the RMS is:

$$f_{\text{bias}}(k) = \sqrt{\frac{\|\vec{y}_{\text{res},\text{bias}}\|_2}{m}}. \quad (7.53)$$

On the other hand, the uncertainty of the residual orbit, $\vec{\sigma}_{y,\text{res}}$ has to be calculated. For this, the input uncertainties need to be propagated through the TSVD process. At the end, a balance between both effects, the bias error and the perturbation error, needs to be found, compare [91, ch. 5].

Error propagation through TSVD The covariance matrix of the residual orbit $\mathbf{C}_{y,\text{res}}$ is a function of the two input covariance matrices \mathbf{C}_M and \mathbf{C}_y :

$$\mathbf{C}_{y,\text{res}} = \mathbf{f}_y(\mathbf{C}_y) + \mathbf{f}_M(\mathbf{C}_M). \quad (7.54)$$

The function \mathbf{f}_y can be calculated analytically. The functional dependence on the matrix \mathbf{C}_M can not be solved in a closed form for only pseudo invertible matrices.

First, the analytic solution \mathbf{f}_y is presented. For the corresponding error propagation, the Jacobian needs to be determined. It is given by:

$$\frac{\partial \vec{y}_{\text{res},k}}{\partial \vec{y}} = -\mathbf{M}\mathbf{V}_S\Sigma_{S,k}^{-1}\mathbf{U}_S^\top\boldsymbol{\eta}\mathbf{P} + \mathbf{1}. \quad (7.55)$$

For the resulting function $\mathbf{f}_y(\mathbf{C}_y)$, it follows:

$$\mathbf{f}_y(\mathbf{C}_y) = \frac{\partial \vec{y}_{\text{res}}}{\partial \vec{y}} \mathbf{C}_y \left(\frac{\partial \vec{y}_{\text{res}}}{\partial \vec{y}} \right)^\top. \quad (7.56)$$

The second term in (7.54) has no analytic solution. For invertible matrices, a closed solution for the uncertainties of $\vec{\theta}$ is given in [93]. But for only pseudo-invertible matrices, different approaches are commonly used. Most of these methods give an error bound, which describes the worst case, but not the 68% significance level. A short overview of these methods, used in error analysis of solar particle spectra, is given in [94]. For the purpose of orbit correction, the method of choice is a numerical Monte Carlo MC simulation of the inverse problem and its solution (7.50).

The MC simulation targets a measure of the uncertainty $\mathbf{f}_M(\mathbf{C}_M)$, arising from the uncertainty of the matrix \mathbf{M} . For the simulation, the measured matrix is used as starting point. The errors on the matrix elements, estimated from the measurement uncertainties, are used in the simulation as well. In the simulation itself, the solution vector $\hat{\vec{\theta}}_k$ as well as the residual orbit $\vec{y}_{\text{res},k}$ are calculated N_{sample} times. For each calculation, the entries of the matrix are smeared by the Gaussian function with mean zero and a width, corresponding to the measured uncertainty. The resulting solution vectors $\hat{\vec{\theta}}_k$ and $\vec{y}_{\text{res},k}$ are stored. Their covariance is used as an estimator for $\mathbf{f}_M(\mathbf{C}_M)$. The procedure is repeated for every value of k .

Combining the analytic solution (7.56) and the MC estimation, described, results in the covariance matrix $\mathbf{C}_{y,\text{res}}$ with neglecting a possible correlation between the measured orbit and the measured matrix \mathbf{M} . The error vector $\vec{\sigma}_{y,\text{res},k}$

7. Orbit Response Matrix

is calculated using the information of the covariance matrix $\mathbf{C}_{y,\text{res},k}$:

$$(\vec{\sigma}_{y,\text{res},k})_i = \sqrt{(\mathbf{C}_{y,\text{res},k})_{ii}}. \quad (7.57)$$

For later use, the RMS of the uncertainty of $\vec{\sigma}_{y,\text{res},k}$ is calculated:

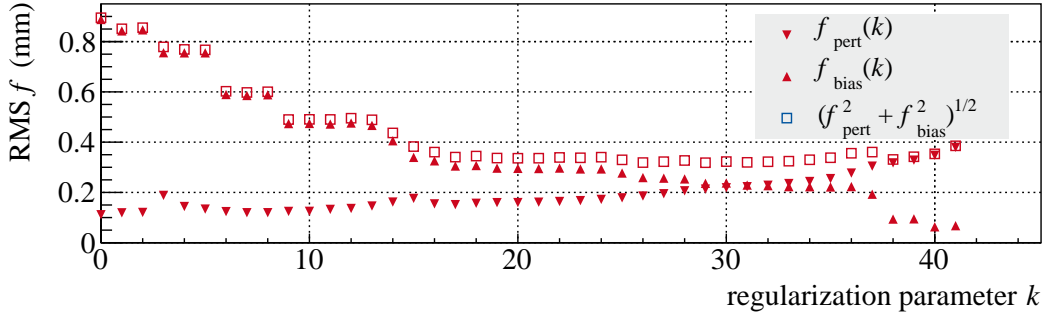
$$f_{\text{pert}}(k) = \sqrt{\frac{\|\vec{\sigma}_{y,\text{res},k}\|_2}{m}}. \quad (7.58)$$

Optimal Regularization Parameter With the developed results, (7.53) and (7.58), the optimal regularization parameter k can be estimated by comparing both effects, the bias and the perturbation [91, ch. 5]. The bias error is going down with increasing cut value, whereas the perturbation amplification increases with increasing regularization parameter k . The regularization parameter on which the two effects are equal is the one of choice. In addition, the quadratic sum of both can be calculated and plotted against the regularization parameter k . The minimum defines the best value for k .

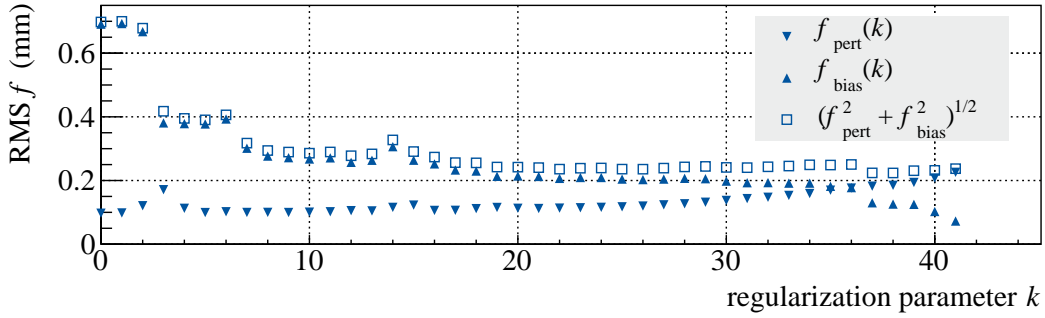
Figure 7.12 shows the curves, calculated during an orbit correction at COSY, which is described in the following section in more details. A clear minimum of the function $\sqrt{f_{\text{bias}}^2 + f_{\text{pert}}^2}$ is not existent. Starting at $k = 17$, the curve becomes flat. Therefore, a regularization parameter around 17 can be chosen.

7.3.3. Example of an Orbit Correction using TSVD

The method of orbit correction, using the TSVD of the ORM, is implemented for COSY and discussed in detail in the following. The presented data were measured in November 2015 with protons at injection energy. First of all, the ORM was measured and calculated. In a second step, the uncorrected orbit and its errors were measured. These uncorrected orbits in horizontal and vertical direction are shown in Fig. 7.13 and Fig. 7.14 with blue markers. The RMS of these orbits are: (4.78 ± 0.07) mm and (3.70 ± 0.07) mm. For the correction, the BPM measurements are treated as uncorrelated with an equal error for each measurement. This simplifies the derived equation (7.32), since the matrices $\boldsymbol{\eta}$ and \mathbf{P} become the unity matrix $\mathbf{1}$. Depending on the regularization parameter, the kick strengths and the residual orbits are calculated. In addition, the perturbation function as well as the bias function are estimated. These two resulting functions are shown in Fig. 7.12a for the horizontal plane and in Fig. 7.12b for the vertical direction. As discussed in the previous chapter a clear minimum of the quadratic sum of both functions does not exist. The regularization parameter can be set to $k = 17$.



(a) Horizontal.



(b) Vertical.

Figure 7.12.: The distribution of the perturbation, the bias and the quadratic sum of both is plotted against the selected regularization parameter for the vertical (a) and the horizontal (b) case. The optimal parameter k is the position of the minimum of the quadratic sum. Since this minimum is flat, a clear choice is not possible.

For comparison of the calculated results to a measurement at COSY, the regularization parameters $k = 3$ and $k = 17$ are used and the strengths $\hat{\theta}_k$ are calculated and applied to the corrector magnets. The calculated orbit $\vec{y}_{\text{res},k}$ is shown in Fig. 7.13 and Fig. 7.14 for the horizontal resp. vertical orbit. The calculated beam positions are marked with open squares. The uncertainty is calculated by using the developed error propagation through the TSVD inversion, cp. (7.57). The orbit, measured after applying the correction strengths, is shown on top of the predicted orbit and marked with filled dots including the measured uncertainties. For each measured orbit, the measured data points are connected with a straight line, which guides the eye. Of course the beam is deflected in between the measured points, since it goes off-centered through quadrupole magnets. The resulting dipole field deflects the beam. The predicted and measured orbits agree very well. Besides the measurements with BPMs bpmx16 ($s = 87.5$ m) and bpmx20 ($s = 118.1$ m), the deviation between

7. Orbit Response Matrix

the measured and the predicted orbit is within the error compatible.

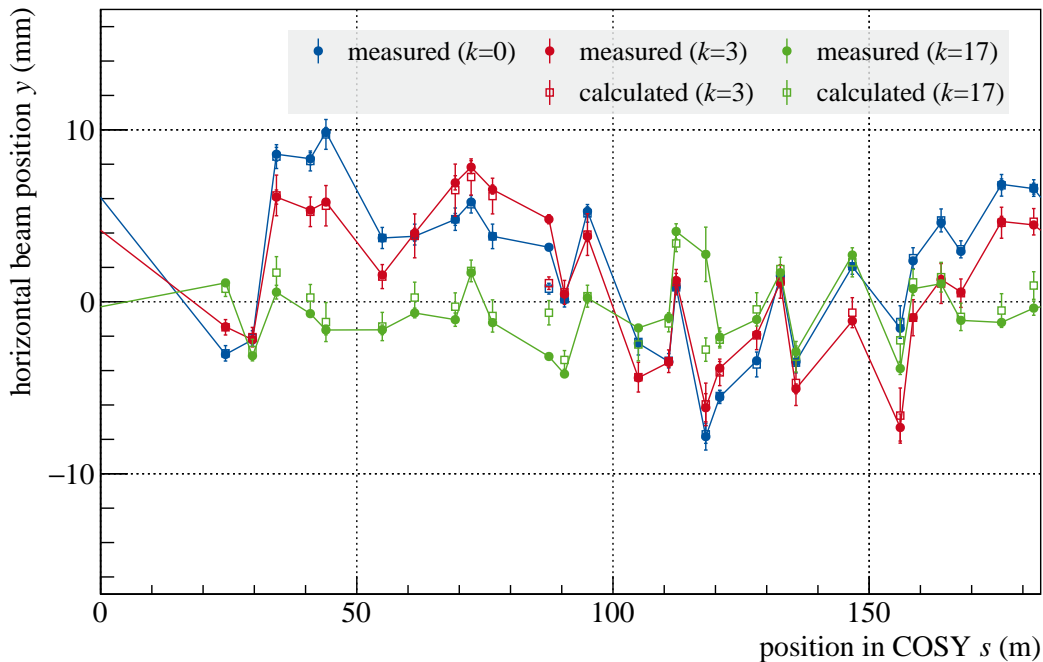


Figure 7.13.: The measured horizontal uncorrected orbit is shown in blue. The prediction of the residual orbit for different regularization parameters k is indicated with open squares. The corresponding measured orbit is plotted on top with filled dots. The lines are only drawn to guide the eye. Besides the beam position measurements at $s = 87.5$ m and $s = 118.1$ m the predicted and the measured orbit are within the errors in perfect agreement.

To compress the information of the orbit quality and the prediction quality in one number, the RMS of the orbit is calculated. This estimation is done for the residual orbit calculated by using the TSVD method for all k values. The resulting curves for the horizontal and the vertical RMS value including an error band are plotted in Fig. 7.15 in red resp. blue. The RMS value is decreasing with an increasing regularization parameter up to the smallest value, which is achievable with the measured ORM and the available corrector magnets. In addition, the RMS values of the measured orbit for the regularization parameters 3, 7, 9, 17 and 35 are indicated as red and blue points, including the measured uncertainty. The measured RMS values follow the predicted dependence on the regularization parameter, but they are always above the predicted curve. The deviation between the prediction and the measured RMS increases with increasing regularization parameter from 0.1 mm to 0.4 mm. This increase can be explained, since the ORM is a linear approximation of the optical lattice of

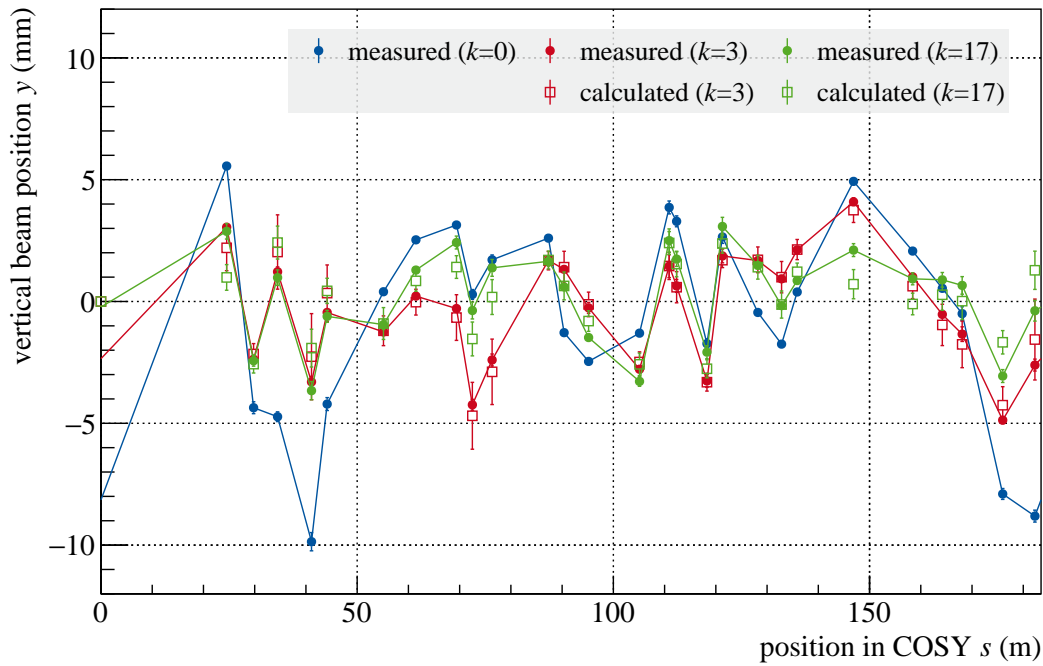


Figure 7.14.: *The measured vertical uncorrected orbit is shown in blue. The prediction of the residual orbit for different regularization parameters k is indicated with open squares. The filled dots represent the measured orbit, after applying the corrector strengths $\hat{\theta}_k$. The lines are drawn to guide the eye. The prediction and the measurement are within the error bars in good agreement.*

the accelerator. Higher order terms, which can occur are not included in the correction scheme. In addition, measurement errors in the matrix are amplified with increasing regularization parameter k and should be included in the error band. But since the ORM measurement is done once and the orbit correction was done once, a statistical statement is not possible at this stage. As an additional point, the distribution of the perturbation and the bias function indicate, that the correction runs into saturation at the regularization parameter $k \approx 17$, which is compatible with the measured RMS values for $k = 17$ and $k = 35$. All four RMS values are in the same range of 1.7 mm to 2.1 mm.

In summary, the developed method of measuring the ORM, calculating the correction strengths, predicting the residual orbit as well as correcting the orbit behave as expected. The correction method is used in the development of an orbit feedback system, which is described below.

One important question to address is: Why is the residual orbit RMS in the order of 2 mm settled and no further correction possible? Is this a problem

7. Orbit Response Matrix

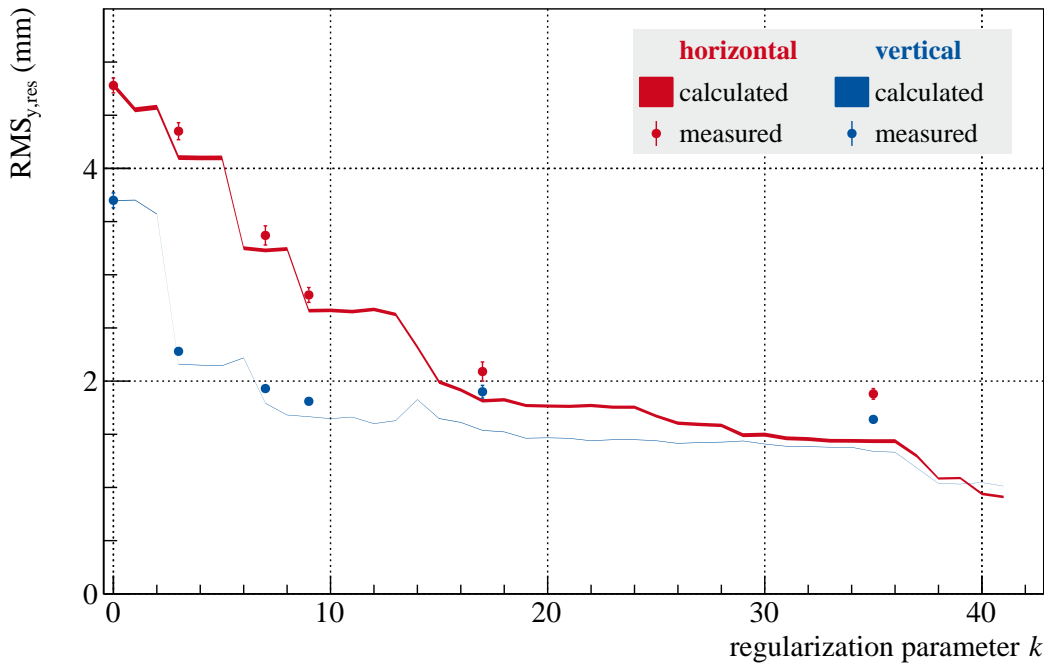


Figure 7.15.: The RMS of the vertical and horizontal orbit after the correction (7.50) is calculated for each k value. For six values the correction was applied. The resulting orbit RMS values are indicated as well.

of the correction method, a lack of BPMs, a lack of corrector magnets, or a problem of the BPM resolution? These questions are investigated in the next section supported by simulations.

7.3.4. Further Developments toward Orbit Feedback System

The existing control system of COSY is designed to feed forward the settings of all magnets as predefined ramps, before starting the injection process. All results presented are measured by using this system. In cooperation with the external company COSYLab¹ the developed algorithm is implemented in a new EPICS² based control system. This implementation allows for online orbit correction during the storage of the particles, without a predefined ramp. This correction scheme is in the commissioning phase (2016-2017). Later on it will be used for the correction of time dependent instabilities of power supplies over the storage time.

¹COSYLAB: Control SYstem Laboratory, <http://www.cosylab.com> (visited 2016/12/13)

²Experimental Physics and Industrial Control System, <http://www.aps.anl.gov/epics/> (visited 2016/12/13)

7.4. Simulations

The question, why is the orbit RMS after the correction not better than ≈ 2 mm is the leading question to the simulations, presented in the following. For the simulations of the closed orbit, the program package MAD-X [95] is used and extended. Within this package, all magnets of the accelerator can be placed and the closed orbit is calculated at each element. The program is extended to perform orbit correction with the same method as the one, implemented for the real storage ring COSY. For example the ORM is estimated by varying the kicker strength of single correction magnets and calculating the response at all BPMs. The orbit correction is done by using the same algorithm, described above.

The starting point of the simulations is an accelerator design, where all elements are aligned perfectly and the settings are adjusted in a way, that the horizontal and vertical tune as well as the dispersion are equal to the setup of COSY, which is used for the deuteron measurements performed to study the feasibility of measuring the deuteron's EDM. The optical functions, the horizontal and vertical beta functions β_x , β_y and the dispersion D are shown in Fig. 7.16.

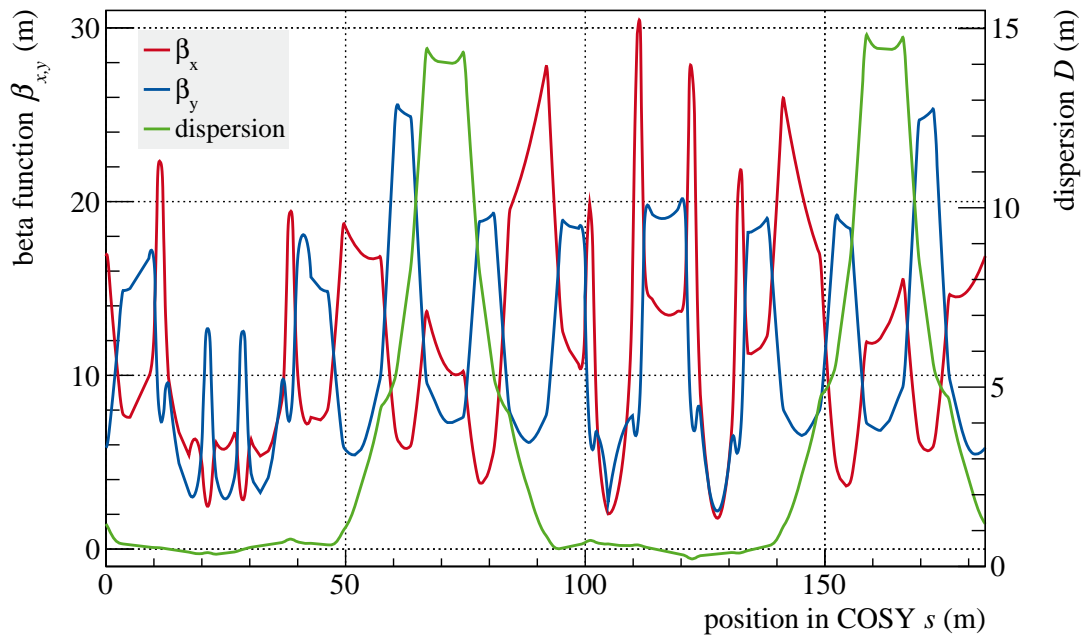


Figure 7.16.: The beta functions β_x (red), β_y (blue) as well as the dispersion D (green) are depicted.

With perfectly aligned magnets, the orbit is centered in all elements and no further correction is needed. To get a disturbed orbit in vertical and horizontal

7. Orbit Response Matrix

direction, magnets need to be moved. This is done by moving the bending dipoles and the quadrupoles in all three directions and rotating them around these directions as well. In addition to the alignments, the influence of the BPM resolution can be analyzed.

The simulation steps and the upcoming corresponding sections are ordered in the following way. First the connection between the magnet alignment resolution and the closed orbit RMS is analyzed. On top of these results, the BPM resolution is investigated. At the end, additional correction elements like BPMs and corrector magnets are added to the simulation. These steps allow a study of the theoretical limit of the orbit quality, by assuming a realistic alignment precision of the magnets. The combination of these effects is presented at the end and in combination with the simulations presented in [16] a possible EDM limit is derived.

7.4.1. Misalignment of Quadrupoles

For the study of the influence of the quadrupole alignment on the orbit quality, all quadrupoles are randomly misaligned with Gaussian distributed misalignments:

$$z = z_0 + \Delta z \quad z \in \{x, y, s, \theta, \psi, \varphi\}, \quad (7.59)$$

where Δz is randomly generated following the Gaussian probability function:

$$p(\Delta z) = \frac{1}{\sqrt{2\pi}\sigma_z} \exp\left(-\frac{(\Delta z)^2}{\sigma_z^2}\right). \quad (7.60)$$

The width of the Gaussian distribution is varied from $0.2 \mu\text{m}$ to 1.3mm resp. $0.2 \mu\text{rad}$ to 1.3mrad . For 10 000 randomly generated misalignments, the orbit RMS value at the BPMs is calculated and the orbit correction with respect to the BPMs is performed. For these calculations, perfectly aligned BPMs with a perfect resolution are assumed. The resulting distributions are shown in Fig. 7.17. The blue graphs show the uncorrected case, whereas the red areas represent the corrected orbit. The filled error band includes 68% of the simulated data points, whereas the error bars represent all data points. For all four curves, a linear function is fitted to the data points:

$$\log(RMS_{\text{ideal}}) = f \cdot \log(\sigma). \quad (7.61)$$

The slope f of these functions is the conversion factor between the alignment precision and the resulting orbit RMS. The resulting fit parameters are summarized in Tab. 7.2. For both planes, the RMS value in millimeter of the uncorrected orbit is one order of magnitude higher than the misalignment in

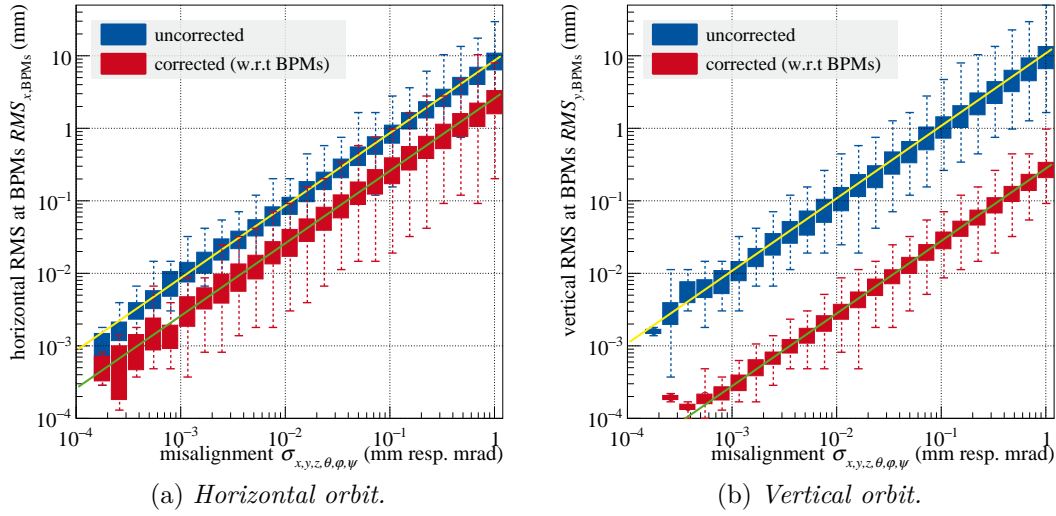


Figure 7.17.: *The horizontal orbit RMS at the BPMs depending on the magnet misalignment. The uncorrected orbit RMS is shown in blue. The result of the orbit correction, with respect to the BPMs, is shown in red. The BPMs are assumed as perfectly aligned and measuring with a perfect resolution. The filled areas represent the 68% error band, the error bars represent all data points. The yellow and green lines are fits to the data points, corrected resp. uncorrected.*

Table 7.2.: *The conversion factors between the orbit RMS at the BPMs and the alignment resolution are summarized for both planes for the uncorrected and the corrected cases.*

plane	corrected / uncorrected	conversion factor f
horizontal	uncorrected	8.6
vertical	uncorrected	10.8
horizontal	corrected	2.6
vertical	corrected	0.3

millimeter respectively milliradian. The corrected orbit is obtained, by using the TSVD method iteratively until the change in the orbit RMS is less than 2%. In the vertical plane, the RMS of the corrected orbit is reduced by a factor of 50, which leads to an orbit RMS, which is 30% of the assumed alignment resolution of the magnets. For the horizontal plane, the correction reduces the RMS only by a factor of 5. This shows, that the horizontal orbit can only be corrected to an RMS value, which is in the same range as the assumed alignment resolution.

In order to compare the resulting RMS to the one which is crucial for an EDM

7. Orbit Response Matrix

measurement, a translation between the RMS measured with the BPMs and the RMS of the beam position within the quadrupoles is important, because the horizontal field components of the quadrupoles are the main sources for EDM like signals, since they produce for a vertically off-centered beam the biggest horizontal magnetic fields. These fields lead to a polarization build up in vertical direction by running an RF Wien filter in EDM mode. The translation between the RMS measured at the BPMs and the RMS within the magnetic quadrupoles are estimated by using the simulation. Figure 7.18 shows the corresponding graphs. For the horizontal and the vertical orbit, the RMS value is calculated at the quadrupoles and plotted against the RMS calculated at the BPMs. For the uncorrected case (blue), the RMS values measured with the BPMs represent the beam RMS in the magnets, since the data points lie on top of a bisecting line, which is drawn in the diagram. For the corrected case (red), the RMS values measured with the BPMs represent the beam RMS in the magnets, since the data points lie on top of a bisecting line, which is drawn in the diagram.

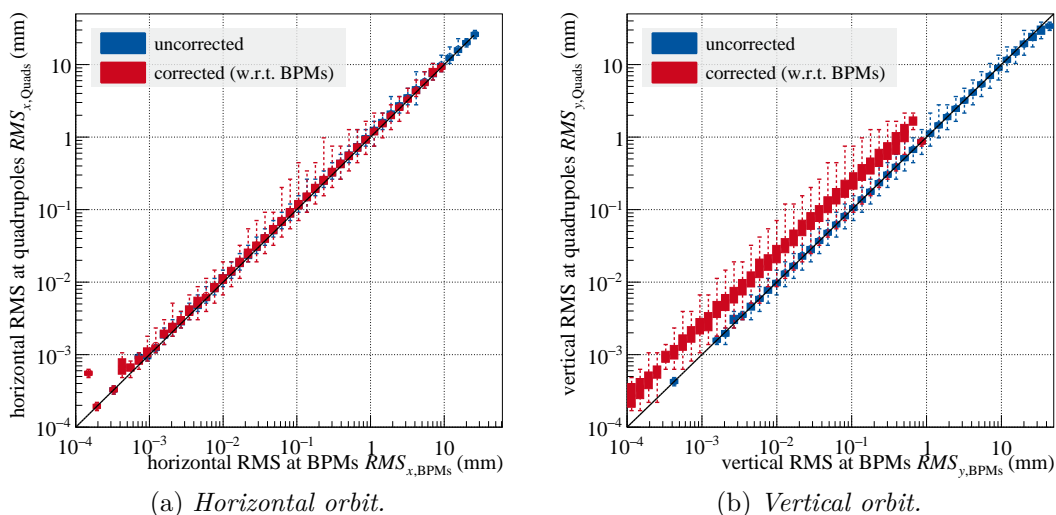


Figure 7.18.: *The orbit RMS at the quadrupole positions shown against the orbit RMS at the BPMs. For the uncorrected orbit (blue), the BPM measurements represent the beam position in the quadrupoles. A perfect agreement is indicated by the black line. The corrected orbit, with respect to the BPMs, shows an higher RMS at the magnets than for the BPMs. The BPMs are assumed as perfectly aligned with a resolution of 0.1 mm. The filled areas represent the 68% error band, the error bars represent the minimal and maximal values.*

For the corrected case, the BPMs have a distinguished position: These are the elements, at which the orbit RMS is reduced with the orbit correction. Wheres the orbit at all other elements of the accelerator is ignored by the orbit

correction algorithm. Therefore, the RMS at the BPMs is smaller than the one measured at the quadrupoles. This effect is more visible in the vertical direction than in the horizontal direction. Nevertheless, the orbit RMS measured at the quadrupoles is reduced by the orbit correction. This effect is clearly visible in the vertical case, where the data points for the corrected case are shifted to the left and the bottom of the plot, compared to the data points of the uncorrected case.

The effect of an overall corrected orbit is underlined by comparing the corrected orbit with the uncorrected one at the quadrupole positions. For this comparison the orbit RMS at the quadrupoles is plotted depending on the magnet misalignment, assumed. Figure 7.19 shows the corresponding graphs, which show that all data points of the corrected orbit are below the uncorrected one. In analogy with the case, where the BPMs are investigated the conversion factor

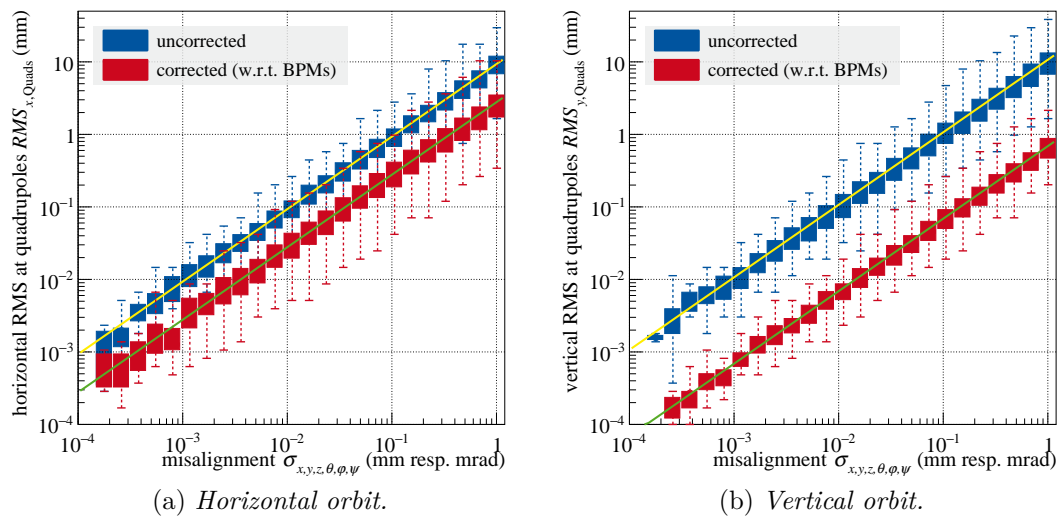


Figure 7.19.: *The orbit RMS at the quadrupole positions depending on the magnet misalignment. The uncorrected orbit (blue) has the same RMS as the uncorrected orbit measured at the BPMs (cp. Fig. 7.17). The corrected orbit is below the uncorrected one. This shows, that a global orbit correction with only using the BPM information is possible. The filled areas represent the 68% error band, the error bars represent the minimal and maximal values.*

between the misalignment and the quadrupole RMS is calculated and indicated by straight lines. The yellow lines correspond to the uncorrected case and the green ones to the corrected one. The conversion factors are summarized in Tab. 7.3.

Overall, the orbit RMS can be corrected by factors 3 and 36 for the horizontal,

7. Orbit Response Matrix

resp. vertical plane, by considering the RMS at BPMs. For the RMS measured at quadrupoles, the factors are 3 (horizontal) resp. 15.3 (vertical). These factors show, that the horizontal beam positions can be corrected at the quadrupoles by using the BPM information. For the vertical plane, the correction is also possible, but the gain in the orbit RMS at the quadrupoles is a factor 2 worse than the one at the BPMs.

Table 7.3.: *The conversion factors between the orbit RMS at the quadrupole magnets and the alignment resolution are summarized for the uncorrected and the corrected cases, each in both planes.*

plane	corrected / uncorrected	conversion factor f
horizontal	uncorrected	9.3
vertical	uncorrected	10.7
horizontal	corrected	2.8
vertical	corrected	0.7

7.4.2. BPM Resolution

In addition to the mentioned alignment precision, the resolution of the BPMs is a crucial point for the orbit correction quality. For the following simulations, the same generated random numbers are used as for the simulation with ideal BPMs. Besides the alignment of the magnets, the measured beam positions at the BPMs are smeared with a Gaussian distribution with a mean of 0 mm and a width of 0.1 mm, which is an optimistic value for the BPMs at COSY, if the gain uncertainty is treated as statistical error (see chapter 6). Assuming this resolution and perfectly aligned BPMs, the figures presented in the previous section change to the following.

First of all, the measured RMS at the BPMs depending on the magnet alignment for uncorrected and corrected orbits is presented in Fig. 7.20. For large misalignments, the curves are identical to the ones obtained with perfect BPMs. Following the uncorrected curves from large misalignments to low ones, the RMS values start to diverge from a straight line at around 0.2 mm and follow asymptotically to the BPM resolution of 0.1 mm. This effect can be described by calculating the first moment of the RMS distribution (cp. A.1), which results in:

$$\langle RMS_{\text{realistic}}(\lambda) \rangle = \sqrt{\frac{\pi}{2}} L_{1/2}^{(N/2-1)} \left(\frac{-\lambda^2}{2} \right) \frac{\sigma}{\sqrt{N}}. \quad (7.62)$$

In this equation, $L_{1/2}^{(N/2-1)}(x)$ are the generalized Laguerre polynomials and λ reads:

$$\lambda = \sqrt{\sum_{i=1}^N \left(\frac{\mu_i}{\sigma_i}\right)^2} \approx RMS_{\text{ideal}} \frac{\sqrt{N}}{\sigma}. \quad (7.63)$$

In this equation, μ_i is the beam position at BPM i and σ_i is the resolution of BPM i . In the approximation all BPMs are assumed to have the same resolution $\sigma_i = \sigma$. The ideal value RMS_{ideal} for the orbits is calculated by using the fit functions (7.61), obtained with ideal BPMs. The calculated expectation value by using (7.62) and (7.63) of the realistic RMS is plotted above the corresponding data points as a yellow resp. green line in Fig. 7.20. The uncorrected data points are described very well.

For the corrected orbit, the orbit RMS follows the calculated curve, but is always above the predicted curve. This effect can be explained with the example of perfectly aligned magnets:

The correction algorithm has the goal to minimize the measured orbit, including the BPM uncertainty. If, for example, the real orbit is perfectly at 0 and only the BPM resolution dominates the measured orbit, the correction algorithm searches for a solution which minimizes the measured beam position at each BPM $x_i \neq 0$. After the correction, the beam is "corrected" to the positions $-x_i$, which results in the same RMS as before the correction. In addition, the uncertainty of the beam position measurement is added to the new beam positions $-x_i$, which can be calculated by:

$$\langle RMS_{\text{cor,realistic}} \rangle = \langle RMS_{\text{realistic}} (\langle RMS_{\text{realistic}}(0) \rangle) \rangle \quad (7.64)$$

$$= \sqrt{\frac{\pi}{2}} \frac{\Gamma((N+1)/2)}{\Gamma(N/2) \Gamma(1.5)} \cdot \frac{\sigma}{\sqrt{N}}. \quad (7.65)$$

For the used example of $\sigma = 0.1$ mm, the resulting limit of the corrected orbit is indicated by a black line in Fig. 7.20. The simulated corrected orbit (red error band) converges towards this line for good alignment resolutions. For large misalignment errors, compared to the BPM resolution, the corrected orbit follows the one obtained with perfect BPMs.

One additional and important question is the orbit quality at the quadrupoles after the correction with realistic BPMs. To answer this question, the orbit RMS measured at the quadrupoles is plotted against the assumed alignment precision, shown in Fig. 7.21.

For large misalignments, compared to the BPM resolution, the corrected and uncorrected orbit curves follow exactly the ones, obtained with perfect BPMs. The corrected orbit diverges from this ideal case at the point, where the alignment resolution is the same as the BPM resolution. Below this point, the orbit

7. Orbit Response Matrix

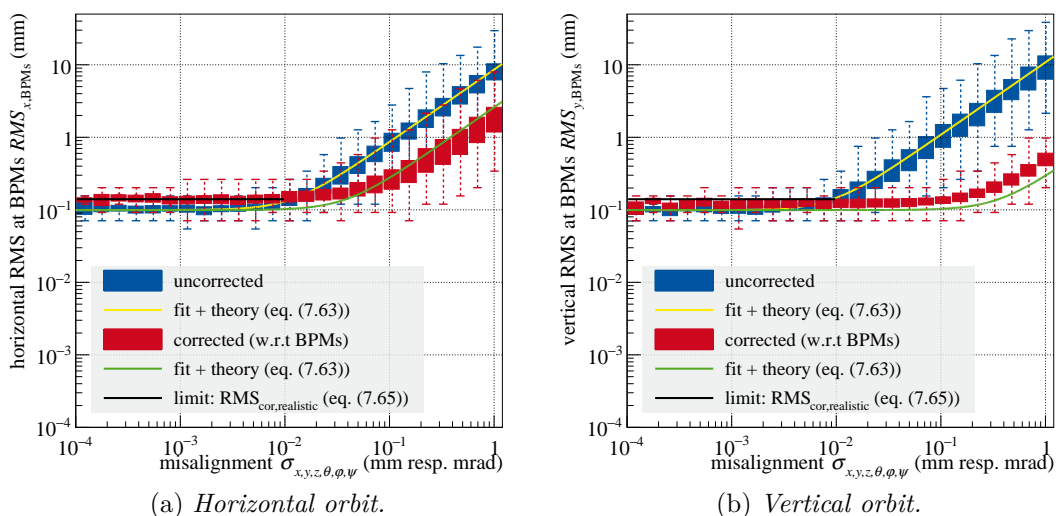


Figure 7.20.: The orbit RMS measured at the BPMs depending on the magnet misalignment. The uncorrected orbit RMS is shown in blue. The corrected orbit, with respect to the BPMs is shown in red. The BPMs are assumed as perfectly aligned with a resolution of 0.1 mm. The filled areas represent the 68% error band, the error bars represent the minimal and maximal values.

RMS at the quadrupoles converges towards the resolution of the BPMs, which can be explained by the same mechanism, which explains the asymptotic behavior of the RMS measured at the BPMs.

As a conclusion, the orbit correction is limited by the BPM resolution if the alignment precision of the magnets is in the same order as the BPM resolution. Above this point, the BPM resolution can be neglected and the limiting factor is the precision of the magnet adjustment.

7.4.3. Alignment of Dipoles and Quadrupoles

The position of the dipole magnets and the quadrupole magnets, with respect to the nominal value, were measured during a maintenance period in April 2016 by the company Vermessungsbüro H.-J. Stollenwerk. The position of each magnet was measured to a precision of 0.01 mm.

The distributions of the longitudinal and horizontal positions of the 24 dipole magnets is presented in Fig. 7.22. The distribution of the longitudinal positions

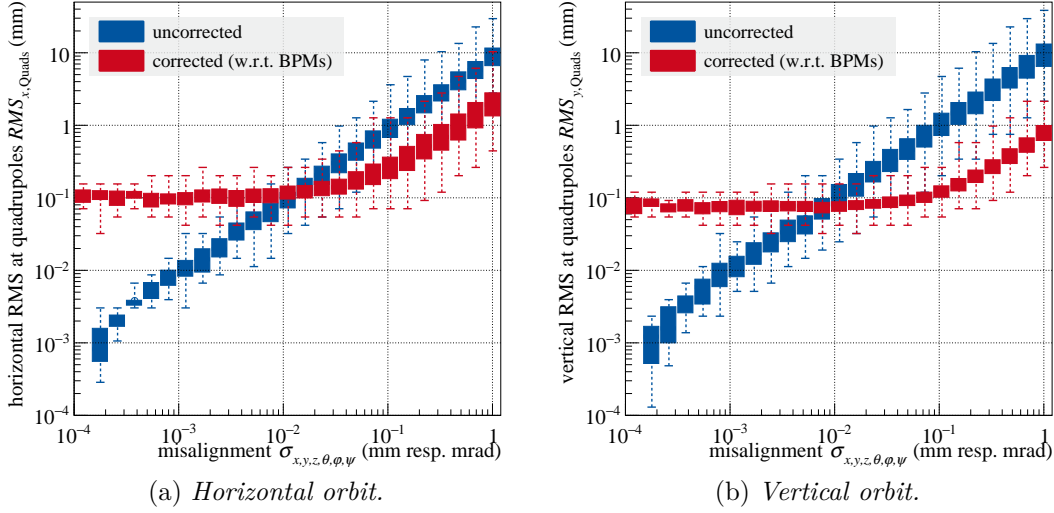


Figure 7.21.: *The orbit RMS at the quadrupole positions depending on the magnet misalignment. The uncorrected orbit (blue) has the same RMS as the uncorrected orbit measured at the BPMs (cp. Fig. 7.17). The corrected orbit is below the uncorrected one. This shows, that a global orbit correction with only using the BPM information is possible. The filled areas represent the 68% error band, the error bars represent the minimal and maximal values.*

is centered at -0.1 mm and has a width of 0.6 mm. The parameters of the horizontal distribution are 0.2 mm for the mean value and 0.4 mm for the standard deviation.

Figure 7.23 depicts the distributions of the longitudinal and horizontal positions of the quadrupole magnets. In comparison to the dipole distributions, the ones of the quadrupoles are much wider. The standard deviation for the longitudinal position is 4 mm, the one for the horizontal position is 0.7 mm.

Multiplying these numbers by the conversion factors for the corrected orbit, results in RMS values of the orbit, which are in the order of

$$RMS_{\text{hor}} = 2 \text{ mm} \quad (7.66)$$

$$RMS_{\text{ver}} = 0.5 \text{ mm}. \quad (7.67)$$

The horizontal orbit RMS is in the same range as the one achieved after orbit correction at COSY (1.9 mm). For the vertical orbit, the achieved orbit RMS after correction is ≈ 1.7 mm, which is a factor 3 larger than the one expected from the survey estimation. Possible explanations are the non Gaussian distribution of the magnet positions, which is not included in the simulation. Additionally,

7. Orbit Response Matrix

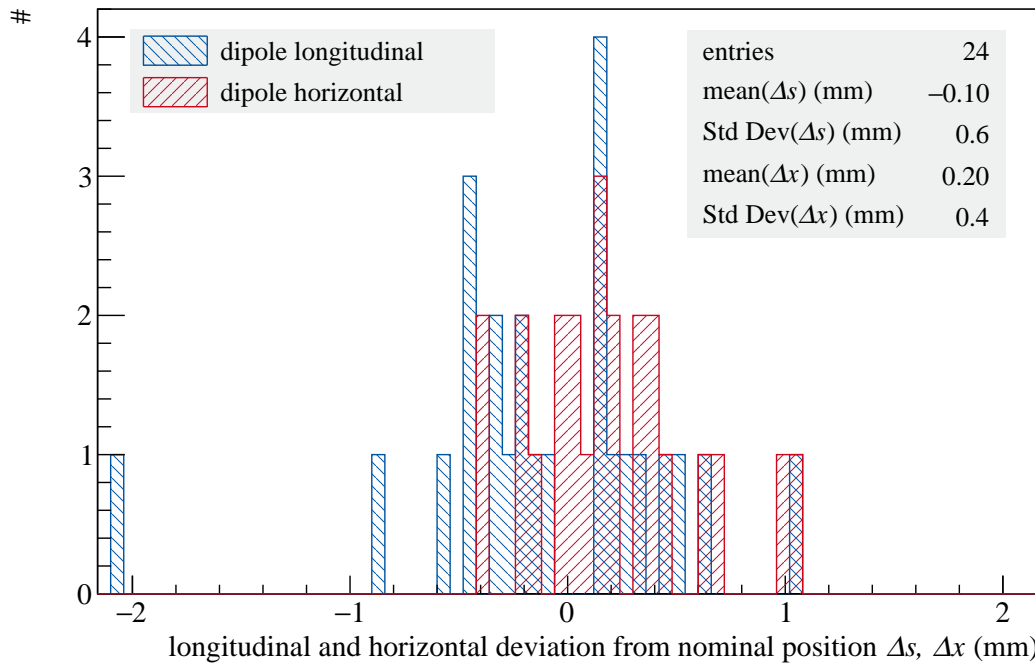


Figure 7.22.: *Distribution of the dipole position deviations, measured during a survey in April 2016. The horizontal deviation from the nominal value are displayed in red, the longitudinal one is shown in blue.*

the BPMs are not considered in the survey and since the position deviations of the magnets are much larger than expected before the survey, the BPMs can of course diverge from their nominal position in the same way as the magnets. All in all, the survey shows, that the magnets moved slightly over the 20 years of COSY operation and have to be repositioned for an EDM measurement. The process of realigning the magnets started during the maintenance of COSY in the winter 2016/2017. If the magnets can be aligned to 0.1 mm and 0.1 mrad or better, the corrected orbit should improve as well. The orbit RMS of the corrected orbit is expected to:

$$RMS_{\text{hor}} = 0.26 \text{ mm} \quad (7.68)$$

$$RMS_{\text{ver}} = 0.03 \text{ mm}, \quad (7.69)$$

which is in the resolution and accuracy of the existing BPM system and maybe not measurable with this system.

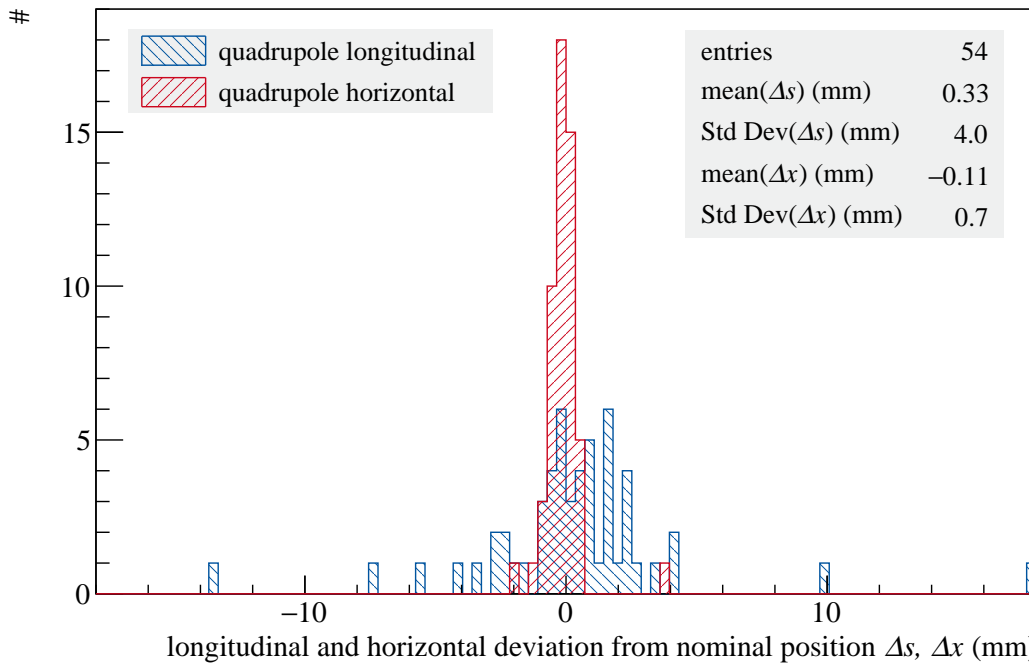


Figure 7.23.: *Distribution of the quadrupole magnet position deviations, measured during a survey in April 2016. The horizontal deviation from the nominal value are displayed in red, the longitudinal one is shown in blue.*

7.4.4. Additional Elements

The simulations, discussed up to now, point out that the orbit RMS is dominated by the alignment resolution. One way of improving the RMS is an alignment of all magnets with a higher precision. A second way is the update of the correction system, which can include additional BPMs or additional corrector magnets or a combination of both. In the following the effect of additional correction elements is investigated. As a reference the presently installed BPMs and corrector magnets at COSY are shown and labeled as default.

The important characteristic numbers are the orbit RMS values calculated at all elements, which is possible in the simulation framework. In the focus of an experiment, the RMS can only be calculated by using the BPM measurements, therefore the BPM measurement results are presented as well. First of all the effect of additional BPMs is discussed, followed by a discussion of additional corrector magnets. As a third point the combination of both is presented and the overall improvement of the orbit quality is pointed out.

7. Orbit Response Matrix

Additional BPMs As a starting point, additional BPMs for both planes are installed at each quadrupole. With this setup, the correction algorithm uses the default corrector magnets, the default BPMs and the additional BPMs. The resulting orbit correction strength is estimated analogously to the conversion factor between misalignment and orbit RMS for the default correction system (cp. 7.4.1), but in addition, the guiding dipoles are randomly shifted as well. The conversion factors between the alignment precision and the RMS measured at the BPMs are:

$$f_{\text{BPM,hor}} = 0.33 \quad (7.70)$$

$$f_{\text{BPM,ver}} = 0.49. \quad (7.71)$$

The factors concerning the overall RMS are in the same range, but a little bit larger:

$$f_{\text{all,hor}} = 0.40 \quad (7.72)$$

$$f_{\text{all,ver}} = 0.51. \quad (7.73)$$

Additional Corrector Magnets As additional corrector magnets, quadrupoles can be used by adding windings in a way, that they produce a dipole field. Since this method is a simple way of adding corrector dipoles, all quadrupoles are used as additional corrector magnets in the simulation. The default BPMs are used as BPM system in the correction algorithm. The resulting conversion factors are:

$$f_{\text{BPM,hor}} = 0.001 \quad (7.74)$$

$$f_{\text{BPM,ver}} = 0.006 \quad (7.75)$$

$$f_{\text{all,hor}} = 0.28 \quad (7.76)$$

$$f_{\text{all,ver}} = 0.24. \quad (7.77)$$

In comparison to the numbers, estimated by using additional BPMs, the discrepancy between the RMS BPMs and the overall RMS is obvious. This effect is explained, by the fact, that with additional corrector magnets, a perfect correction at the BPMs is nearly possible. But the RMS at other elements, between the BPMs, is not included in the correction algorithms, since the beam position can not be measured at these elements. Nevertheless, the orbit RMS at all elements is a factor ≈ 3 better than the default setting.

Additional Corrector Magnets and BPMs The combination of additional corrector magnets and additional BPMs result in the best orbit after the cor-

rection. The conversion factors reduce to:

$$f_{\text{BPM,hor}} = 0.068 \quad (7.78)$$

$$f_{\text{BPM,ver}} = 0.01 \quad (7.79)$$

$$f_{\text{all,hor}} = 0.10 \quad (7.80)$$

$$f_{\text{all,ver}} = 0.11. \quad (7.81)$$

In this configuration, the orbit RMS at all elements can be reduced by factors of ≈ 8 (horizontal) and ≈ 6 (vertical) compared to the default correction elements.

Summary of Additional Elements All conversion factors for the presented upgrade with additional corrector magnets and additional BPMs are presented in Fig. 7.24 and summarized in Tab. 7.4.

Table 7.4.: *The conversion factors between magnet alignment precision and orbit RMS for different orbit correction system upgrade scenarios are listed. The scenarios include additional corrector magnets and/or additional BPMs. The factors are calculated for the horizontal and vertical planes.*

plane	correction system	BPM system	conversion factors	
			f_{BPMs}	f_{all}
horizontal	default	default	0.22	0.83
	default	add BPMs	0.33	0.40
	add correctors	default	0.0010	0.28
	add correctors	add BPMs	0.068	0.10
vertical	default	default	0.32	0.65
	default	add BPMs	0.49	0.51
	add correctors	default	0.0063	0.24
	add correctors	add BPMs	0.01	0.11

The blue bars represent the factors corresponding to the RMS measured at the BPMs, whereas the red bars correspond to the RMS measured at all elements. For the presently installed system at COSY, the RMS at all elements is a factor 4 (horizontal) and a factor 2 (vertical) higher than the ones measured at the BPMs. By upgrading the BPM system, the RMS measured at the BPMs and the one averaged over the accelerator, approach each other at ≈ 0.4 . The RMS at all elements decreases, whereas the RMS at the BPMs increases. For the upgrade of only the corrector magnet system, the RMS values decrease. Especially the RMS conversion factor at the BPMs reaches 0.006 (horizontal) and 0.001 (vertical). In perspective of the EDM measurement, the RMS at all

7. Orbit Response Matrix

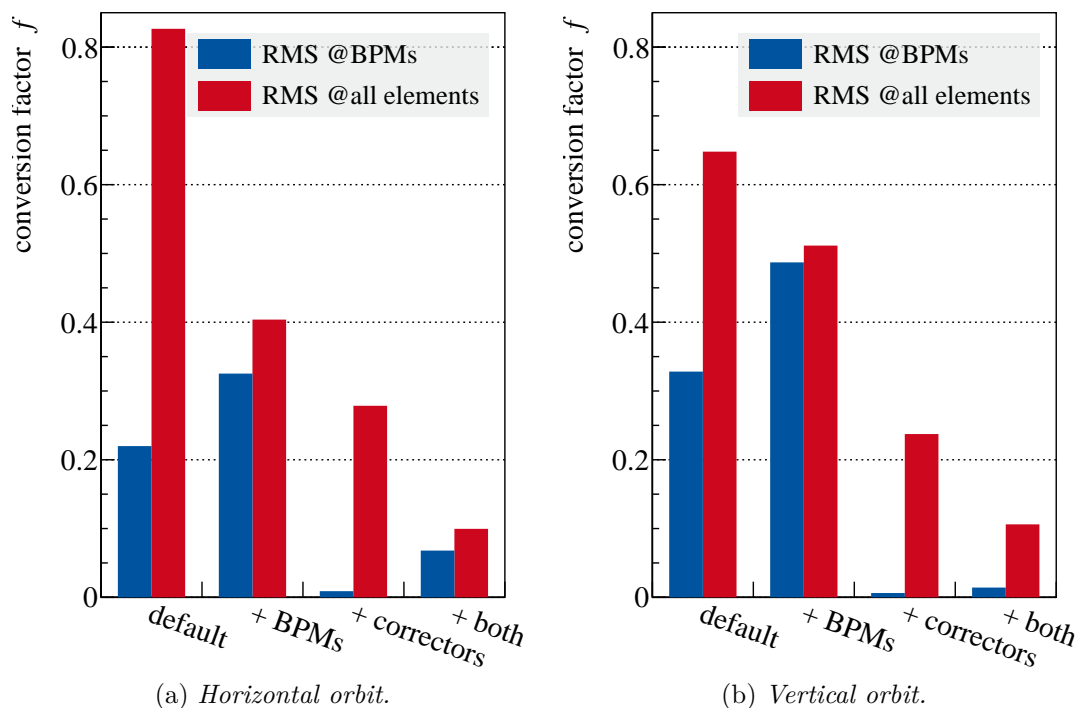


Figure 7.24.: The conversion factor f between the alignment resolution and the orbit RMS after correction is presented in the two diagrams for different combinations of additional corrector magnets and additional BPMs. In addition to the existing COSY systems ("default"), additional dipole windings are installed at the quadrupoles and/or additional BPMs are installed inside the quadrupoles. The RMS is calculated at the BPMs (blue), including the additional ones, and at all elements (red). The calculation is done for the horizontal and the vertical orbits.

elements is the important value, which is lower than the one with only upgraded BPMs. For the combination of both upgrades, the RMS values approach each other and decrease significantly.

The best upgrade option is the upgrade of both systems, which is complicated since there is no space available for the installations of new BPMs. The second-best solution is the installation of additional windings on the quadrupoles, which improves the quality of the orbit correction by a factor of 3 in the horizontal case and a factor of 2.7 in the vertical case. This improvement is directly proportional to the systematic EDM limit, depicted in [16].

For example, the orbit can be improved by aligning the magnets with a resolution of 0.1 mm, which started end of 2016. This will lead to a corrected

orbit RMS of 0.08 mm and 0.065 mm for the horizontal resp. vertical direction. With the possible installation of additional quadrupole windings, the RMS can be improved to 0.03 mm resp. 0.01 mm. Of course, the BPM resolution has to be better than the RMS of the orbit, which will be the case for the upgraded readout electronics. With an achievable vertical RMS of 0.01 mm, the EDM measurement is systematically limited to $d_{\text{EDM}} \approx 5 \cdot 10^{-21} e \text{ cm}$.

8. Systematic Effects on Spin Motion

For the EDM measurements, the influence of the ORM and the orbit correction on the spin motion is of interest. Therefore a measurement of an ORM and in parallel monitoring the spin tune was performed and analyzed. The spin tune ν_s (4.30), the number of spin precessions during one particle revolution, can be measured by using the EDDA detector with a precision of $1 \cdot 10^{-10}$ within 100 s [71]. Since the spin tune determination is the most precise measurement of a quantity at COSY, it can be used as a tool to measure other quantities of COSY.

8.1. Dispersion Measurements at the Corrector Magnets

Varying the strength of the corrector magnets and monitoring the spin tune in parallel, makes the measurement of the horizontal dispersion function at the corrector magnets possible. Usually the dispersion function is only measured at the BPMs, whereas it is unknown in between. In the following a dispersion measurement at the corrector magnets done in December 2015, and a dispersion measurement at the BPMs, done in May 2015, are presented.

8.1.1. Theoretical Model

The connection between the dispersion, the corrector magnet change and the spin tune is derived in the following. The spin tune is in first order given by:

$$\nu_s = \gamma G. \quad (8.1)$$

A relative change of the momentum leads to a change of the Lorentz γ :

$$\frac{\Delta\gamma}{\gamma_0} = \beta^2 \frac{\Delta p}{p_0}. \quad (8.2)$$

8. Systematic Effects on Spin Motion

This change results in a spin tune change:

$$\frac{\Delta\nu}{\nu_0} = \frac{\Delta\gamma}{\gamma_0}. \quad (8.3)$$

Since a kick θ_j with corrector magnet j leads to momentum change (3.46), the spin tune is changed as well:

$$\frac{\Delta\nu}{\nu_0} = -\beta^2 \frac{D_j}{\eta L_0} \theta_j. \quad (8.4)$$

This equation allows for a measurement of the local dispersion at the corrector magnets by knowing the circumference L_0 and the phase slip factor η of COSY. The factor $\frac{\beta^2}{\eta}$ can be measured by changing the cavity frequency and observing relative spin tune changes. This measurement was done during commissioning of a feedback system, which stabilizes the spin tune by adjusting the cavity frequency. The relation of both quantities is given by [72]:

$$\frac{\Delta\nu}{\nu_0} = \frac{\beta^2}{\eta} \frac{\Delta f}{f_0}. \quad (8.5)$$

The spin tune change, measured with 27 different frequencies, is presented in Fig. 8.1. A straight line is fitted against the data points. The spin tune change per frequency change is $(76.9 \pm 0.3) \cdot 10^{-9} \text{ Hz}^{-1}$. In addition to the spin tune change, the nominal spin tune and the nominal revolution frequency were measured. Their results are:

$$f_0 = (750\,599.036 \pm 0.011) \text{ Hz} \quad (8.6)$$

$$\nu_0 = 0.160\,974\,163\,5 \pm 1.7 \cdot 10^{-9} \quad (8.7)$$

Using these measurements result in:

$$\frac{\beta^2}{\eta} = 0.3572 \pm 0.0015. \quad (8.8)$$

Combining this result with (8.4) and inserting the length of COSY L_0 allows the estimation of the dispersion at the corrector magnets.

8.1.2. Spin Tune Monitoring

In order to measure the dispersion at the corrector magnets, the spin tune needs to be monitored during the change of corrector magnets. For the spin tune measurements the following beam manipulations and accelerator settings are essential:

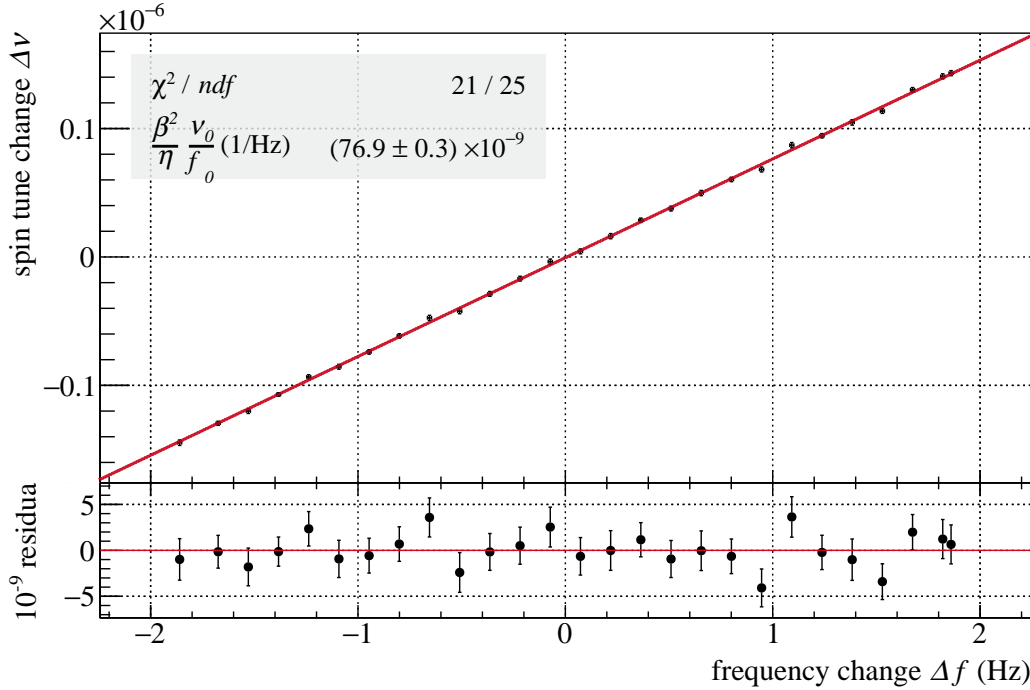


Figure 8.1.: Change of the spin tune induced by a change of the revolution frequency [72]. The nominal revolution frequency is $f_0 = (750\,599.036 \pm 0.011)$ Hz, the nominal spin tune is measured to $\nu_0 = 0.160\,974\,163\,5 \pm 1.7 \cdot 10^{-9}$.

1. The beam is electron cooled for 75 s
2. Moving the beam near a carbon target
3. Start a continuously extraction onto the carbon target with a constant rate
4. All detected scattered particles are time-stamped
5. Flipping the polarization into the horizontal plane by using an RF solenoid
6. Fourier spectra of the time stamped events provide polarization amplitude and phase, latter is used for spin tune interpolation.

Electron Cooling The beam is cooled with the electron cooler [57, 96] to shrink the transverse, as well as the longitudinal phase space. The shrinking of the phase space in addition to a setting with zero chromaticity leads to a spin lifetime, also called spin coherence time, in the horizontal plane of about 1000 s [27, 16].

8. Systematic Effects on Spin Motion

Carbon Target After the cooling process, the beam is moved close to a 17 mm carbon block target, which is fixed 3 mm above the center of the beam pipe at the internal EDDA experimental area. The scattering of the polarized particles and a detection of the ejectiles in the scintillating bars and rings of the EDDA detector allows a determination of the beam polarization as described in 5.2 and in [71, 97].

Continuously Extraction After cooling and moving the beam, it is continuously heated in vertical direction by using a white noise electric field in a strip line unit with a center frequency at the vertical betatron frequency $Q_y f_0$. The heating leads to an expansion of the beam in vertical direction. This expansion results in an overlap of the beam with the target. Particles of the beam are scattered and registered in the detector. The rate in the detector is stabilized by the means of a feedback system, which controls the noise amplitude. The rate in the detector is in the order of 5 kHz [71].

Time Stamping All events in the detector are categorized depending on their azimuth angle in one of the four categories: Up, Right, Down, and Left. In addition to the category, a time stamp with a precision of 92.59 ps is attached to the event. In order to estimate later on the spin tune, the cavity frequency is measured with the same long range time to digital converter [70].

Polarization Flip At injection and during the cooling process, the beam polarization is aligned in parallel to the vertical direction. In order to measure the precession around this axis, the polarization is flipped in the horizontal direction. The flipping is achieved by performing a Froissart Stora scan, which stops exactly at the resonance frequency. At this time, the initially vertical polarization is completely flipped in the horizontal plane [98, 64, 65].

Spin Tune and Polarization Determination The time resolved Fourier spectra of the detector events provides the information needed to determine the polarization amplitude and the spin tune. The amplitude of the Fourier spectra is equal to the up-down asymmetry. This asymmetry is directly proportional to the polarization of the beam. The position of the maximum divided by the measured revolution frequency in combination with the time dependent phase information allows the determination of the spin tune with a precision of $1 \cdot 10^{-9}$ for a time interval of 5 s [71, 72].

8.1.3. Measurement Results

Dispersion Measurement at Corrector Magnets The measurement of the dispersion at the corrector magnets is done in parallel to the measurement of the ORM. In each cycle, a corrector magnet current is changed in five steps. Each of the steps last 5.5 s. The spin tune is determined all over the cycle. The two dimensional water fall plot of one measurement is presented in Fig. 8.2. The top x axis displays the time in seconds after the spin flip is performed. The bottom x axis represents the corresponding kick angle θ . The y axis represents the spin tune proportional to the frequency, whereas the color coded z axis represents the Fourier amplitude A . The position change of the Fourier spectra maximum is clearly visible.

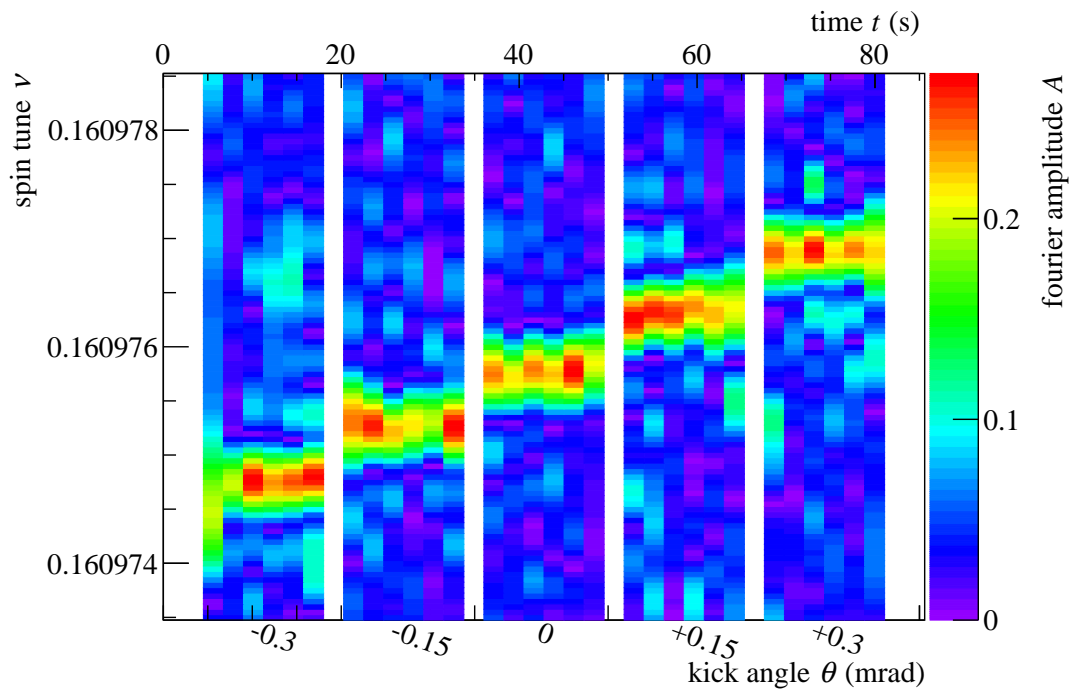


Figure 8.2.: *Spin tune change due to different kick angles at the horizontal corrector magnet 35 ($s = 166.1$ m). The top x -axis represents the time in the cycle. The bottom x -axis displays the corresponding kick angles. The y -axis is a frequency spectra, normalized to the revolution frequency. The fourier amplitude is shown in the color coded z -axis. The spin tune jumps induced by the corrector kick are clearly visible.*

A detailed analysis, including the phase information [72], results in a two dimensional projection of the data, presented in Fig. 8.3. In this view, the y axis represents the relative spin tune change plotted against the kick angle θ

8. Systematic Effects on Spin Motion

(x -axis). The five data points clearly follow within their errors a straight line, which is fitted against the data points. The slope of this line is according to (8.4) proportional to the dispersion. It can be calculated by dividing the slope by $\frac{\beta^2}{\eta^2}$ (8.8) and the circumference $L_0 = (183.473 \pm 0.001)$ m. The resulting dispersion at magnet SH35 reads:

$$D_{\text{sh35}} = (11.09 \pm 0.13) \text{ m.} \quad (8.9)$$

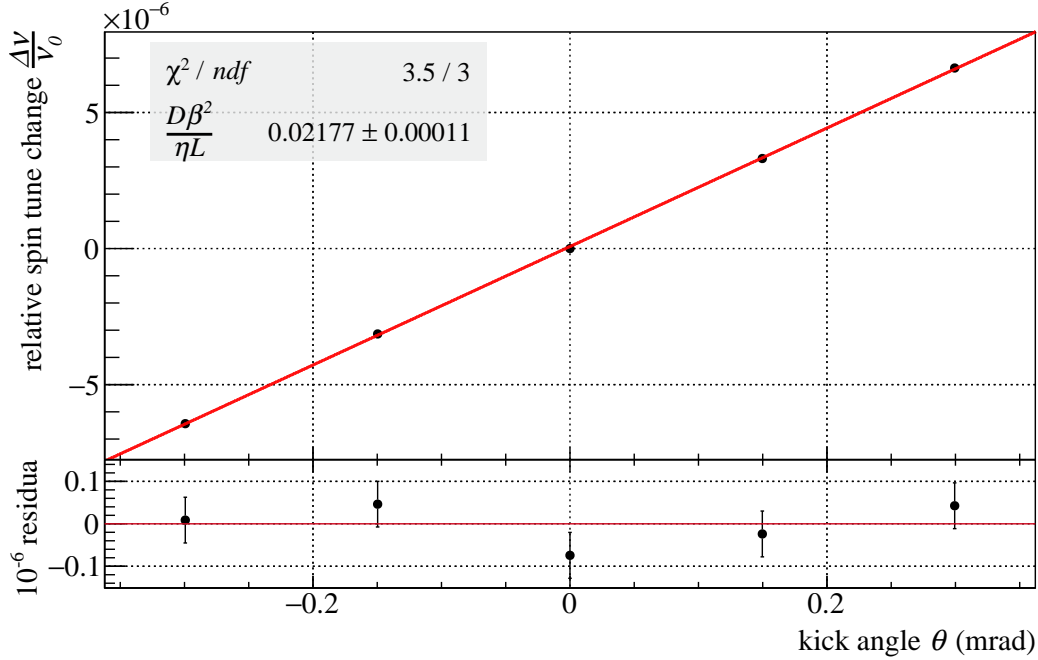


Figure 8.3.: *Relative spin tune change induced by horizontal corrector kicks. The averaged spin tune change for each time interval of Fig. 8.2 is plotted against the kick angle θ . The dispersion D at the corrector magnet position is calculated to $D = (11.09 \pm 0.13)$ m by using the slope of the fitted linear function and the known parameters β, η, L .*

The dispersion measurement, exemplarily explained for corrector magnet sh35, is repeated for all horizontal corrector magnets. In order to compare the measured dispersion at the corrector magnets, a measurement of the dispersion, which was done in May 2015 is analyzed in detail.

Dispersion Measurement at BPMs The usual way to measure the dispersion is to vary the momentum of the beam and measure the resulting orbit change at all BPMs. This procedure leads to the dispersion at the BPMs. Such a

dispersion measurement was performed in May 2015. In this measurement, the frequency of the cavity was changed in steps of 750 Hz. This change leads to a momentum change (3.42), which results in a beam position variation at the i th BPM:

$$\Delta x_i = D_i \eta \frac{\Delta f}{f_0}. \quad (8.10)$$

The dispersion can be calculated with the knowledge of η . Figure 8.4 shows the corresponding dispersion measurement at the horizontal BPM bpmx24. The

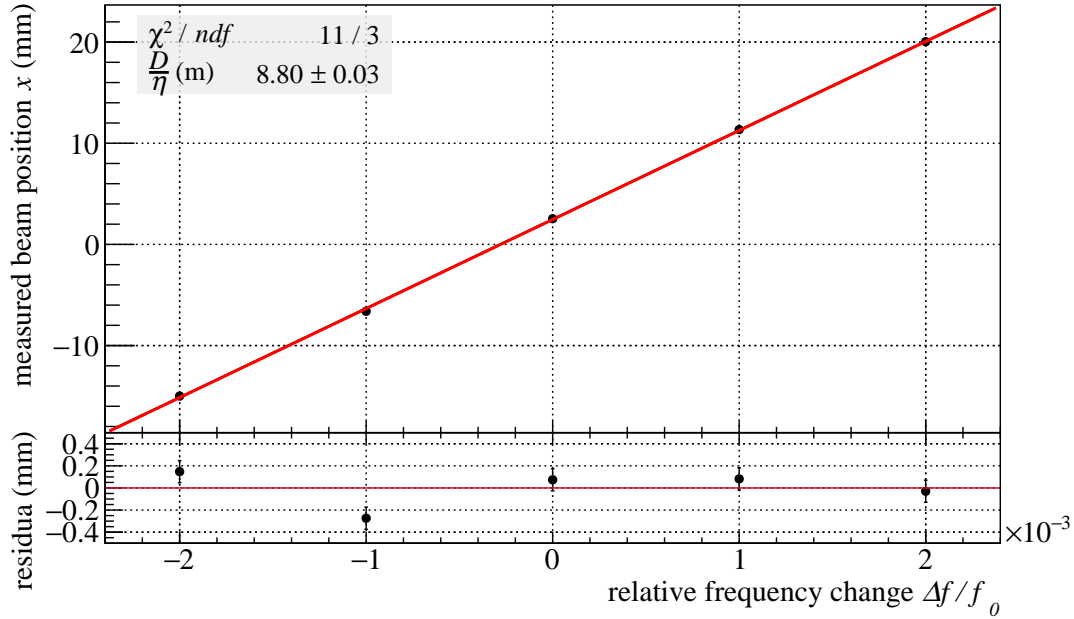


Figure 8.4.: Dispersion measurement with one horizontal BPM bpmx24 ($s = 151.7$ m). The frequency is changed and the corresponding position change is measured. The slope is the dispersion divided by the phase slip factor η .

calculation of the dispersion is done for all BPMs.

Comparison of the Dispersion at BPMs and at Corrector Magnets The dispersion, measured at the horizontal corrector magnets, is plotted as red curve in Fig. 8.5 against the corrector magnet position in COSY. The dispersion measured at the BPMs is depicted in blue. The two arcs of COSY, where the dispersion reaches its maximum value are clearly visible, whereas the dispersion in the straight sections is suppressed. The blue and red curves show the same characteristics. A quantitative comparison is not possible, since the BPMs and the corrector magnets are not at the same position and therefore the dispersion

8. Systematic Effects on Spin Motion

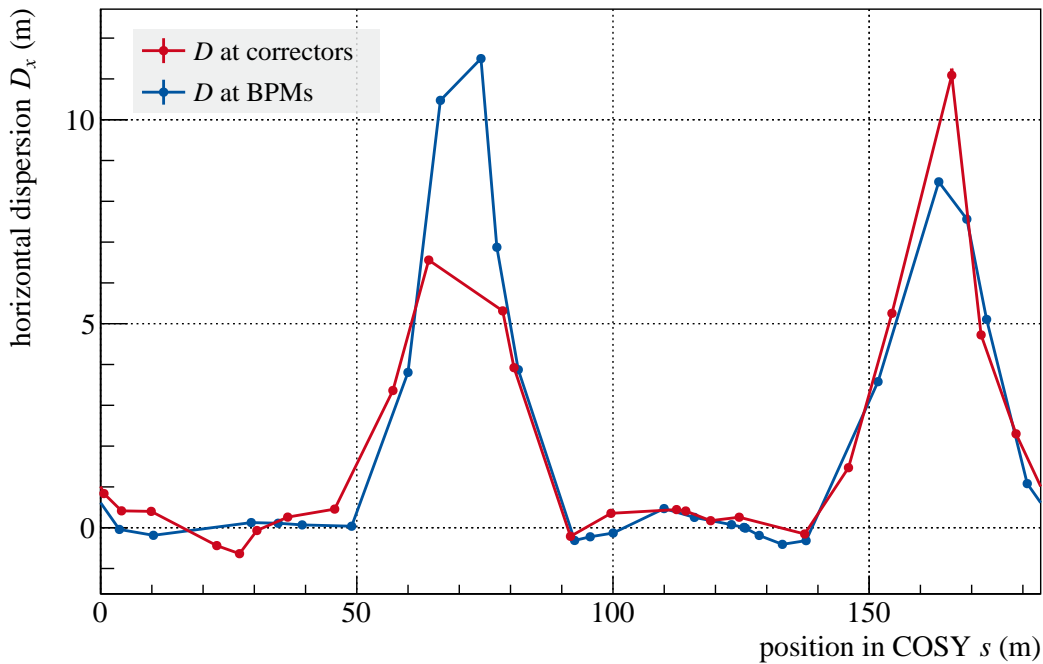


Figure 8.5.: *The dispersion function is measured with BPMs (blue) and by analyzing the spin tune changes due to corrector magnet kicks (red). The blue curve is measured in May 2015, the red one in December 2015 with the same accelerator settings. Considering this time gap between the measurements, they agree very well. The connecting lines are only drawn to guideline the eye.*

is different for both. An additional difference is caused by the fact, that both measurements are taken with a time difference of six months. In principle, the settings are reloaded, but fine tuning was done to adjust beam lifetime, spin lifetime, tunes, chromaticity as well as the extraction process of COSY. This fine tuning can result in small changes of the dispersion. All in all, the dispersion measurement at the corrector magnets is possible by using the spin tune as a tool.

8.1.4. Outlook: Orbit Correction and EDM Measurement

For the planned first measurement of the EDM with the help of an RF Wien filter [30], a feedback loop, which fixes the Wien filter frequency to a harmonic of the spin precession frequency, is planned [99]. If the orbit feedback is running in parallel and changing corrector magnets at positions with high dispersion without adjusting the revolution frequency, the momentum of the beam changes (3.46). This momentum change results in a spin tune change. This spin tune

8.1. Dispersion Measurements at the Corrector Magnets

change leads to a readjustment of the RF Wien filter frequency. In order to avoid this chain of changes, the measured dispersion at the corrector magnets can be fed in the orbit feedback system and a readjustment of the cavity frequency should lead to a stable momentum. Within this setup, the Wien filter feedback loop has only to adjust the Wien filter frequency by smaller amounts, which should result in more stable conditions.

9. Conclusion and Outlook

The measurement of EDMs of fundamental particles is complementary to the high energy experiments to solve the puzzle of antimatter and matter differences in the known universe. Storage rings can be used to measure the EDMs of charged hadrons, for which no direct EDM measurement exist at the moment. Within this thesis, the focus was on the investigation of the existing storage ring COSY at Jülich. The orbit quality, one major source of systematic contributions to the EDM measurement, was studied in detail. Especially the model independent orbit correction is improved. For this correction, a software measuring the orbit response matrix was developed from scratch. This software allows an automated measurement of the orbit response matrix. The measurement of the matrix was successfully tested. In a second step, an algorithm for orbit correction is developed, based on the singular value decomposition. The developed algorithm is successfully applied and the orbit is corrected down to an RMS of 2 mm. The developed algorithm is the starting point for an ongoing project of a live orbit feedback which is able to counteract time dependent instabilities of the magnets at COSY.

In addition to these algorithms, the resolution of the Beam Position Monitors, including the readout electronics was analyzed. The existing BPMs are able to measure the orbit with a resolution of $\approx 1 \mu\text{m}$, but the accuracy is much worse: 0.1 mm. The accuracy is dominated by the readout electronics. After the detailed analysis of the behavior, an upgrade program of the BPM electronics started and is ongoing. With the upgrade, the accuracy should be in the range of $4 \mu\text{m}$.

A third focus, connected to the orbit correction was the question "Why is the orbit not getting better?". This question was answered by simulations, using the program MADX and the developed orbit correction algorithms. The simulations show, that the main source of beam displacements is connected to the alignment precision of the quadrupole and dipole magnets of COSY. To explain the measured orbit RMS, the magnets can only be aligned with a precision of $\approx 0.5 \text{ mm}$. A survey of these magnets shows that they are exactly aligned with the precision, which was predicted by the simulation. In order to improve the orbit quality, a readjustment of the magnets is in progress. In addition to this alignment precision, the possibility of upgrading COSY with additional corrector magnets or BPMs was investigated. By adding BPMs the overall RMS can

9. Conclusion and Outlook

be improved by a factor 2. Additional corrector magnets allow an improvement of a factor 3. The orbit RMS can be reduced by one order of magnitude, if additional corrector magnets and additional BPMs are installed. With a re-alignment of the magnets to 0.1 mm and an installation of additional elements, the orbit RMS should be in the order of 10 μm , which is in the same range as the resolution of the upgraded BPM system.

If all these steps are done, a direct measurement of the deuteron's EDM down to $d_{\text{EDM}} \approx 5 \cdot 10^{-21} e \text{ cm}$ is possible by applying the Wien filter method and trusting the simulations presented in [16].

Besides the topics directly related to the orbit correction, a new method of measuring the dispersion at the positions of the corrector magnets was presented. This method is based on the monitoring of spin tune changes by changing of corrector magnet strengths. The measured dispersion agrees qualitatively with the one measured at the BPMs. A direct comparison was not possible, since a time gap of half a year was between the measurements. Within this time, small changes of the dispersion are expected, since the setting of COSY needs always some fine tuning.

All in all, the developed algorithms and software packages function as expected and a way of upgrading COSY towards an improved EDM sensitivity was presented.

Bibliography

- [1] Alpher, R.A., Bethe, H. and Gamow, G. The Origin of Chemical Elements. *Physical Review*, 73(7):803–804, 1948. <https://doi.org/10.1103/PhysRev.73.803>.
- [2] Wiebusch, C. *Astronomie und Astrophysik (Lecture notes)*. Aachen, 2011.
- [3] Fields, B., Molaro, P. and Sarkar, S. Review of Particle Physics: Big-Bang Nucleosynthesis. *Chinese Physics C*, 40(10):100001, 2016. <https://doi.org/10.1088/1674-1137/40/10/100001>.
- [4] Ade, P.A.R. et al. Planck 2013 results. XVI. Cosmological parameters. *Astronomy & Astrophysics*, 571:A16, 2014. <https://doi.org/10.1051/0004-6361/201321591>.
- [5] Riotto, A. and Trodden, M. RECENT PROGRESS IN BARYOGENESIS. *Annual Review of Nuclear and Particle Science*, 49(1):35–75, 1999. <https://doi.org/10.1146/annurev.nucl.49.1.35>.
- [6] Battiston, R. The antimatter spectrometer (AMS-02): A particle physics detector in space. *Nuclear Instruments and Methods in Physics Research Section A: Accelerators, Spectrometers, Detectors and Associated Equipment*, 588(1-2):227–234, 2008. <https://doi.org/10.1016/j.nima.2008.01.044>.
- [7] Sakharov, A.D. Violation of CP invariance, C asymmetry, and baryon asymmetry of the universe. *Pisma Zh.Eksp.Teor.Fiz.* 5 (1967) 32-35, 5:32–35, 1967. <https://doi.org/10.1070/PU1991v034n05ABEH002497>.
- [8] Lee, T.D. and Yang, C.N. Question of Parity Conservation in Weak Interactions. *Physical Review*, 104(1):254–258, 1956. <https://doi.org/10.1103/PhysRev.104.254>.
- [9] Wu, C.S. et al. Experimental Test of Parity Conservation in Beta Decay. *Physical Review*, 105(4):1413–1415, 1957. <https://doi.org/10.1103/PhysRev.105.1413>.
- [10] Angelopoulos, A. et al. First direct observation of time-reversal non-invariance in the neutral-kaon system. *Physics Letters B*, 444(1-2):43–51, 1998. [https://doi.org/10.1016/S0370-2693\(98\)01356-2](https://doi.org/10.1016/S0370-2693(98)01356-2).

Bibliography

- [11] Griffiths, D. *Introduction to elementary particles*. Wiley-VCH, Weinheim, 2nd. rev. ed. edition, 2009.
- [12] Hori, M. et al. Buffer-gas cooling of antiprotonic helium to 1.5 to 1.7 K, and antiproton-to-electron mass ratio. *Science (New York, N.Y.)*, 354(6312):610–614, 2016. <https://doi.org/10.1126/science.aaf6702>.
- [13] Christenson, J.H. et al. Evidence for the 2π Decay of the K^0_S Meson. *Physical Review Letters*, 13(4):138–140, 1964. <https://doi.org/10.1103/PhysRevLett.13.138>.
- [14] Kobayashi, M. and Maskawa, T. CP -Violation in the Renormalizable Theory of Weak Interaction. *Progress of Theoretical Physics*, 49(2):652–657, 1973. <https://doi.org/10.1143/PTP.49.652>.
- [15] Chriplovič, I.B. and Lamoreaux, S.K. *CP violation without strangeness: Electric dipole moments of particles, atoms, and molecules*. Texts and monographs in physics. Springer, Berlin [u.a.], 1997.
- [16] Rosenthal, M. *Experimental Benchmarking of Spin Tracking Algorithms for Electric Dipole Moment Searches at the Cooler Synchrotron COSY*. PhD thesis, RWTH Aachen University, Aachen, 2016.
- [17] Czarnecki, A. and Krause, B. Neutron Electric Dipole Moment in the Standard Model: Complete Three-Loop Calculation of the Valence Quark Contributions. *Physical Review Letters*, 78(23):4339–4342, 1997. <https://doi.org/10.1103/PhysRevLett.78.4339>.
- [18] Pospelov, M. and Ritz, A. Electric dipole moments as probes of new physics. *Annals of Physics*, 318(1):119–169, 2005. <https://doi.org/10.1016/j.aop.2005.04.002>.
- [19] Guo, F.K. and Meißner, U.G. Baryon electric dipole moments from strong CP violation. *Journal of High Energy Physics*, 2012(12), 2012. [https://doi.org/10.1007/JHEP12\(2012\)097](https://doi.org/10.1007/JHEP12(2012)097).
- [20] Pendlebury, J.M. et al. Revised experimental upper limit on the electric dipole moment of the neutron. *Physical Review D*, 92(9), 2015. <https://doi.org/10.1103/PhysRevD.92.092003>.
- [21] Smith, J.H., Purcell, E.M. and Ramsey, N.F. Experimental Limit to the Electric Dipole Moment of the Neutron. *Physical Review*, 108(1):120–122, 1957. <https://doi.org/10.1103/PhysRev.108.120>.
- [22] Baron, J. et al. Order of magnitude smaller limit on the electric dipole moment of the electron. *Science (New York, N.Y.)*, 343(6168):269–272, 2014. <https://doi.org/10.1126/science.1248213>.

- [23] Griffith, W.C. et al. Improved limit on the permanent electric dipole moment of ^{199}Hg . *Physical review letters*, 102(10):101601, 2009. <https://doi.org/10.1103/PhysRevLett.102.101601>.
- [24] Bennett, G.W. et al. Improved limit on the muon electric dipole moment. *Physical Review D*, 80(5), 2009. <https://doi.org/10.1103/PhysRevD.80.052008>.
- [25] Dekens, W. et al. Unraveling models of CP violation through electric dipole moments of light nuclei. *Journal of High Energy Physics*, 2014(7), 2014. [https://doi.org/10.1007/JHEP07\(2014\)069](https://doi.org/10.1007/JHEP07(2014)069).
- [26] Dmitriev, V.F. and Sen'kov, R.A. Schiff moment of the mercury nucleus and the proton dipole moment. *Physical review letters*, 91(21):212303, 2003. <https://doi.org/10.1103/PhysRevLett.91.212303>.
- [27] Guidoboni, G. et al. How to Reach a Thousand-Second in-Plane Polarization Lifetime with 0.97-GeV/c Deuterons in a Storage Ring. *Physical review letters*, 117(5):054801, 2016. <https://doi.org/10.1103/PhysRevLett.117.054801>.
- [28] Rathmann, F., Saleev, A. and Nikolaev, N.N. Search for electric dipole moments of light ions in storage rings. *Physics of Particles and Nuclei*, 45(1):229–233, 2014. <https://doi.org/10.1134/S1063779614010869>.
- [29] Morse, W.M., Orlov, Y.F. and Semertzidis, Y.K. rf Wien filter in an electric dipole moment storage ring: The “partially frozen spin” effect. *Physical Review Special Topics - Accelerators and Beams*, 16(11), 2013. <https://doi.org/10.1103/PhysRevSTAB.16.114001>.
- [30] Slim, J. et al. Electromagnetic Simulation and Design of a Novel Waveguide RF Wien Filter for Electric Dipole Moment Measurements of Protons and Deuterons. *Nuclear Instruments and Methods in Physics Research Section A: Accelerators, Spectrometers, Detectors and Associated Equipment*, 828:116–124, 2016. <https://doi.org/10.1016/j.nima.2016.05.012>.
- [31] Gebel, R., Nass, A. and Rathmann, F. Waveguide RF Wien Filter: Commissioning and initial investigations.
- [32] Rosenthal, M. RF Wien Filter Based EDM Measurements using Clockwise/Counterclockwise Beams: JEDI: Internal Note. 2016.
- [33] Wiedemann, H. *Particle Accelerator Physics*. Springer Berlin Heidelberg and Springer e-books and Springer, Berlin, Heidelberg, 3rd ed edition, 2007. <http://www.worldcat.org/oclc/191467326>.

Bibliography

- [34] Wille, K. *Physik der Teilchenbeschleuniger und Synchrotronstrahlungsquellen: Eine Einführung*. Teubner-Studienbücher. Physik. Teubner, Stuttgart, 2., überarb. und erw. Aufl. edition, 1996.
- [35] Rossbach, J. and Schmüser, P. Basic course on accelerator optics. In *CAS - CERN Accelerator School*, pages 17–88. CERN, 1994. <https://doi.org/10.5170/CERN-1994-001.17>.
- [36] Steier, C., Safranek, J. and Xiaobiao, H. Beam-based Diagnostics, 06/2015. http://www2.als.lbl.gov/als_physics/csteier/uspas15/.
- [37] Hill, G.W. On the part of the motion of the lunar perigee which is a function of the mean motions of the sun and moon. *Acta Mathematica*, 8(1):1–36, 1886. <https://doi.org/10.1007/BF02417081>.
- [38] Le Duff, J. Longitudinal Beam Dynamics in circular Accelerators. In *CAS - CERN Accelerator School*, pages 289–312. CERN, 1994. <https://doi.org/10.5170/CERN-1994-001.17>.
- [39] Pirkl, W. Longitudinal beam dynamics. In Turner, S., editor, *CAS, CERN Accelerator School, fifth advanced accelerator physics course*, volume 95-06 of *CERN*, pages 233–258, Geneva, 1995. CERN, European Organization for Nuclear Research.
- [40] Hofmann, A. Transporting the Energy Calibration across Optics. In Poole, J., editor, *Proceedings of the Third Workshop on LEP Performance*, pages 303–308, Geneva, 1993. CERN.
- [41] Wenninger, J. Orbit Corrector Magnets and Beam Energy. *CERN - SL DIVISION*, (97-06 OP), 1997. <https://jwenning.web.cern.ch/jwenning/documents/EnergyCal/hcorr.pdf>.
- [42] Li, Y. and Krinsky, S. Beam Energy Variation with Dipole fault. In *Proceedings IPAC2012*, pages 1305–1307. IEEE, [S. l.], 2012.
- [43] Ohlsen, G.G. Polarization transfer and spin correlation experiments in nuclear physics. *Reports on Progress in Physics*, 35(2):717–801, 1972. <https://doi.org/10.1088/0034-4885/35/2/305>.
- [44] Fick, D. *Einführung in die Kernphysik mit polarisierten Teilchen*. Bibliographisches Inst., 1951.
- [45] Hoffstaetter, G.H., editor. *High-energy polarized proton beams: A modern view*, volume 218 of *Springer Tracts in Modern Physics*. Springer, New York, 2006. <https://doi.org/10.1007/978-0-387-34754-7>.

- [46] Buon, J. and Koutchouk, J. Polarization of electron and proton beams. In Turner, S., editor, *CAS, CERN Accelerator School, fifth advanced accelerator physics course*, volume 95-06 of *CERN*, pages 879–940, Geneva, 1995. CERN, European Organization for Nuclear Research.
- [47] Pauli, W. Zur Quantenmechanik des magnetischen Elektrons. *Z. Physik (Zeitschrift für Physik)*, 43(9-10):601–623, 1927. <https://doi.org/10.1007/BF01397326>.
- [48] Silenko, A.Y. Quantum-Mechanical Description of the Electromagnetic Interaction of Relativistic Particles with Electric and Magnetic Dipole Moments. *Russian Physics Journal*, 48(8):788–792, 2005. <https://doi.org/10.1007/s11182-005-0203-1>.
- [49] Povh, B. et al. *Particles and Nuclei: An Introduction to the Physical Concepts*. Springer Berlin Heidelberg, Berlin, Heidelberg, 2002.
- [50] <http://physics.nist.gov/cuu/index.html>. <http://physics.nist.gov/cuu/index.html>.
- [51] Thomas, L.H. I. The kinematics of an electron with an axis. *The London, Edinburgh, and Dublin Philosophical Magazine and Journal of Science*, 3(13):1–22, 1927. <https://doi.org/10.1080/14786440108564170>.
- [52] Bargmann, V. and Telegdi, V.L. Precession of the Polarization of Particles Moving in a Homogeneous Electromagnetic Field. *Physical Review Letters*, 2(10):435–436, 1959. <https://doi.org/10.1103/PhysRevLett.2.435>.
- [53] Weidmann, R. et al. The polarized ion source for COSY. *Review of Scientific Instruments*, 67(3):1357–1358, 1996. <https://doi.org/10.1063/1.1146665>.
- [54] Bräutigam, W. et al. Status and perspectives of the cyclotron JULIC as COSY injector. *Nukleonika*, Vol. 48,suppl.2:123–126, 2003. http://yadda.icm.edu.pl/baztech/element/bwmeta1.element.baztech-article-BUJ5-0004-0080/c/Status_and_perspectives_of_the_cyclotron_JULIC.pdf.
- [55] Weidemann, C. et al. Toward polarized antiprotons: Machine development for spin-filtering experiments. *Physical Review Special Topics - Accelerators and Beams*, 18(2), 2015. <https://doi.org/10.1103/PhysRevSTAB.18.020101>.
- [56] Maier, R. Cooler synchrotron COSY — Performance and perspectives. *Nuclear Instruments and Methods in Physics Research Section A: Accelerators, Spectrometers, Detectors and Associated Equipment*, 390(1-2):1–8, 1997. [https://doi.org/10.1016/S0168-9002\(97\)00324-0](https://doi.org/10.1016/S0168-9002(97)00324-0).

Bibliography

- [57] Stein, H.J. et al. Present Performance of Electron Cooling at Cosy-Jülich. In *18th Conference on Charged Particle Accelerators (RUPAC 2002) Obninsk, Russia, October 1-4, 2002*, 2011. <https://inspirehep.net/record/885968/files/arXiv:1101.5963.pdf>.
- [58] Kamerdzhev, V., Bechstedt, U. and Esser, F.M. 2MeV Electron Cooler for COSY and HESR – First Results. In *Proceedings of the 5th International Particle Accelerator Conference [also] IPAC14, June 15-20, Dresden, Germany*, pages 765–767, Geneva, 2014. JACoW.
- [59] Prasuhn, D. et al. Electron and stochastic cooling at COSY. *Nuclear Instruments and Methods in Physics Research Section A: Accelerators, Spectrometers, Detectors and Associated Equipment*, 441(1-2):167–174, 2000. [https://doi.org/10.1016/S0168-9002\(99\)01128-6](https://doi.org/10.1016/S0168-9002(99)01128-6).
- [60] Dietrich, J., Kamerdzhev, V. and Rukhlyada, N.Y. *Instruments and Experimental Techniques*, 46(5):581–586, 2003. <https://doi.org/10.1023/A:1026053231074>.
- [61] Maier, R. et al. Non-Beam Disturbing Diagnostics at COSY-Jülich. In *EPAC1990*, pages 800–802, 1990.
- [62] Leonova, M.A. *Achieving High Spin-Flip Efficiency with an RF Magnet and Discovery of Spin-Resonance Strength Formulae Problem*. PhD thesis, Michigan U, 01.01.2008. http://inspirehep.net/record/1391452/files/leonova_1.pdf.
- [63] Mey, S. and Gebel, R. Towards an RF Wien-Filter for EDM Experiments at COSY. In *Proceedings of the 6th International Particle Accelerator Conference [also] IPAC 2015, Richmond, USA, May 3-8, 2015*, pages 3761–3763, Geneva, 2014. JACoW.
- [64] Benati, P. et al. Synchrotron oscillation effects on an rf-solenoid spin resonance. *Physical Review Special Topics - Accelerators and Beams*, 15(12), 2012. <https://doi.org/10.1103/PhysRevSTAB.15.124202>.
- [65] Benati, P. et al. Erratum: Synchrotron oscillation effects on an rf-solenoid spin resonance [Phys. Rev. ST Accel. Beams 15 , 124202 (2012)]. *Physical Review Special Topics - Accelerators and Beams*, 16(4), 2013. <https://doi.org/10.1103/PhysRevSTAB.16.049901>.
- [66] PAX collaboration. Letter of Intent for Antiproton-Proton Scattering Experiments with Polarization. 2003.
- [67] Bisplinghoff, J. et al. Position sensitivity by light splitting in scintillator arrays. *Nuclear Instruments and Methods in Physics Research Section A: Accelerators, Spectrometers, Detectors and Associated Equipment*, 329(1-2):151–162, 1993. [https://doi.org/10.1016/0168-9002\(93\)90930-G](https://doi.org/10.1016/0168-9002(93)90930-G).

- [68] Collaboration, W.a.C. et al. Proposal for the Wide Angle Shower Apparatus (WASA) at COSY-Juelich - WASA at COSY.
- [69] Barsov, S. et al. ANKE, a new facility for medium energy hadron physics at COSY-Jülich. *Nuclear Instruments and Methods in Physics Research Section A: Accelerators, Spectrometers, Detectors and Associated Equipment*, 462(3):364–381, 2001. [https://doi.org/10.1016/S0168-9002\(00\)01147-5](https://doi.org/10.1016/S0168-9002(00)01147-5).
- [70] Bagdasarian, Z. et al. Measuring the polarization of a rapidly precessing deuteron beam. *Physical Review Special Topics - Accelerators and Beams*, 17(5), 2014. <https://doi.org/10.1103/PhysRevSTAB.17.052803>.
- [71] Eversmann, D. et al. New Method for a Continuous Determination of the Spin Tune in Storage Rings and Implications for Precision Experiments. *Physical review letters*, 115(9):094801, 2015. <https://doi.org/10.1103/PhysRevLett.115.094801>.
- [72] Eversmann, D. *High Precision Spin Tune Determination at the Cooler Synchrotron in Jülich: in preparation*. PhD thesis, RWTH Aachen University, Aachen, 2017.
- [73] Laux, F. *Development of capacitive beam position, beam current and Schottky-signal monitors for the Cryogenic Storage Ring (CSR)*. PhD, Max-Planck Institut für Kernphysik, Heidelberg, July 2011. <http://nbn-resolving.de/urn:nbn:de:bsz:16-heidok-124351>.
- [74] Shafer, R.E. Beam position monitoring. In *The Physics of Particle Accelerators Vol. I (based on the US Particle Accelerator School (USPAS) Seminars and Courses)*, AIP Conference Proceedings, pages 601–636. AIP, 1992. <http://dx.doi.org/10.1063/1.41980>, <https://doi.org/10.1063/1.41980>.
- [75] Forck, P., Kowina, P. and Liakin, D. Beam Position Monitors. In Brandt, D., editor, *CERN Accelerator School, beam diagnostics, Dourdan, France, 28 May - 6 June 2008*, pages 187–228, 2009.
- [76] Müller, R. *Rauschen*, volume Bd. 15 of *Halbleiter-Elektronik*. Springer-Verlag, Berlin and New York, 2. überarb., u. erw. aufl edition, 1990.
- [77] Hinder, F. et al. Development of New Beam Position Monitors at COSY. In *IBIC 2015*, pages 339–343, Genf, 2015. CERN. <http://accelconf.web.cern.ch/AccelConf/IBIC2015/papers/tupb015.pdf>, <https://doi.org/10.18429/JACoW-IBIC2015-TUPB015>.
- [78] Trinkel, F. *PhD Thesis: in preparation*. PhD thesis, RWTH Aachen University, Aachen, 2017.

Bibliography

- [79] KFKI-MSzKI. BPMeP Vorverstärker: (manual): private communication with M. Simon.
- [80] KFKI-MSzKI. BPMeA Analoge Elektronik: (manual): private communication with M. Simon.
- [81] KFKI-MSzKI. BPMeD Digitale Elektronik: (manual): private communication with M. Simon.
- [82] Libera. Libera Hadron: High performance beam position monitor electronics for hadron circular machines: (user manual), 2016. http://www.i-tech.si/accelerators-instrumentation/libera-hadron/benefits_7.
- [83] Žnidarčič, M. Hadron Beam Position Processor: Specifications (user manual). *Libera*, 2016.
- [84] Safranek, J. Experimental determination of storage ring optics using orbit response measurements. *Nuclear Instruments and Methods in Physics Research Section A: Accelerators, Spectrometers, Detectors and Associated Equipment*, 388(1-2):27–36, 1997. [https://doi.org/10.1016/S0168-9002\(97\)00309-4](https://doi.org/10.1016/S0168-9002(97)00309-4).
- [85] Weidemann, C. et al. Model Driven Machine Improvement of COSY Based on ORM Data. In *IPAC 2016*, pages 3240–3243, Genf, June 2016. [CERN]. <http://jacow.org/ipac2016/papers/thpmb009.pdf>, <https://doi.org/10.18429/JACoW-IPAC2016-THPMB009>.
- [86] Brun, R. and Rademakers, F. ROOT — An object oriented data analysis framework. *Nuclear Instruments and Methods in Physics Research Section A: Accelerators, Spectrometers, Detectors and Associated Equipment*, 389(1-2):81–86, 1997. [https://doi.org/10.1016/S0168-9002\(97\)00048-X](https://doi.org/10.1016/S0168-9002(97)00048-X).
- [87] Retzlaff, M. private communication: Corrector Magnet Stability, 29.06.2016.
- [88] Vashegyi, T. private communication: Cosy Timing System, 28.06.2016.
- [89] Barlow, R. *Statistics: A guide to the use of statistical methods in the physical sciences*. The Manchester physics series. Wiley, Chichester, England and New York, 1989.
- [90] Higham. Cholesky factorization. 2016. http://www.encyclopediaofmath.org/index.php?title=Cholesky_factorization&oldid=37467.

- [91] Hansen, P.C. *Discrete inverse problems: Insight and algorithms*. Fundamentals of algorithms. Society for Industrial and Applied Mathematics, Philadelphia, 2010.
- [92] Golub, G.H. and Van Loan, Charles F. *Matrix computations*. Johns Hopkins studies in the mathematical sciences. Johns Hopkins University Press, Baltimore, 3rd ed edition, 1996.
- [93] Lefebvre, M. et al. Propagation of errors for matrix inversion. *Nuclear Instruments and Methods in Physics Research Section A: Accelerators, Spectrometers, Detectors and Associated Equipment*, 451(2):520–528, 2000. [https://doi.org/10.1016/S0168-9002\(00\)00323-5](https://doi.org/10.1016/S0168-9002(00)00323-5).
- [94] Kharytonov, A., Böhm, E. and Wimmer-Schweingruber, R.F. Regularization methods used in error analysis of solar particle spectra measured on SOHO/EPHIN. *Astronomy and Astrophysics*, 495(2):663–675, 2009. <https://doi.org/10.1051/0004-6361:200810854>.
- [95] Grote, H. and Schmidt, F. MAD-X. 2016. <http://madx.web.cern.ch/madx/>.
- [96] Poth, H. Electron cooling: Theory, experiment, application. *Physics Reports*, 196(3-4):135–297, 1990. [https://doi.org/10.1016/0370-1573\(90\)90040-9](https://doi.org/10.1016/0370-1573(90)90040-9).
- [97] The EDDA Collaboration Eur. Phys. J. A. A precision measurement of pp elastic scattering cross-sections at intermediate energies. *The European Physical Journal A*, 22(1):125–148, 2004. <https://doi.org/10.1140/epja/i2004-10011-3>.
- [98] Froissart, M. and Stora, R. Depolarisation d'un faisceau de protons polarisés dans un synchrotron. *Nuclear Instruments and Methods*, 7(3):297–305, 1960. [https://doi.org/10.1016/0029-554X\(60\)90033-1](https://doi.org/10.1016/0029-554X(60)90033-1).
- [99] Gebel, R., Nass, A. and Rathmann, F. Waveguide RF Wien Filter: Commissioning and initial investigations. http://collaborations.fz-juelich.de/ikp/jedi/public_files/proposals/JEDI-RF-Wien-filter_11.11.2016_combined.pdf.
- [100] Evans, M., Hastings, N.A.J. and Peacock, J.B. *Statistical distributions*. Wiley series in probability and statistics Texts and references section. Wiley, New York, NY [u.a.], 3. ed. edition, 2000.
- [101] Johnson, N.L., Kotz, S. and Balakrishnan, N. *Continuous univariate distributions I-II*. Wiley series in probability and mathematical statistics. John Wiley & Sons, New York, 2. edition edition, 1994-1995.

Bibliography

- [102] Weisstein, E.W. From MathWorld - A Wolfram Web Resource: Chi Distribution, 2016. <http://mathworld.wolfram.com/ChiDistribution.html>.

List of Figures

2.1. EDM under parity transformation and time reversal.	8
3.1. Coordinate System.	16
3.2. Focusing of a quadrupole magnet.	18
3.3. Phase space ellipse.	21
5.1. COSY layout.	34
5.2. EDDA scattering angles.	36
5.3. EDDA detector.	36
6.1. BPM sketch.	39
6.2. Comparison of accuracy and precision.	41
6.3. Distributions of the digitized difference and sum signals.	44
6.4. Resolution of the BPM system depending on the beam position.	45
6.5. Beam position accuracy sourced by the uncertainty of the gains in the electronics.	47
6.6. Measured beam position depending on the true beam position.	48
7.1. Layout of the ORM measurement software.	52
7.2. Corrector magnet steps and BPM trigger events.	53
7.3. Closed orbit response for SH01 & bpmx18 & bpmx19.	55
7.4. Distribution of the BPM readout delay.	56
7.5. Noise measurement for bpmx25	58
7.6. STD distribution for horizontal and vertical BPMs.	59
7.7. Amplitudes of the global noise fit	60
7.8. Noise measurement for bpmx27	61
7.9. Fit of the ORM entry $M_{\text{bpmx18,SH01}}$	63
7.10. Fit of ORM entry $M_{\text{bpmx10,SH01}}$, including the BPM readout elec- tronics model.	64
7.11. Complete measured ORM.	65
7.12. Distribution of the regularization parameter k	73
7.13. Horizontal uncorrected and corrected orbit.	74
7.14. Vertical uncorrected and corrected orbit.	75
7.15. Orbit RMS as function of the regularization parameter k	76
7.16. Optical functions used in the simulation.	77
7.17. Orbit RMS at BPMs depending on magnet misalignment.	79

List of Figures

7.18. Orbit RMS at quadrupoles against the RMS at BPMs for ideal BPMs.	80
7.19. Orbit RMS at quadrupoles depending on magnet misalignment for realistic BPMs.	81
7.20. Orbit RMS at BPMs depending on magnet misalignment.	84
7.21. Orbit RMS at quadrupoles depending on magnet misalignment for ideal BPMs.	85
7.22. Survey distribution of the dipoles.	86
7.23. Survey distribution of the quadrupole magnets.	87
7.24. Conversion factors with upgraded corrector/BPM system.	90
8.1. Spin tune change due to frequency change.	95
8.2. Spin tune spectra during the change of corrector magnet 35.	97
8.3. Spin tune jumps due to corrector magnet SH35.	98
8.4. Dispersion measurement with BPM bpmx24.	99
8.5. Dispersion measurement with BPMs and corrector magnets.	100

List of Tables

2.1. Dependency: Vertical orbit RMS, polarization buildup and equivalent EDM.	13
4.1. Measurement results for the gyromagnetic anomaly for different particles.	31
7.1. Corrector magnet settings.	54
7.2. Conversion factors between alignment resolution and orbit RMS at BPMs.	79
7.3. Conversion factors between alignment resolution and orbit RMS at quadrupole magnets.	82
7.4. Conversion factors between alignment resolution and orbit RMS for additional elements.	89

A. Appendix

A.1. Derivation of the RMS Expectation Value

In the following the RMS expectation value is derived by using, the literature [100, p. 57], [101], and [102]. The distribution

$$z = \sqrt{\sum_{i=1}^N \left(\frac{x_i}{\sigma_i}\right)^2} = \frac{1}{\sigma} \sqrt{\sum_{i=1}^N x_i^2} \quad (\text{A.1})$$

follows a noncentral χ -distribution. In the second step a common resolution σ is considered. This distribution has two parameters: λ and N . The parameter N is the number of degrees of freedom and λ is:

$$\lambda = \sqrt{\sum_{i=1}^N \left(\frac{\mu_i}{\sigma_i}\right)^2} = \frac{1}{\sigma} \sqrt{\sum_{i=1}^N \mu_i^2}. \quad (\text{A.2})$$

The first moment of this distribution is given by:

$$\langle z \rangle = \sqrt{\frac{\pi}{2}} L_{1/2}^{(N/2-1)} \left(\frac{-\lambda^2}{2} \right) \quad (\text{A.3})$$

where $L_n^{(a)}(x)$ is the generalized Laguerre polynomial. For the RMS, which is

$$RMS = \frac{z}{\sqrt{N}} \cdot \sigma, \quad (\text{A.4})$$

and the standard deviation σ of the sample being equal for all random variables x_i , the first moment of the RMS reads:

$$\langle RMS \rangle = \sqrt{\frac{\pi}{2}} L_{1/2}^{(N/2-1)} \left(\frac{-\lambda^2}{2} \right) \frac{\sigma}{\sqrt{N}} \quad (\text{A.5})$$

For large values of N and $\mu_i \ll \sigma$, the mean $\langle RMS \rangle$ converges to σ .

Acknowledgments

My supervisor Prof. Dr. Jörg Pretz supported me during my Ph.D. study. He was always available for interesting discussions the topic "measuring electric dipole moments with storage rings".

The whole JEDI collaboration helped me in various topics during my studies at Forschungszentrum Jülich. Dr. Frank Rathmann provided always new ideas, which serve as input for technical developments. Dr. Alexander Nass helped to organize the technical equipment to run the experiments at COSY. The data acquisition system is developed and maintained by the colleagues Dr. Volker Hejny and Dr. Peter Wüstner. Dr. Andro Kacharava, the head of the publication comity, organizes the intercultural workshops with the Georgian universities. In looking back, I will remember the events and the hospitality in Tiflis. Prof. Dr. Mei Bai, director of the IKP-4, gives me the opportunity to visit the United States particle accelerator school, where I learned a lot about beam instrumentation. The COSY accelerator group around Dr. Ralf Gebel and Dr. Bernd Lorentz supported me to develop the algorithms and to test them directly at the accelerator. The beam instrumentation group around Dr. Vsevolod Kamerdzhev provided me with technical knowledge about BPMs. The information about the IT-infrastructure to setup the developed algorithms was provided by the control group around Michael Simon. Dr. Marcel Rosenthal, former PhD student, helped me a lot with his knowledge about Beam and Spin dynamics. His office was always a good contact point for questions concerning these topics. PhD student Fabian Trinkel shared the office with me and was always interested in discussions about physical questions. In addition, he motivated me during the PhD time in Jülich. Critical questions, which helped to understand the physical problems in deeper insight, were asked by PhD student Dennis Eversmann. Besides these PhD students, I had the pleasure to work with a motivated group of JEDI PhD students: Sebastian May, Jan Hetzel, Nils Hempelmann, Vera Schmidt, Fabian Müller, Paul Maanen, Stansilav Chekmenev and Artem Saalev. They are doing a lot of daily work to enable beam times and running the experiments.

My patchwork family, Christiane Nordhausen-Hinder & Bernd Nordhausen and Heiner Hinder & Karola Jochmann supported me during my study of physics in the past years.

I express my extraordinary thanks to all these people.